

**CHARACTERIZATION OF NANOSTRUCTURED
SEMICONDUCTORS BY ULTRAFAST LUMINESCENCE IMAGING**

by

Jolie Blake

A dissertation submitted to the Faculty of the University of Delaware in partial fulfillment of the requirements for the degree of Doctor of Philosophy in Chemistry and Biochemistry

Summer 2017

© 2017 Jolie Blake
All Rights Reserved

**CHARACTERIZATION OF NANOSTRUCTURED
SEMICONDUCTORS BY ULTRAFAST LUMINESCENCE IMAGING**

by

Jolie Blake

Approved: _____

Murray Johnston, Ph.D.
Chair of the Department of Chemistry & Biochemistry

Approved: _____

George H. Watson, Ph.D.
Dean of the College of Arts & Sciences

Approved: _____

Ann L. Ardis, Ph.D.
Senior Vice Provost for Graduate and Professional Education

I certify that I have read this dissertation and that in my opinion it meets the academic and professional standard required by the University as a dissertation for the degree of Doctor of Philosophy.

Signed: _____
Lars Gundlach, Ph.D.
Professor in charge of dissertation

I certify that I have read this dissertation and that in my opinion it meets the academic and professional standard required by the University as a dissertation for the degree of Doctor of Philosophy.

Signed: _____
Andrew V. Teplyakov, Ph.D.
Member of dissertation committee

I certify that I have read this dissertation and that in my opinion it meets the academic and professional standard required by the University as a dissertation for the degree of Doctor of Philosophy.

Signed: _____
Mathew DeCamp, Ph.D.
Member of dissertation committee

I certify that I have read this dissertation and that in my opinion it meets the academic and professional standard required by the University as a dissertation for the degree of Doctor of Philosophy.

Signed: _____
Joshua Zide, Ph.D.
Member of dissertation committee

ACKNOWLEDGEMENTS

These past 6 years have been truly transformative. I have deepened my knowledge of chemistry, fallen in and out of love with my work and gained a mind flexible enough to tackle any problem. More importantly, this period has taught me about myself, my weaknesses and strengths and provided a thorough and invaluable education on human nature. I am grateful for being given the opportunity to experience all of these things, the good and especially the bad. I must acknowledge all the people that helped shaped this experience.

I would like to thank the members of the Gundlach Group, past and present, because without them this work would not be possible. In particular, I would like to thank Dr. Lars Gundlach for his hands-on help in the lab, help with preparing this dissertation and for having an open door policy. I would also like to thank Dr. Jesus Nieto-Pescador for this constant willingness to help me align my NOPA and for his patience in teaching me optical alignment. I thank Dr. Peter Eldridge for his work with Igor, which made it possible to efficiently collect and analyze data and hence significantly speed up the period towards publication. I am thankful to Baxter Abraham for his help with the optics, his great sense of humor and his resourcefulness in procuring things we needed in the lab. Additionally, I thank Dr. Zide who took the time to provide insight on semiconductor material properties, which turned out to be truly invaluable to completing this dissertation.

I want to acknowledge Dr. Sharon Neal whose grace and wisdom I hope to someday acquire. I am truly grateful for the talks that we had and how, like a sage, you always knew what to say and had the right answers to every situation. Your advice and mentorship were instrumental to me completing my Ph.D.

I am thankful for the other members of the Chemistry & Biochemistry Department such as Doug Nixon and Susan Cheadle. I want to thank Doug for helping me learn how to handle different types of glass, for quickly repairing my numerous cracked quartz tubes and for his useful input in helping me manifest many of my ideas. Susan Cheadle was always ready to help with the necessary paper work at each stage of my academic career. I especially want to thank her for helping me sort out my immigration documents to ensure my continued enrollment in the program.

I am also thankful for the University of Delaware NOBCCChE student chapter and its members. The chapter's events would not have been possible if it was not for the support of Dr. Murray Johnston who pledged his support for the group from the beginning. I want to thank the NOBCCChE student members for supporting me and the other founding members in the creation of this chapter and for helping me with my vision of establishing our professional network.

To Ornella Sathoud, supportive NOBCCChE board member and friend, thank you for being a fellow black female scientist in this marginalizing environment and for being a formidable and resilient force of nature. I am grateful for our long talks on racism, prejudice and perseverance in this program despite the odds. I truly admire your determination. I have discovered the beauty in being constantly undermined, disparaged, treated less than and having your ability questioned is that it acts as a refining process. It polishes you into a person who does not rely on external validation or acknowledgment in pursuit of your highest potential. It helps you to recognize that your place here was not acquired by charity or luck but hard earned. If you have not already realized this effect I strongly believe you will soon.

I cannot forget my undergraduate advisor Dr. Katherine Plass. If it was not for you sharing your undying passion and enthusiasm for research with me I probably would not be here today. If it was not for your insightful advice early on in this program, I definitely would not have been here today completing my Ph.D. Thank you for being a great teacher, advisor and mentor. Thank you for giving me the opportunity to work in your lab, encouraging me to pursue graduate school and for believing that

I had what it took to be a good researcher and chemist.

Lastly, I want to thank my mom, my significant other Jonathan and the rest of my family. Jonathan, thank you for being so selfless, understanding and patient and for all those long nights you sat in my office waiting for me while I worked in the lab. It would not have been possible without you. Mom, I dedicate this dissertation to you. You were my first teacher, my biggest supporter, my one-woman fan club and the one person who never once doubted my ability to do anything especially completing this program. Thank you for your sacrifice, constant encouragement and prayers.

You may write me down in history

With your bitter, twisted lies,

You may trod me in the very dirt

But still, like dust, I'll rise.

You may shoot me with your words,

You may cut me with your eyes,

You may kill me with your hatefulness,

But still, like air, I'll rise.

Maya Angelou (1921-2014)

TABLE OF CONTENTS

LIST OF TABLES	x
LIST OF FIGURES	xi
ABSTRACT	xviii
 Chapter	
1 INTRODUCTION	1
1.0.1 Measuring the electronic properties of nanostructures	6
1.1 Amplified Spontaneous Emission	7
1.2 Objectives	11
2 EXPERIMENTAL METHODS	13
2.1 Ultrafast Kerr-gated Microscope	13
2.1.1 Kerr-electro-optic effect	13
2.1.2 Laser system	17
2.1.3 Microscope optical setup	19
2.1.4 Ultraviolet Configuration	20
2.1.5 Modes of operation	20
2.2 Sample Preparation	21
3 KERR-GATED MICROSCOPY IN THE VISIBLE DETECTION	

RANGE	24
3.1 Cadmium Sulfide Selenide Semiconductor material	24
3.1.1 CdS _x Se _{1-x} Nanostructure Synthesis	25
3.2 Ultrafast Measurements	26
3.2.1 Spatial Variation in Carrier Dynamics	26
3.3 Extracting non-radiative recombination rates in a single CdS _x Se _{1-x} nanowire	35
3.3.1 Introduction	35
3.3.2 Materials and Methods	36
3.3.3 Results and discussion	38
3.3.4 Conclusions	41
4 ZINC OXIDE SEMICONDUCTOR MATERIAL	42
4.1 Historical Timeline	42
4.2 Fundamental properties and applications	43
4.2.1 Crystal structure	45
4.3 Synthesis and growth	46
4.3.1 Vapor Phase Synthesis of ZnO	48
4.3.2 Solution based Synthesis of ZnO	55
4.4 Point defects	69
5 ULTRAVIOLET FEMTOSECOND KERR-GATED MICROSCOPY	75
5.1 Kerr Medium Selection for the UV	75
5.2 Preliminary Ultrafast Measurements	78
5.2.1 ZnO single nanowire samples	78
5.2.2 Steady State Measurements	78
5.2.3 Time-resolved Spectroscopy	82

5.2.4	Time-resolved Imaging	85
5.3	Conclusion	87
6	KERR-GATED MICROSCOPY FOR MEASURING DEFECT DENSITY	89
6.1	Introduction	89
6.2	Results and Discussion	92
6.2.1	Steady state measurements	92
6.2.2	Time resolved measurements	95
6.2.3	Recombination rates from the Amplified Spontaneous Emission Model	97
6.2.4	The influence of a defect density profile	101
6.3	Experimental methods	106
6.3.1	Single ZnO nanowire samples	106
6.3.2	Computational Techniques	107
6.3.3	SEM-CL measurements	107
6.4	Additional characterization	108
6.4.1	Finite Difference Time Domain Calculations	108
6.4.2	SEM-cathodoluminescence measurements	109
6.4.3	Middle region	111
6.5	Conclusion	112
7	SUMMARY	113
	BIBLIOGRAPHY	115
	Appendix	
A	FIGURE REPRINT PERMISSIONS	137

LIST OF TABLES

3.1	ASE Model Fitting Parameters	39
4.1	Properties of wurtzite ZnO. Reprinted with permission from Elsevier. [130]	44
6.1	ASE Model Fitting Parameters for Global Fit of Luminescence Dynamics from Region 1 and 2	101

LIST OF FIGURES

1.1	Renewable energy supply trends for the US. (From the U.S. Department of Energy, U.S Energy Information Administration Short-Term Energy Outlook report.)	2
1.2	Schematic overview of a dye-sensitized solar cell. Reprinted with permission from. [7]	3
1.3	Schematic of the electron transition in the ASE process.	8
2.1	(a) Schematic of the Kerr-gated microscope setup. S: sample, SO_{1-3} : Schwarzschild objectives, P_{1-2} : polarizers, K: Kerr medium, D: delay line and F, BG: spectral filters, WP: waveplate and PR: prism. Reprinted with permission from American Chemical Society [59].(b) Photograph of the optical column of the microscope.	14
2.2	Schematic of the Kerr -gate showing the polarizers in the crossed (closed-gate) position.	15
2.3	Diagram of a Schwarzschild objective.[69]	18
2.4	(a) Drop cast method where nanowires removed by either wafer sonication, scratching or plucking are suspended in acetone and deposited onto a clean silicon wafer. (b) The electrospray setup. Nanowires suspended in acetone are dispersed onto the substrate by applying a high voltage between a needle and clean substrate. . . .	22
2.5	(a) TEM grid sample holder that allowed for ultrafast measurements and could be transfered directly to SEM measurements without removal of individual grids. Inset shows micrograph of labeled grid. (b) Sample on silicon wafer substrate where a second wafer was used to divide the sample into quadrants for relocating nanowires after ultrafast measurements.	23
3.1	Experimental setup for VLS synthesis of CdS_xSe_{1-x} nanostructures.	26

3.2	(a) SEM image showing a single $\text{CdS}_x\text{Se}_{1-x}$ nanowire resting on a TEM grid. (b) Fluorescence micrograph highlighting three regions of enhanced emission. (c) High resolution SEM image of the nanowire surface. Reprinted with permission from Elsevier.[89]	27
3.3	Integrated luminescence dynamics at three different locations on the single nanowire for excitation fluences 2, 2.6 and 3 mJ/cm^2 . Red line shows fit with ASE model. Reprinted with permission from Elsevier.[89]	28
3.4	(a) CIE standard color matching functions. (b) The CIE 1931 color space chromaticity diagram.	31
3.5	(a) Color matching functions for red, green and blue filters of the optical microscope. (b) Color image a $\text{CdS}_x\text{Se}_{1-x}$ nanowire and the pure color filter images that are combined to produce it.	33
3.6	Spatially resolved color space analysis of the single $\text{CdS}_x\text{Se}_{1-x}$ nanobelt. Reprinted with permission from Elsevier.[89]	34
3.7	The normalized PL spectra for CdS, CdSe and $\text{CdS}_x\text{Se}_{1-x}$ nanobelts. Curves (a) and (i) are the PL spectra for CdS and CdSe respectively and curves (b)-(h) are the PL spectra for varying compositions of $\text{CdS}_x\text{Se}_{1-x}$ nanobelts. Reprinted with permission from Journal of American Chemical Society.[95]	34
3.8	(a) A fluorescence micrograph of the studied CdSSe nanowire on a TEM grid. (b) The results of a color space analysis of the micrograph displaying the extracted emission wavelength in nanometers. (c) and (d) SEM images of the same nanowire. (e) EDS measurement for the bulk sample.[99]	37
3.9	a) A time-integrated open gate image displaying the luminescence along the nanowire in a false-color scale. (b) The integrated intensity at two different locations along the wire as a function of excitation fluence on a log-log plot.[99]	38
3.10	Measured luminescence transients from the single nanowire at two different excitation fluences (gray and blue markers) and the fits to the ASE model (solid) line at each fluence.[99]	40

4.1	(a) Model of the wurtzite structure of ZnO, showing the tetrahedral coordination of Zn-O . (b) The three crystal facets of ZnO nanostructures (0001) $\{2\bar{1}\bar{1}0\}$, $\{01\bar{1}0\}$. Reprinted with permission from Elsevier. [137]	45
4.2	The common growth morphologies of one-dimensional ZnO nanostructures and the corresponding facets. Reprint permission granted by Elsevier. [137]	47
4.3	(a) SEM image of ZnO nanowire array grown via second VLS method. (b) Magnified image of a single ZnO nanowire showing the characteristic gold catalyst tip.	51
4.4	(a) and(b) SEM images of horizontally aligned ZnO nanowires grown via second VLS method.	52
4.5	SEM image Au droplets formed from the deposition of 6 nm layer onto silicon wafer using vacuum sputtering system.	54
4.6	Chart showing growth conditions and morphology for alkali method.	57
4.7	SEM images of ZnO nanostructures obtained with alkali hydrothermal method with ZnCl ₂ concentrations (a) 0.15 M, (b) 0.2 M, (c) 0.3 M and (d) 0.5 M. ((e)-(h) SEM images of nanostructures grown with increasing growth times of 10 , 15, 20, 30 hours respectively for fixed ZnCl ₂ concentration of 0.3 M and NaOH concentration of 4M. . . .	58
4.8	Idealized growth morphology of ZnO crystal. Reprint permission granted by Crystal Growth. [171]	60
4.9	SEM images of ZnO nanostructures grown with starting reagents 4 M NaOH and .2 M ZnCl ₂ (a) unstirred (b) stirred reactions. Inset shows the possible cause of the indentations observed. SEM images of ZnO nanostructures grown with starting reagents 4 M NaOH and .3 M ZnCl ₂ (c) non-stirred and (d) stirred reactions.	61
4.10	Chart showing growth conditions and morphologies for the solvothermal method.	63
4.11	SEM images of ZnO nanostructures grown via the solvothermal-colloid method with 1 M NaOH and 1 M Zn(NO ₃) ₂ at (a) 10 hours, (b) 15 hours and (c) 20 hours.	64

4.12	SEM images of ZnO nanostructures grown with 1 M Zn(NO ₃) ₂ ·6 H ₂ O and (a) 1 M NaOH and (b) 6 M NaOH. SEM images of ZnO nanostructures grown at (c) 200 °C and (d) 180 ° with a constant reactant concentrations.	65
4.13	Formation of twin crystal nucleus by the linkage of ZnO ₄ ⁻⁶ tetrahedral growth units by K ⁺ bridge. Reproduced with permission from John Wiley and Sons.[175]	66
4.14	SEM images of nanowires grown on the same wafer by the low temperature hydrothermal method.	68
4.15	SEM images of nanowires grown (a) with 0.005 M PEI and (b) without PEI in the growth solution.	69
4.16	Formation energies as a function of Fermi level for Zn-rich and O-rich growth conditions calculated using GGA + U method. Dotted line represents the conduction band minimum of ZnO. Reproduced with permission from Physical Review B .[195]	72
4.17	The formation energies as a function of Fermi level for Zn-rich and O-rich growth conditions calculated using LDA + U method. Reproduced with permission from Physical Review B .[119]	74
5.1	The instrument response function for YAG 0.5 mm and fused silica 0.5mm and 0.15 mm Kerr medium at 360 nm. Reprinted with permission from The Optical Society. [200]	76
5.2	(a) SEM image of a single ZnO nanowire. (b) Open-gate image of the same nanowire at (b) low fluence (4.4 mJ/cm ²) and (c) high fluence (13.2 mJ/cm ²). Reprinted with permission from SPIE.[207]	79
5.3	a) Power dependent emission spectra of the same ZnO nanowire. (b) The emission intensity dependence of the pump fluence. Reprinted with permission from SPIE.[207]	80
5.4	a)Time resolved spectrum of the same ZnO nanowire at (a) 14.9 mJ/cm ² and (b) 16.4 mJ/cm ² . Black dotted line shows the red-shift due to BGR with delay time.Reprinted with permission from SPIE.[207]	83

5.5	(a) Transient image sequence of a single ZnO nanowire excited at 16.4 mJ/cm ² . The red and yellow boxes demarcate region 1 and 2 respectively. (b) Transient dynamics extracted from region 1 on the nanowire at fluences ranging from 9.7 mJ/cm ² to 16.4mJ/cm ² . Reprinted with permission from SPIE.[207]	86
6.1	Scheme showing the amplified spontaneous emission rate model. The N_1 is excited initially and then relaxes to the N_2 state at the band edge at a rate of γ_r . The rate of loss of photons due to radiation is given by γ_Φ . The photon field population ($\Phi(t)$) and the carrier population in N_2 are linked by a feedback mechanism that results in oscillations in the emission intensity. The three competing recombination pathways Shockley-Read-Hall (γ_s), non-geminate (γ_d) and auger (γ_a) act to dampen these oscillations and serve as channels for non-radiative recombination.	91
6.2	(a) Scanning electron microscopy image of the single ZnO nanowire measured in this study. Loose ZnO debris particles on the surface of the nanowire were from sample preparation and are not apart of growth morphology. False-color fluorescence micrographs at (b) 7 mJ/cm ² and (c) 14 mJ/cm ² . Discrete regions of enhanced emission are observed on the nanowire above the the threshold fluence of 5.5 mJ/cm ² .(d) Power dependent emission spectra (inset: the power dependence of emission with excitation intensity) and (e) The power dependence of the emission with excitation intensity.	94
6.3	(a) False-color luminescence images of the single ZnO nanowire at different delay times after excitation at 18.2 mJ/cm ² in transient mode. The two colored boxes at 0.5 ps represent the end facets of the nanowire. (b) The corresponding SEM image of the nanowire and the location of the regions (Region 1 and 2) of interest with respect to the debris particles on the surface. (c)and (d) The extracted transient dynamics from region 1 and 2 at excitation fluences 11.5-18.2 mJ/cm ²	96
6.4	(a) Transients extracted from each region depicting the evolution of the emission and the relative emission intensity at a fluence of 18.2 mJ/cm ² . (b) Normalized emission transients from each region showing the change in emission dynamics at each location on the nanowire.	97

6.5	(a)-(b) The red and green markers represent the transient dynamics extracted from each region at high (18.2 mJ/cm^2) and low excitation (11.5 mJ/cm^2) fluences respectively. The fit to the ASE model is represented by the blue line.	99
6.6	(a) Diagram of the energy levels of the intrinsic defects and defect complexes that induce absorption in the base of the nanowire. (b) Schematic of the two non-radiative trap-assisted Auger recombination mechanisms which reduce the intensity of emission at Region 2. (c) Defect mediated recombination mechanisms at a defect state acting as a recombination center (RC).	104
6.7	(a) FDTD computational domain showing the propagation direction of the Gaussian pulse source perpendicular to the long axis of the nanowire. (b) Electrical field intensity distribution of the long axis cross-section of the nanowire (Scale represents $1 \mu \text{ m}$).	108
6.8	(a)-(d) SEM-CL images of the tip and base of the nanowire for bandedge emission (blue) and visible emission (green) respectively. White box represents region where integrated intensity was measured for each region.	110
6.9	(a) SEM image of the nanowire and the location of all regions (Region 1-4) of interest. (b) Transient extracted from all regions at a fluence of 18.2 mJ/cm^2 (b) Transients extracted from region 3 and 4 at a fluence of 18.2 mJ/cm^2	111
A.1	Reprint permission for Figure 2.1, 3.3 and 3.6.	138
A.2	Reprint permission for Figure 3.2.	139
A.3	Reprint permission for Figure 3.7.	140
A.4	Reprint permission for Figure 5.1.	141
A.5	Reprint permission for Table 4.1.	142
A.6	Reprint permission for Figure 4.1 and Figure 4.2.	143
A.7	Reprint permission for Figure 5.2, Figure 5.3, Figure 5.4 and 6.3.	144
A.8	Reprint permission for Figure 4.8.	145

A.9	Reprint permission for Figure 4.13.	146
A.10	Reprint permission for Figure 4.17.	147
A.11	Reprint permission for Figure 4.16.	148

ABSTRACT

Single nanostructures are predicted to be the building blocks of next generation devices and have already been incorporated into prototypes for solar cells, biomedical devices and lasers. Their role in such applications requires a fundamental understanding of their opto-electronic properties and in particular the charge carrier dynamics occurring on an ultrafast timescale. Luminescence detection is a common approach used to investigate electronic properties of nanostructures because of the contact-less nature of these methods. They are, however, often not equipped to efficiently measure multiple single nanostructures nor do they have the temporal resolution necessary for observing femtosecond dynamics. This dissertation intends to address this paucity of techniques available for the contact-less measurement of single nanostructures through the development of an ultrafast wide-field Kerr-gated microscope system and measurement technique. The setup, operational in both the steady state and transient mode and capable of microscopic and spectroscopic measurements, was developed to measure the transient luminescence of single semiconductor nanostructures. With sub micron spatial resolution and the potential to achieve a temporal resolution greater than 90 fs, the system was used to probe the charge carrier dynamics at multiple discrete locations on single nanowires exhibiting amplified spontaneous emission. Using a rate model for amplified spontaneous emission, the transient emission data was fitted to extract the values of the competing Shockley-Read-Hall, non-geminate and Auger recombination constants. The capabilities of the setup were first demonstrated in the visible detection range, where single nanowires of the ternary alloy $\text{CdS}_x\text{Se}_{1-x}$ were measured. The temporal emission dynamics at two separate locations were compared and calculation of the Langevin mobility revealed that the large carrier densities generated in the nanowire allows access to non-diffusion controlled recombination. In the

second phase of this study the setup was configured to the ultraviolet detection range for measuring the nanowires of conductive metal oxides. ZnO was the metal oxide of focus in this research. Ultrafast measurements were conducted on ZnO nanowires and ASE dynamics from multiple regions along a nanowire were again fitted to the ASE model and the recombination constants extracted. The diminished influence of the Shockley-Read-Hall recombination rate on the measured luminescence suggested that leading quadratic term in the model is a measure of a two-body defect mediated recombination rate, from which a defect density could be calculated. The measured change in defect density along the length of the nanowire correlated with changes in the growth conditions that established a defect gradient. The results show that the Kerr-gated system, as well as being a probe of ultrafast dynamics, is also a new tool for measuring changes in defect density in single nanostructures.

Chapter 1

INTRODUCTION

The technological trend of continued miniaturization of electronic and photonic devices has been the impetus for semiconductor nanomaterial research for the past two decades. Their unique optical, electronic, thermal and mechanical properties have made them excellent candidates for applications such as sensors, lasers, solar cells, transistors, nanoelectronic circuits, batteries and novel devices for interfacing with live cells.[1, 2, 3, 4, 5] The work towards energy conversion applications of nanomaterials, particularly solar cells, has risen rapidly alongside the use of solar generated power (Figure 1.1). The projected upward climb in the demand for solar cells will continue to drive the investigations in this field as research tries to address issues such as stability, lower cost materials, size and most importantly the need for greater power conversion efficiency.

Since the seminal paper by O'Regan and Grätzel written in 1991,[6, 7] dye-sensitized solar cells (DSCs) have emerged as a major competitor of solid-state junction devices.[8] With economical device fabrication, better performance under diffuse and ambient lighting and increase design flexibility, DSCs are an attractive alternative to the traditional photovoltaics.[8, 9] Figure 1.2 shows a schematic of typical DSC. The device is centered around a mesoporous metal oxide layer (10-30 nm), typically anatase TiO_2 , composed of nanometer-sized particles sintered together to allow electronic conduction. The oxide layer is deposited onto a transparent substrate usually fluorine-doped tin oxide coated glass. A charge transfer dye is attached to the surface of the nanocrystalline film. When the dye is photoexcited an electron is injected into the conduction band of the metal oxide while the dye is left in a oxidized state. The dye is restored to the ground state by electron donation from an electrolyte. Regeneration of

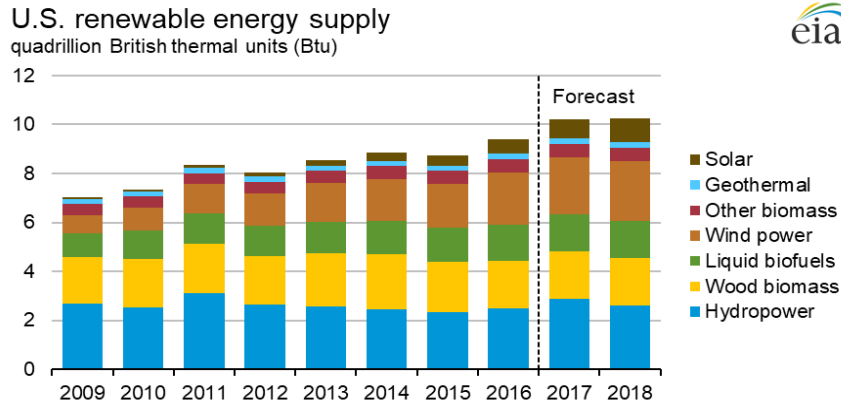


Figure 1.1: Renewable energy supply trends for the US. (From the U.S. Department of Energy, U.S Energy Information Administration Short-Term Energy Outlook report.)

the dye sensitizer by the electrolyte prevents recapture of the conduction band electron by the oxidized dye. The electrolyte itself is regenerated at the counterelectrode and the circuit is completed via electron migration through the external load.[10, 6, 7]

In pursuit of higher efficiencies researchers have often isolated and tackled the components of the DSCs separately. Currently, several thousands of dyes have been investigated,[7, 11, 12] hundreds of electrolyte systems,[13, 14, 15] and multiple configurations have been explored [16, 13] all in the effort to optimize the energy conversion process. Although the various components of a DSC are a well comprised orchestra, the metal oxide electrode is often referred to as the heart of the device.[6] Research on the metal oxide electrodes has involved either moving away from the thin film configuration towards nanowire arrays or using an alternative metal oxide to TiO_2 such as ZnO , SnO_2 and ZrO_2 or mixed combinations of these wide band-gap materials. [17, 18, 19] The nanowire array configuration promises to improve electron transport efficiency by providing a direct conduction pathway for electrons while maintaining a

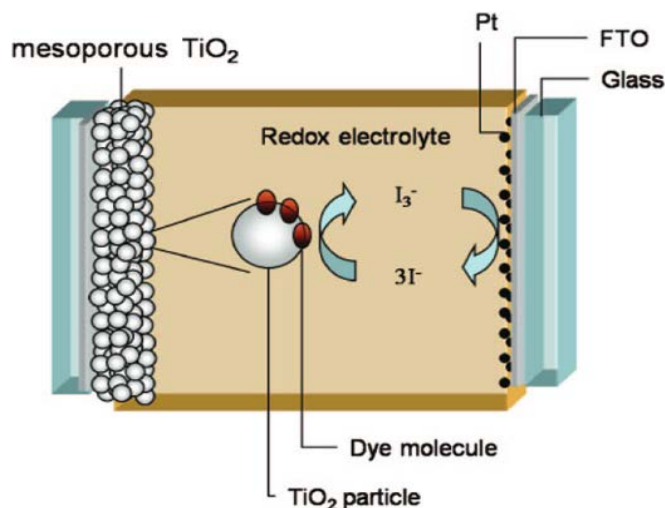


Figure 1.2: Schematic overview of a dye-sensitized solar cell. Reprinted with permission from. [7]

large surface area for dye adsorption. Additionally, nanowires can be synthesized at low temperatures without sintering.[20, 21] For replacing TiO_2 , the two most popular alternatives are ZnO and SnO_2 because they have similar band-gaps to TiO_2 , 3.4 eV and 3.8 eV for ZnO and SnO_2 respectively. The larger band-gap of SnO_2 is less likely to generate holes in the valence band by direct photon absorption and should be more stable under UV illumination than devices made from TiO_2 and ZnO . The most promising feature of these alternative metal oxides is their large electron mobilities. The bulk electron mobilities of ZnO ($200 \text{ cm}^2/\text{Vs}$) [22, 23] and SnO_2 ($250 \text{ cm}^2/\text{Vs}$) [24] are two orders of magnitude larger than that of TiO_2 ($1 \text{ cm}^2/\text{Vs}$).[25]

Despite the theoretically favorable features of a nanowire DSCs design, both alternative metal oxide electrodes and the nanowire array arrangement have lagged behind with respect to power conversion efficiency compared to the original TiO_2 nanocrystalline thin film design. This raises two pertinent questions that are without satisfactory answers. The first is why are photovoltaic devices with metal oxide

nanowire arrays, although structurally conducive to better electron transport, less efficient. The second is why does the higher bulk electron mobility in ZnO and SnO₂ not translate to higher efficiency and better performance for devices made with these materials. These questions reveal gaps in the knowledge base in the field of carrier dynamics in metal oxide nanostructures. Answering these questions requires the ability to efficiently measure the charge carrier dynamics of single nanowires occurring on a ultrafast timescale.

This dissertation lays the ground work to address these discrepancies from the perspective of the metal oxide single nanowire by establishing the instrumentation and method for characterizing single nanostructures and investigating single nanostructures. Specifically, a femtosecond Kerr-gated microscope system with both steady state and transient modes was built to detect the luminescence dynamics of single nanostructures occurring within the first few picoseconds after excitation. Amplified spontaneous emission (ASE) from single nanowires was fit to a kinetic model where the recombination rates and charge carrier mobility can be extracted.

Although the broader goal of this project is to ultimately compare the charge carrier dynamics of the three main metal oxides (TiO₂, ZnO and SnO₂), this research initiates the study with cadmium sulfide selenide (CdS_xSe_{1-x}). CdS_xSe_{1-x} is also a technologically important semiconductor material and its tunable band-gap for visible emission made it an excellent candidate for ultrafast measurements within the visible detection range. As the scope of this project is so large, this dissertation only focuses on one of the metal oxides, ZnO. After conversion of the optical setup to the ultraviolet detection range, ultrafast measurement of single nanowires of ZnO were conducted to gain insight into the electronic properties of individual nanowires. The thesis is organized in the following order:

The rest of **Chapter 1** looks at techniques for measuring the charge carrier dynamics in single nanowires, specifically the Kerr-gated microscopy technique used this in this work. The ASE model used to fit the transient data is explained and the main objectives of this dissertation is highlighted.

Chapter 2 presents the experimental methods. It focuses on the experimental setup of the Kerr-gated microscope and the laser system. The specific components that were used to optimize temporal resolution are detailed, the microscopic and spectroscopic modes of operation are outlined as well as the steps towards conversion to the ultraviolet detection range. The preparation methods and strategies of nanowire samples is also highlighted.

Chapter 3 introduces cadmium sulfide selenide semiconductor nanomaterial and the preliminary ultrafast measurements with the Kerr-gated setup in the visible detection range. Position-dependent charge carrier dynamics in a single nanowire is introduced and the capability of the setup to resolve these locations is demonstrated. The charge carrier mobility is calculated from the leading non-geminate term after applying the ASE model to the transient data.

Chapter 4 serves as an in depth introduction into ZnO semiconductor properties and synthesis to facilitate a discussion on the ultrafast dynamics of ZnO nanowires that is presented in the upcoming chapters. The chapter also shows the solution based synthesis studies conducted and the morphologies obtained.

Chapter 5 is the first chapter on measurements conducted in the ultraviolet range of detection. The chapter looks at Kerr medium selection for the new configuration and presents the preliminary measurements on ZnO. The aim of this chapter is to present the capabilities of the instrument in the UV detection range. The increased signal, due to the higher Kerr efficiency, that allows for observation of ultrafast phenomenon and subtle changes in emission wavelength from different locations on a single nanowire are also demonstrated.

Chapter 6 continues the work in Chapter 5 with the measurement of a single ZnO nanowire and the fitting of the transient data to the ASE model. The fit of the ASE model showed that the Shockley-Read-Hall recombination rate had little influence over the emission and could be omitted. The remaining competing de-excitation pathways, the non-geminate and Auger, represent the different types of defect assisted recombination pathways. The leading non-geminate term was then a measure of the

two-body defect assisted recombination rate. From the model, the defect density gradient established by the synthetic method, was measured along the nanowire length.

1.0.1 Measuring the electronic properties of nanostructures

The extensive work done on nanomaterials has led to great advances being made in the synthesis of highly crystalline nanostructures. This means that a high degree of selectivity, with respect to morphology and properties, can be employed depending on the specific application.[26, 27] Techniques to measure the electrical properties of nanostructures have also developed concomitantly. Being able to control the electrical properties through synthesis and subsequently measure these properties accurately is of paramount importance to the development of novel devices. Single nanowires are typically characterized by conventional electrical transport measurements such as Hall effect measurements, which are more appropriately used for planar layers. Hall effect measurements require a specific contact geometry made to the single nanowire which is challenging to apply.[28, 29] Similarly, field effect transistor (FET) measurements, the most commonly used method for measuring the transport properties of single nanowires, also requires complex contacts to be made to the nanowire. The contacts themselves have specific requirements with respect to the nature (Ohmic or Schottky) and resistance and so are often costly and time consuming to construct.[28] Additionally, assumptions used to model a FET device and uncertainties in the gate capacitance can heavily influence the interpretation of the data and create systematic errors or artifacts.[30, 31]

Contact-less techniques are therefore more appropriate for measuring nanowires. Arrays of nanowires in devices have commonly been characterized by photoresponse such as fluorescence-loss and THz time-domain spectroscopy. Although THz time-domain spectroscopy can directly probe charge carrier lifetimes, mobilities and dopant concentrations with subpicosecond time resolution,[28] the technique relies on ensemble averaging and is not sensitive enough for single nanowire measurements. The capability to measure single nanowires is essential as nanowire arrays tend to vary in size,

morphology and composition. Averaging over these variations negates a fundamental understanding of carrier dynamics on the single nanowire scale. Other contact-less methods such as Kelvin probe force microscopy involving scanning and are restricted to a small number of samples and hence measurement time is increased.[32]

Luminescence detection techniques have managed to overcome many of the previously mentioned hindrances with the additional advantage of temporal signal detection.[33, 34, 35, 36, 37] Ultrafast microscopy provides a highly useful route to visualize and elucidate morphology-property relationships in single nanostructures.[38, 39, 33, 36] Ultrafast optical gating in particular, is a versatile alternative to other luminescence detection methods because it can combine the imaging capabilities, femtosecond time resolution and spectroscopy. Optical Kerr-gating has primarily been used for time resolved spectroscopy.[40, 41, 42, 43] The available literature on Kerr-gated systems is modest, with only a few research groups currently publishing.[42, 44, 45] An even smaller number of these groups have the combined imaging with the spectroscopic capabilities.[46] Collectively, none of these groups have managed to surpass a temporal resolution better than sub 100 ps. The Kerr-gated system in this study is therefore unique in that it has a wide-field microscope, sub 90 fs time resolution, spectroscopic capabilities and can be operated in both steady state and transient modes. The measurement capabilities of the system therefore have the potential to measure temporal dynamics on timescales inaccessible with other systems.

1.1 Amplified Spontaneous Emission

Adopting a luminescence detection approach to probing the electronic properties of single nanostructures, processes such as amplified spontaneous emission can be observed. Amplified spontaneous emission (ASE), also referred to as mirror-less lasing, is an important phenomenon readily observed in nanostructures.[47, 48, 49, 50, 2] In ASE when a certain excitation threshold is surpassed, a spontaneously emitted photon passes through a gain medium, the spontaneous emission is then strongly amplified through a stimulated process. Generally, the main prerequisites for observation of ASE

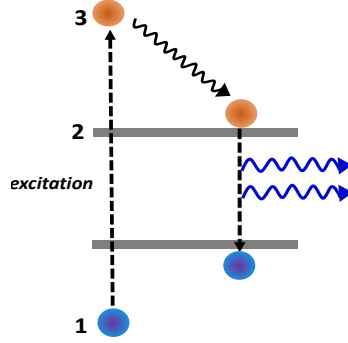


Figure 1.3: Schematic of the electron transition in the ASE process.

is that a volume of gain medium be excited above a threshold.[51] These conditions are less stringent than observation of lasing in nanostructures where a pristine cavity configuration for positive feedback is often required.[52, 51] Lasing and ASE are sometimes used interchangeably as both phenomenon involve stimulated processes. Observation of lasing in nanostructures is, however, more difficult unless extensive presorting of nanostructures or nano-manipulation by facet cleaving are utilized.[53, 54, 55, 56, 27] The transition from spontaneous emission to ASE is characterized by a superlinear increase in luminescence intensity that is highly directional, spectra line width narrowing, and in some cases re-broadening and a red shift in the emission spectra.[57, 47, 49, 58] In addition to a lack of a cavity, ASE can be distinguished from lasing by the absence of longitudinal and transverse modes in the emission spectra.[51]

If a nanowire system is considered to be a three-level laser, then the electron transition can be described by the schematic in Figure 1.3. When excited, electrons transition from the valence band (1) to the conduction band (3), relax to the band edge (2) before finally returning to the valence band generating spontaneous emission. ASE will occur when the excitation is high enough for the gain to be more than the loss in the light propagation process at a sufficiently high excitation intensity. This inversion population threshold for ASE, where the nanowire is considered an ensemble of atoms in a uniform column of length l , is expressed as [51, 52]

$$\Delta N = \frac{8\pi\nu_0^2\Delta\nu_0\tau_S}{lc^2\phi} \quad (1.1)$$

where ν_0 is the peak frequency of spontaneous emission, $\Delta\nu_0$ is the linewidth, τ_S is the lifetime of the excited state, c is the velocity of light in vacuum and ϕ is the branching ratio.

The kinetic rate model for describing the ASE process is described by the following first-order non-linear coupled differential equations [59]

$$\begin{aligned} \frac{d}{dt} N_1(t) &= AV_p(t) - \gamma_r N_1(t) \\ \frac{d}{dt} N_2(t) &= \gamma_r N_1(t) - B\Phi(t)N_2(t) - \gamma_s N_2(t) - \gamma_g N_2(t)^2 - \gamma_a N_2(t)^3 \\ \frac{d}{dt} \Phi(t) &= B\Phi(t)N_2(t) - \gamma_\Phi \Phi(t) \end{aligned} \quad (1.2)$$

N_1 is the highly excited carrier density created by the Gaussian pump pulse V_p which has an amplitude A . N_1 decays at a rate of γ_r via carrier phonon scattering, into the carrier density at the band edge, N_2 . At pump fluences above the ASE threshold, a spontaneously emitted photon on its way through a crystal will give rise to stimulated emission. It is the stimulated emission that gives the feedback between N_2 and the density of the photon field (Φ) and accounts for the coupled nature of these two terms. The feedback is given by the term $B\Phi(t)N_2(t)$. γ_s , γ_g , and γ_a are competing decay pathways due to the linear Shockley-Read-Hall, quadratic non-geminate and cubic Auger recombination, respectively. γ_Φ accounts for the loss of photons from the active area due to radiation. B is the stimulated emission rate. It will be shown in chapter 6 that the quadratic term can also be a measure of the defect mediated recombination rate.

The signal that is recorded by the microscope is the temporal dependence of the photon field (Φ). The fit of this measured signal with the ASE model allows the different recombination constants, i.e. Shockley-Read-Hall rate, non-germinate radiative rate and Auger rate, which result in 1st, 2nd and 3rd order kinetic contributions,

respectively, to be extracted. The Shockley-Read-Hall rate is a measure of indirect recombination and is related to surface defect scattering. Assuming the Shockley-Read-Hall rate is the leading de-excitation pathway, then it can be used to calculate the charge carrier mobility by considering the momentum gained in a unit electric field (E) in between collisions given by the equation

$$-qE\bar{\tau} = m^*v_d \quad (1.3)$$

where m^* is the effective mass, q is the charge and $\bar{\tau} = 1/\gamma_s$ which is the Shockley-Read-Hall lifetime. The mobility can then be given as the ratio of the drift velocity to the applied electric field

$$\mu = \frac{v_d}{E} = -\frac{q}{m^*}\bar{\tau} \quad (1.4)$$

Since the electron mobility in low defect concentration bulk TiO_2 , ZnO and SnO_2 is more than a magnitude larger than the hole mobility it can be assumed that the Shockley-Read-Hall rate is a measure of the electron trapping at early delay times.[60, 61, 62] Alternatively, with a leading non-geminate recombination pathway the mobility can be obtained by considering the case of free electrons and holes undergoing either a diffusion controlled or non-diffusion controlled recombination.[63]

For high mobility solids, if the volume swept out by the carrier moving with a thermal velocity v_T in a scattering time τ_S encompasses a recombination center, recombination will occur and the recombination coefficient will be given by the equation

$$\gamma_g = v_T\sigma \quad (1.5)$$

where σ is the capture cross section. Essentially, for high mobility solid the condition $v_T\tau_S > N_r^{-1/3}$ needs to be met where N_r is the density of carriers. This recombination is not diffusion limited. On the other hand for a low mobility solid where the Coulomb radius r_c is much greater than the distance traveled by the charge carrier ($v_T\tau_S \ll r_c$) then the carrier which moves within the mutual Coulomb radius of an oppositely charge

carrier will suffer collisions before diffusing to recombination.[63] The recombination coefficient is then given by the equation

$$\gamma_g = e\mu_L/\epsilon \quad (1.6)$$

where μ_L is the Langevin mobility, e is the electron charge and ϵ is the dielectric constant. In this diffusion limited regime, the system can be modeled after Langevin recombination and the non-geminate relaxation rate is a measure of the Langevin mobility which is equal to the sum of the electron and hole drift mobilities ($\mu_L = \mu_e + \mu_h$).

1.2 Objectives

This study primarily focuses on ultrafast Kerr-gating method development and aims to establish and optimize a robust, contact-less technique by which single nanostructures can be characterized by ultrafast spectroscopic and microscopic methods. From this foundation, meaningful studies on single nanostructures be performed. The characterization involves interpreting the early femtosecond luminescence dynamics to gain insight into the recombination processes that influence the measured signal, determining what these recombination pathways reveal about the material and conversely how synthetic methods may affect these recombination pathways.

To do this the first measurements extrapolate on previous work by measuring single $\text{CdS}_x\text{Se}_{1-x}$ nanowires with the setup configured for detection in the visible spectrum. The carrier dynamics of discrete regions on a single nanowire were measured and recombination rates extracted. From the extracted recombination rates a value for the charge carrier mobility will be calculated and compared to literature reports. Additionally, the origin of the position specific dynamics is investigated.

In the next step, the setup is converted to the ultraviolet detection range for measurement of the metal oxide nanostructures. As the main metal oxide of focus in this study, ZnO nanowires were then measured to investigate position specific occurrences of ASE dynamics. The carrier dynamics from multiple discrete regions exhibiting

ASE were extracted and compared by fitting to the ASE model. From the extracted rates determine links between synthesis, morphology and early luminescence dynamics in a single ZnO nanowire.

Chapter 2

EXPERIMENTAL METHODS

The primary objectives of this study, outlined above, were to measure the ultrafast dynamics of single nanostructures. For this, the instrumental requirements were micron or greater spatial resolution for resolving single nanostructures, femtosecond time resolution for accessing the ultrafast luminescence dynamics and spectroscopic capabilities. The experimental setup described below provides all of these features and is the center of the proposed contact-less technique. Sample preparation was also very important for obtaining transient measurements. The different sample preparation procedures and particle location strategies are also discussed.

2.1 Ultrafast Kerr-gated Microscope

The experimental setup for the Kerr-gated microscope consists of three major components, the source of the ultrafast pulses, the excitation wavelength selector and the microscope optical train with Kerr-gate and spectrometer. Figure 2.1 shows the schematic of the setup in its entirety.

2.1.1 Kerr-electro-optic effect

The Kerr-gate is the heart of the Kerr-gated system. The operation of the optical Kerr-gate is based on the Kerr-electro-optic effect. Discovered in 1875 by the Scottish physicist John Kerr¹, the Kerr effect is essentially the change in refractive index with a change in static electric field. It was decades later in 1963 that researchers discovered

¹ John Kerr published this work in two communications to the Philosophical Magazine in 1875. He described his success in performing experiments to observe this change in isotropic medium, a task Faraday failed to do.[64, 65]

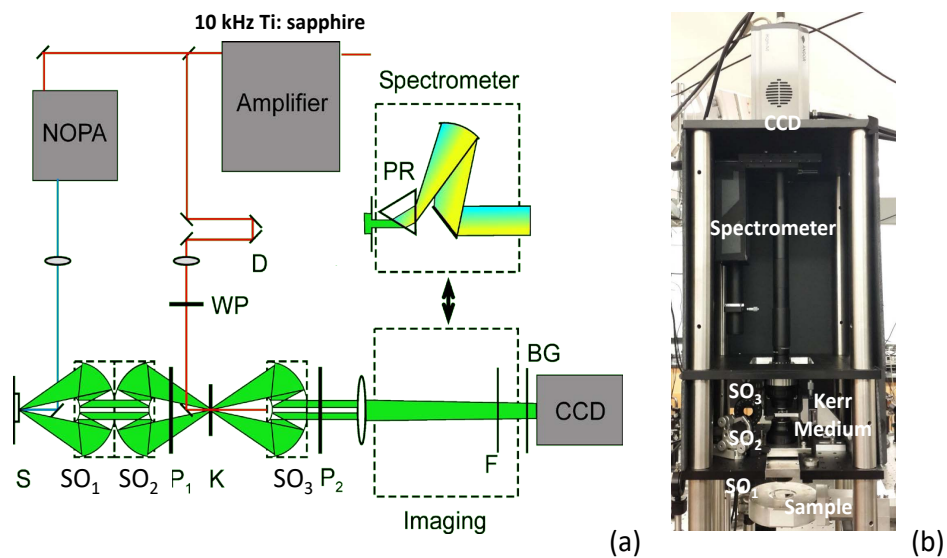


Figure 2.1: (a) Schematic of the Kerr-gated microscope setup. S: sample, SO_{1-3} : Schwarzschild objectives, P_{1-2} : polarizers, K: Kerr medium, D: delay line and F, BG: spectral filters, WP: waveplate and PR: prism. Reprinted with permission from American Chemical Society [59]. (b) Photograph of the optical column of the microscope.

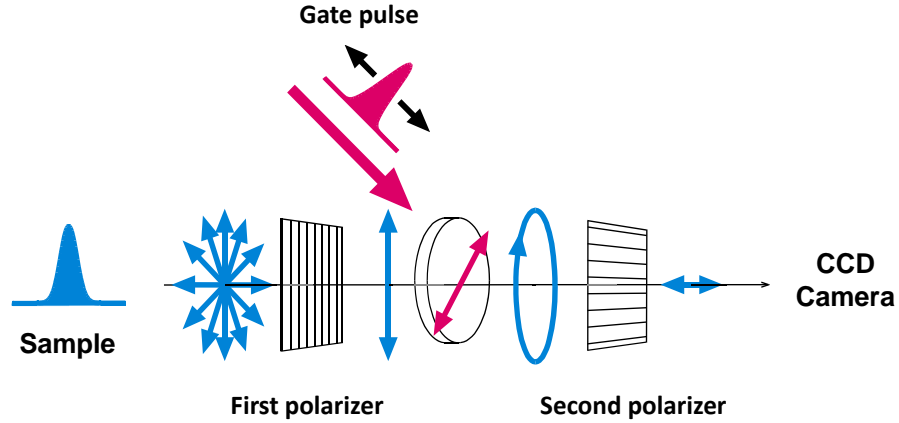


Figure 2.2: Schematic of the Kerr-gate showing the polarizers in the crossed (closed-gate) position.

that an optical electromagnetic field could also modify the dielectric properties and induce birefringence.[66] The development of the chirped pulse amplification technique was next pivotal moment in the time line of Kerr-gating techniques. With pulsed lasers researchers could induce transient birefringence in a Kerr medium and hence measure the relaxation process in the Kerr medium itself as well as track the dynamical response in other systems.[67] Further improvements in pulsed laser sources has made optical Kerr-gating a reliable method for investigating transient phenomena.

The Kerr-electro-optic effect is the light-induced change in birefringence of a substance. When intense light propagates in crystals, glasses or certain gases and liquids, there is a change in the refractive index in response to an electric field. The refractive index of materials can be described by the equation[68]

$$n = n_0 + n_2 I \quad (2.1)$$

where n_0 is the weak field refractive index, n_2 is the second-order index of refraction which gives the rate at which the refractive index increases with increasing optical

intensity and I is the time averaged intensity. The change in the refractive index is therefore,

$$\Delta n = n_2 I \quad (2.2)$$

this equation can also be written in the expanded form

$$\Delta n = \lambda_0 K \langle E_0(t)^2 \rangle \quad (2.3)$$

where λ_0 is the vacuum wavelength of the gate pulse, K is the Kerr constant and $\langle E_0(t)^2 \rangle$ is the time average of the electric field of the gate pulse. Figure 2.2 shows the schematic of the optical Kerr-gate. The gate is the core of the setup and consists of a Kerr medium between two polarizers integrated into the optical train of the microscope. When the short, intense pulses of the gating beam impinge on the Kerr medium there is a phase shift in the orthogonally polarized components of the incident light leading to temporarily elliptically polarized light. Maroncelli et al. [40] provides an excellent derivation of equations that define the operation of a Kerr-gate. If the static equivalent of the Kerr-gate, a retardation plate is considered, then the difference in the phase shift imparted on the light polarized along the slow and fast (s,f) axes of the retarder is

$$\phi = \phi_s - \phi_f = 2\pi L \Delta n / \lambda \quad (2.4)$$

here L is the thickness of the retardation plate, Δn is the static birefringence and λ is the wavelength of the incident light. Transmission through a retardation plate between a pair of crossed polarizers is given by

$$T = \sin^2(2\theta) \sin^2(\phi/2) \quad (2.5)$$

where θ is the angle between the slow axis of the retardation plate and the output polarizer direction. Replacing the static birefringence with the time dependent change

in refractive index and rotating the polarization of the gate pulse to $\theta = 45^\circ$ the transmittance becomes

$$T = \sin^2 \left(\frac{\phi(t)}{2} \right) = \sin^2 \left(\frac{\pi L \Delta n}{\lambda} \right) \quad (2.6)$$

Since ϕ depends on Kerr medium thickness, birefringence and wavelength, the ideal combination of these parameters can yield maximum transmittance. The choice of Kerr medium material and size is indeed one of the more critical aspects of optical Kerr-gating. Additionally, spatial and temporal overlap of the signal and gate beams and the group velocity dispersion and group velocity mismatch of the beams in the Kerr medium can affect the efficiency and temporal resolution of the setup. These parameters are discussed in more detail in chapter 5.

It is important to note that the setup is only functional as a gate or shutter when the polarizer pair is in the crossed position. The crossed polarizers prevent light emitted from the sample from being detected unless the gate pulse is present. In the parallel position, the gating capability of the setup is removed and only steady state measurements are possible.

2.1.2 Laser system

The laser system that provides the ultrashort pulses is comprised of a Ti:sapphire femtosecond oscillator (Coherent Mantis) and a regenerative amplifier (Coherent Legend-Elite). Pulses from the oscillator are stretched in the amplifier before being amplified in a Ti:Sapphire crystal. The Ti:sapphire crystal is pumped by a Nd:YLF (Coherent Evolution) laser. The pulses are then compressed to 38 fs pulses centered at 800 nm with a repetition rate of 10 kHz and 620 μJ energy.

The output from the amplifier is split to power a two-stage Non-collinear Optical Parametric Amplifier (NOPA) and to provide the gating beam of the optical Kerr-gate. Optical parametric amplifiers generate tunable energy pulses from the output of the Ti:sapphire laser system which is limited to the fundamental 800 nm. In Optical parametric amplification (OPA) a higher input frequency (ω_1), the pump beam, amplifies

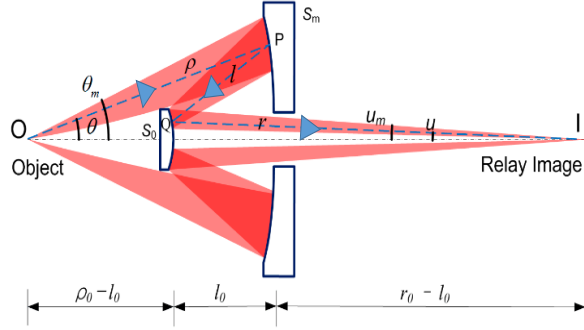


Figure 2.3: Diagram of a Schwarzschild objective.[69]

a lower frequency beam ω_2), the signal, and a third beam is generated (ω_3), the idler and energy is conserved. OPA is governed by the expanded equation

$$P(\omega_1 - \omega_2) = 2\epsilon_0\chi^{(2)}E_1E_2^* \quad (2.7)$$

where P is one of the complex amplitudes of the second-order contribution to the nonlinear polarization, ϵ_0 is the permittivity of free space, $\chi^{(2)}$ second order nonlinear optical susceptibility and E_1 and E_2^* are the electric field and the complex transpose of the electric field. [68] Only noncentrosymmetric crystals, crystals without inversion centers, can exhibit $\chi^{(2)}$ processes. The NOPA in this setup used β -barium borate (BBO) crystals and generated 25 fs pulses at 580 nm. Second-harmonic generation, another $\chi^{(2)}$ process, was used to double the output frequency from the NOPA in another BBO crystal to provide 290 nm excitation pulses to the sample.

2.1.3 Microscope optical setup

The schematic in Figure 2.1(a) shows that three identical, all-reflective Schwarzschild objectives²(SO_x) (Davin Optronics x36 Reflecting Objectives, NA= 0.5) were used. Schwarzschild objectives (2.3) consist of two spherical mirrors, one concave and the one convex, with coincident curvature centers.[72, 73] The mirrors are on-axis with a hole in one mirror for the light to pass through.³ Compared to their glass counterparts, Schwarzschild objectives aid in minimizing group velocity dispersion and increase the time resolution of the system by reducing the optical elements through which the light has to travel. Additionally, considering the simplicity of the design, it provides a wide field of view and excellent imaging characteristics. [74]

Figure 2.1 shows that the excitation pulse from the NOPA is directed onto the sample (S) via a small mirror on the first Schwarzschild objective (S_1). Fluorescence emitted from the sample is collected by the first objective passed through the first polarizer (P_1) (ProFlux High contrast polarizers, PPL04C) and focused onto the Kerr medium (K) via the second objective (S_2). Yttrium aluminium garnet (YAG) was used as the Kerr medium. The effects of changes in the Kerr medium material and thickness are discussed in chapter 5. The gate pulse (800 nm) is superimposed with the image of the sample luminescence with a second small mirror. A waveplate (WP) is used to rotate the polarization of the gate pulse by 45° . The recollimated light from the sample is collected by the third objective (S_3) before it passes through the second polarizer (P_2) (ProFlux High contrast polarizers, PFU04C). The recollimated light at this point is either imaged directly on a CCD camera (Andor Ikon-M 912) or dispersed

² The Scwharzschild objective was named after the German scientist Karl Schwarzschild (1873-1916). He published this work in the proceedings of the Gö ttingen observatory in 1905 with the original focus being calculation of aberration and optical system analysis. [70, 71]

³ The name Cassegrain objective is sometimes used interchangeably with the name Schwarzschild. The design of the Cassegrain objective is credited to the catholic priest Laurent Cassegrain in 1672. Apart from the fact that the Schwarzschild was invented 200 years after, the major distinguishing factor is there is no requirement for cocentricity in Cassegrain objectives. [74]

by a prism in a spectrometer. The spectrometer consists of a slit, a BK7 prism, two curved mirrors and a focusing lens. Lastly, a FGB37 bandpass filter was used to block any scattered 800 nm light from the gating pulse.

2.1.4 Ultraviolet Configuration

The original setup was specifically tailored for detecting visible light. The polarizers in particular were specified for a wavelength range of 420 nm- 700 nm. To allow measurement of the wide bandgap metal oxides that are the central focus of this study the setup needed to be configured for the ultraviolet detection range. The polarizers were replaced with ones with a contrast ratio in the UV, greater than 100,000:1, and transmittance better than 52% (Laser Components colorPol UV 380 BC4). The UV polarizers were also chosen as thin as possible (2 mm) as a measure to ensure that the time resolution is preserved in the configuration. An additional filter, a BG3 short pass filter, was also added to block any residual excitation light.

2.1.5 Modes of operation

The setup functions as both a steady state and transient microscope and spectrometer. In the steady state mode the polarizers are in the parallel configuration and all light is allowed to pass through continuously to be detected by the CCD camera. In the steady state mode fluorescence images and steady state spectra can be obtained. In transient mode, the polarizers are crossed and light is not transmitted unless the gate pulse is present. To obtain time-resolved measurements the gate pulse and the emission signal from the sample must overlap spatially and temporally in the Kerr medium. The time between the gate pulse and signal is delayed by changing the path length (D) (Figure 2.1(a)). In transient mode sequential images or movies and transient spectra are measured. The spectrometer, which is mounted onto a sliding track, can be moved in and out of the optical train of the setup in either steady state or transient mode.

2.2 Sample Preparation

Proper sample preparation was an integral step before ultrafast measurements. Ensuring that nanowires would be well separated, their exact locations on a substrate be repeatedly found and that each sample could be taken to subsequent characterization instruments were factors that needed to be taken into account during the preparation process. Parameters such as nanowire removal, deposition, dispersing solvent and measurement substrate were all considered before preparation.

Prior to deposition nanostructures that were epitaxially grown on a substrate needed to be removed. Removal was performed by either sonication, scratching the surface with a blade or plucking. The best removal approach depended on the nanostructure morphology. Sonication of an as-grown sample wafer in a solvent was reserved for samples with nanowires less than $10\ \mu\text{m}$ in length. Sonication is inherently destructive so this method produced single nanowires that were often too damaged to produce detectable luminescence. Surface scratching was best executed on nanowires that were greater than $10\ \mu\text{m}$ in length. This method, however, had the disadvantage of also removing the bulk layer of material that formed the base of epitaxially grown samples and would result in more clusters on the surface of the prepared sample. The plucking method proved to be the most superior removal technique. It involved plucking clusters of nanowires from a substrate surface with a tweezer and resulted in long nanowires with limited damage to the surface and fewer debris particles. The plucking method could only be performed on samples with exceptionally long nanowires $> 50\ \mu\text{m}$ and hence was seldom used. The nanowires removed from their original growth platforms were suspended in acetone after removal. Acetone proved to be the most appropriate solvent as the rapid rate of evaporation allowed samples to dry quickly and resulted in fewer water marks compared to ethanol.

The two methods were used to deposit nanowires onto substrates were the drop cast method and the electrospray method, Figure 2.2 (a) and (b) respectively. The drop cast method was predominantly used as it was the most rapid way to produce multiple well populated samples. In the drop cast method, nanostructures suspended

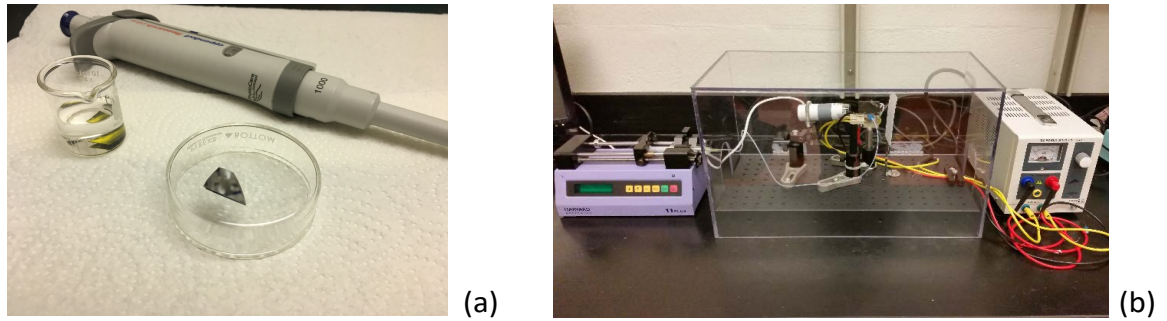


Figure 2.4: (a) Drop cast method where nanowires removed by either wafer sonication, scratching or plucking are suspended in acetone and deposited onto a clean silicon wafer. (b) The electro spray setup. Nanowires suspended in acetone are dispersed onto the substrate by applying a high voltage between a needle and clean substrate.

in acetone were pipetted onto the measurement substrate. Although the density of deposition could be controlled by either increasing the volume of solvent or decreasing the amount of nanostructures added to a fixed volume of solvent, the results were difficult to reproduce between samples and many nanostructures were deposited in clusters. The latter issue being the more severe of the two. Overlapping nanostructures or structures that had debris particles from other broken nanostructures often precluded single nanostructure measurements. Electro spray deposition provided the ideal solution to clustered deposition. The charge issued to nanostructures upon deposition rendered them repulsive to each other ensuring that the individual particles that were deposited were well spaced from each other. The major drawbacks of the electro spray deposition method were the small deposition area and that longer nanowires ($> 5 \mu\text{m}$) could not be deposited.

The choice of substrate was based on being able to characterize selected nanowires by scanning electron microscopy (SEM) and transmission electron microscopy (TEM) techniques after ultrafast measurements. The need for a conducting surface for SEM

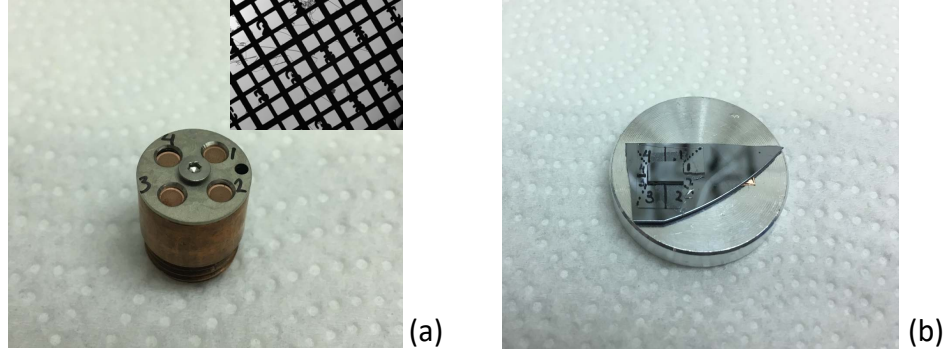


Figure 2.5: (a) TEM grid sample holder that allowed for ultrafast measurements and could be transferred directly to SEM measurements without removal of individual grids. Inset shows micrograph of labeled grid. (b) Sample on silicon wafer substrate where a second wafer was used to divide the sample into quadrants for relocating nanowires after ultrafast measurements.

and grid for TEM narrowed the selection to silicon wafers and copper TEM grids. Labeled TEM grids provided the added benefit of easier nanowire mapping but the curved surfaces of the bars caused some longer nanowires to bend and conform to the surface. This could result in observed delays in the emission from regions along the length of nanowire. Lastly, proprietary surface coatings of some TEM grids were found to quench the emission of $\text{CdS}_x\text{Se}_{1-x}$ nanowire samples prepared. To avoid this silicon wafers were primarily used especially for larger samples that were too thick (> 200 nm) for TEM.

Chapter 3

KERR-GATED MICROSCOPY IN THE VISIBLE DETECTION RANGE

In this chapter the operation of the Kerr-gated setup in the visible detection range is addressed. Cadmium sulfide selenide ($\text{CdS}_x\text{Se}_{1-x}$) nanowires were the semiconductor material used in the visible operation. Although a deviation from the metal-oxides at the center of this study, the technological significance of $\text{CdS}_x\text{Se}_{1-x}$, its optical properties and facile synthetic techniques made it an ideal material to explore carrier dynamics while the setup was configured for detection of visible luminescence. $\text{CdS}_x\text{Se}_{1-x}$ material properties, synthesis and the ultrafast measurements were performed on single $\text{CdS}_x\text{Se}_{1-x}$ nanowires are presented. The measurements highlight the spatial variation in carrier dynamics that can occur along a single nanowire as well as provide insight into the recombination mechanisms that affect the temporal luminescence.

3.1 Cadmium Sulfide Selenide Semiconductor material

CdS and CdSe are two very important wide band gap semiconductors. The combined product of the two creates the ternary alloy $\text{CdS}_x\text{Se}_{1-x}$. $\text{CdS}_x\text{Se}_{1-x}$ is one of the most important II-VI ternary compounds. It can assume a variety of different morphologies including nanowires, nanobelts and nanosheets.[75, 76, 77] In addition to the numerous available morphologies $\text{CdS}_x\text{Se}_{1-x}$, the real allure of this material is the tunable band gap. This wide band-gap chalcogenide compound can span the full visible spectrum by simply adjusting the mole fraction of S and Se mole in the chemical formula. The optical emission energy can be continuously tuned from 1.7 eV to 2.4 eV.[78] This property has made $\text{CdS}_x\text{Se}_{1-x}$ nanomaterial a prime candidate for

applications such as tunable wavelength source in semiconductor nanolasers,[79, 80] field effect transistors[81] and as light harvesters in solar cells.[82, 5]

3.1.1 $\text{CdS}_x\text{Se}_{1-x}$ Nanostructure Synthesis

The synthetic flexibility of the material has also allowed researchers to synthesize new structures with continuous alloy composition.[81, 3, 83] The graded band-gap structures have the added potential of resolving lattice mismatch problems of multi-junctions and the low conversion efficiency of solar cells.[81] These novel structures, just like the typical nanowires, were synthesized via a vapor phase transport method, vapor- liquid-solid (VLS) synthesis. VLS methods, compared to other vapor phase methods, are the simplest and most economical method to achieve highly crystalline nanostructures and hence is the most commonly used. The VLS process was established decades ago and has since been widely used a bottom-up approach to growth of nanowires.[84, 85, 86] First highlighted by Wagner et al., nanowires grown by the VLS mechanism possess a small globule at the tip of the nanowire during growth.[84] This globule found at the tip of nanowires is the metal catalyst. In the VLS process, the metal catalyst nanodroplets interact with gaseous reactants facilitating nucleation and growth.[87] The nanodroplet absorbs and becomes supersaturated with the reactant. The reactant then precipitates below the nanodroplet forming the nanowire. If the growth conditions are maintained then a straight nanowire perpendicular to the substrate can be obtained.[88] For $\text{CdS}_x\text{Se}_{1-x}$ nanowire growth the most common catalyst is Au. Catalyst type and size effects on growth are discussed in section 4.3.1 with respect to ZnO nanostructure growth.

The $\text{CdS}_x\text{Se}_{1-x}$ nanostructures in this study were grown on Si (111) wafers via the metal catalyzed VLS method adapted from Pan et al.[77] The experimental setup is shown in Figure 3.1. Equimolar portions of CdS and CdSe were mixed together in an alumina dish and placed at the centre of a quartz tube which was inserted into a horizontal tube furnace. Si (111) wafers, sputtered with a thin film of Au (30nm), were placed downstream of a constant high purity He flow (96 sccm). Insulation was used at

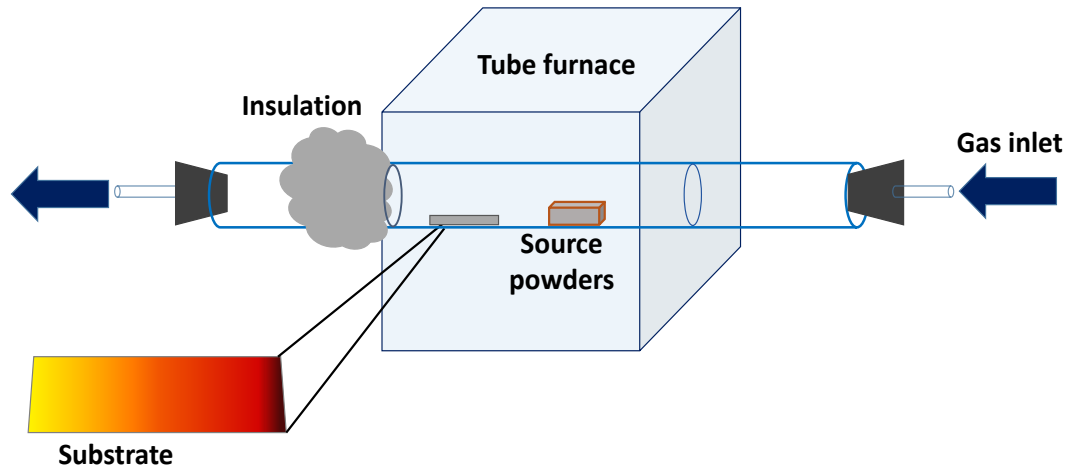


Figure 3.1: Experimental setup for VLS synthesis of $\text{CdS}_x\text{Se}_{1-x}$ nanostructures.

one end of the setup to create a less steep temperature gradient. The quartz tube was purged with O_2 at $100\text{ }^\circ\text{C}$ for an hour to prevent the preferential formation of metal oxides during the high temperature ramp cycle. The temperature of the center of the furnace was ramped to $900\text{ }^\circ\text{C}$ for an additional hour. The furnace was allowed to cool naturally before the sample was removed.

3.2 Ultrafast Measurements

3.2.1 Spatial Variation in Carrier Dynamics

Gundlach et al. reported on the ultrafast carrier dynamics in $\text{CdS}_x\text{Se}_{1-x}$ nanocrystal clusters.[59] The improved spatial resolution of the current setup allowed for these ultrafast measurements to be conducted on single nanowires as well as different locations along a single nanowire. At high excitation fluences amplified spontaneous emission (ASE) was observed in a single $\text{CdS}_x\text{Se}_{1-x}$ nanowire. The nanowire also exhibited position dependent variations in the ASE dynamics. Characterization by SEM

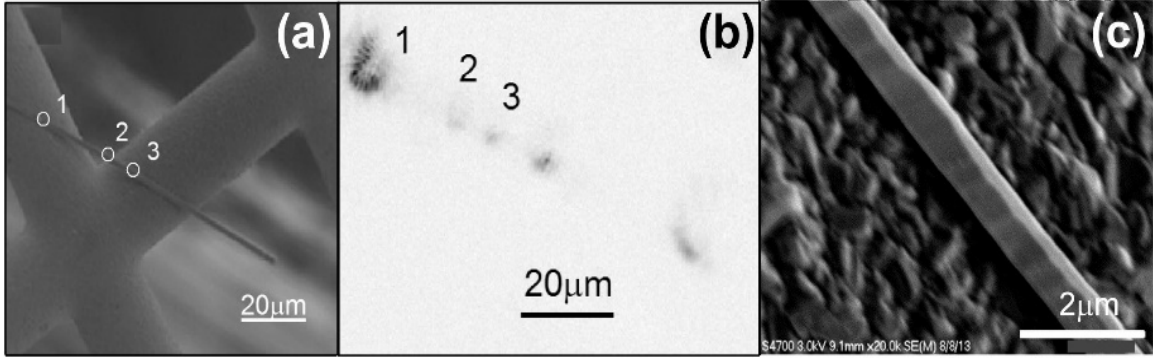


Figure 3.2: (a) SEM image showing a single $\text{CdS}_x\text{Se}_{1-x}$ nanowire resting on a TEM grid. (b) Fluorescence micrograph highlighting three regions of enhanced emission. (c) High resolution SEM image of the nanowire surface. Reprinted with permission from Elsevier.[89]

and color space analysis technique, discussed below, showed that these variations were not as a result of compositional changes in the nanowire. The differences in the dynamics can be attributed to changes in the recombination rates that dampen ASE oscillations. By modelling the ultrafast dynamics of ASE at each of the discrete locations it is possible to extract charge carrier scattering rates. In particular, the linear Shockley-Read term, which can be directly used to calculate charge carrier mobility. The measurement represents the first application of the ultrafast Kerr-gated microscope system as a sub-micron, contactless probe for charge carrier mobility in a single nanowire.

In preparation for ultrafast measurements, individual nanowires were isolated onto TEM grids as described in section 2.2. The TEM grid sample was evacuated in a vacuum cryostat and the measurements conducted at room temperature. The nanowires that were found to be unobstructed and free standing were identified. Figure 3.2 (a) shows the SEM image of one of the single nanowires studied, resting across the bars of a TEM grid. Three regions of interest were identified along the length of the

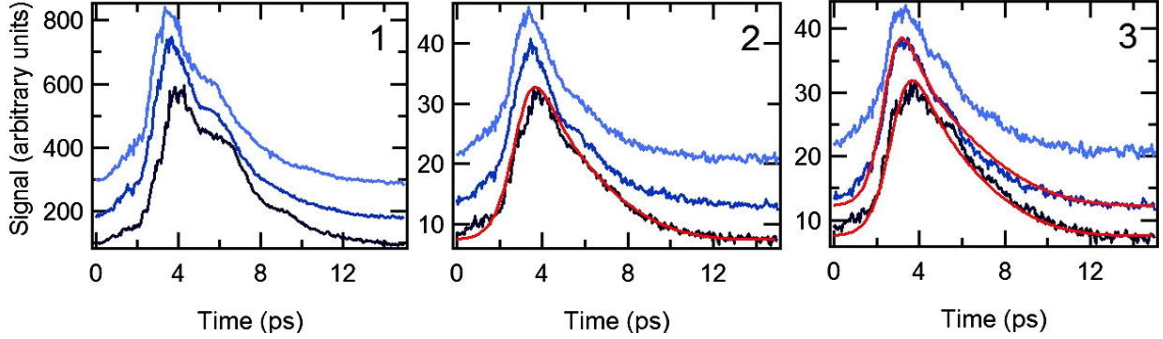


Figure 3.3: Integrated luminescence dynamics at three different locations on the single nanowire for excitation fluences 2, 2.6 and 3 mJ/cm². Red line shows fit with ASE model. Reprinted with permission from Elsevier.[89]

nanowire. Spot 1 and 3 are regions on the nanowire that coincide with the bars of the grid while spot 2 is located at a freely suspended region of the nanowire. The TEM grid allows for the same nanowire to be located again for post measurement characterization such as SEM. The SEM measurements were performed after the ultrafast measurements to prevent damage to the wire due to the electron beam. The high resolution SEM images show that the surface of the nanowire was slightly rough on the nanoscale but free of loose particles or contamination.

Figure 3.2 (b) is a luminescence image of the same nanowire excited at a fluence of 3 mJ/cm². As observed previously, a nonlinear increase in the emission intensity occurred above a certain threshold for a particular nanowire with increased excitation fluence.[59] This transition to enhanced emission was observed on the nanowire in the form of localized regions of enhanced emission. Surpassing the threshold facilitates the onset of non-linear luminescence dynamics which can be attributed to ASE occurring in the nanowire.

The wide field imaging mode of the Kerr-gated setup simultaneously records the

signal from the entire image field and hence all locations along the nanowire. Although the wide-field approach restricts the spatial resolution to being diffraction limited, it also makes it possible to measure more than one nanowire in the field of view under the same measurement conditions. The spatially resolved luminescence dynamics from different nanowires and different locations on the same nanowire can then be compared by extracting the time integrated signal after the measurement. Figure 3.3 shows the integrated transient emission collected at the three locations along the length of the nanowire, highlighted in Figure 3.2 (a) and (b), for the excitation fluences 2, 2.6 and 3 mJ/cm². In the extracted early luminescence dynamics only location 1 and 3 show a second maxima at 5-6 ps delay times. Spot 1 shows a more pronounced second maxima than spot 3. The red curves represent the preliminary fit to the ASE model.

The ASE model, details of which are given in section 1.1, is described by a set of coupled rate equations. The rate equations of the model predict oscillations in the emission. The second maxima observed in spots 1 and 3 are the first recurrence of the oscillatory signal. As stated previously, the non-radiative loss rates, γ_s , γ_g and γ_a , act to dampen the oscillations in the emission. The non-radiative loss rates as well as the carrier density are therefore the key parameters that influence the amplitude of the second maximum. While all three loss channels are necessary to reproduce the measurements, the linear Shockley-Read term is the leading term. The initial carrier density and the Shockley-Read relaxation time determine the amplitude of the second maximum in the measurements. The more prominent second maximum in spot 1 and 3 compared to spot 2 can therefore be attributed to either a higher initial carrier density generated in each of these locations or longer Shockley-Read relaxation times.

Higher initial concentrations in localized regions along the nanowire can result from either a higher excitation fluence at spot 1 and 3 or higher extinction coefficients at those locations. Differences in the excitation fluence can be eliminated as an explanation because of the size and nature of the excitation spot. The excitation spot had a Gaussian intensity profile and was approximately 100 μm . The spot size was much larger than the area that encompassed all three spots. Additionally, if the Gaussian

intensity profile is considered then the excitation fluence would have been higher at the center, the location of spot 2, where the measured ASE dynamics indicates a lower carrier concentration. It should be noted that amongst the several nanowires measured there was no noticeable correlation observed between ASE dynamics from locations on the nanowire resting on the grid bars to those freely suspended.

If the excitation fluence at all locations on the nanowire is constant then changes in the initial carrier densities could be explained by differences in the local extinction coefficients. Changes in the morphology, composition or growth orientation on the nanowire could result in changes in the extinction coefficient. Although this nanowire was too thick for crystallographic analysis via TEM, the SEM images (Figure 3.2) showed no apparent changes in morphology along the length connecting the three spots. A change in growth orientation of the crystal axis with respect to the polarization of the excitation is known to affect the extinction coefficient.[59] This change in growth orientation would manifest as a change in morphology such as kinks or steps along the length the nanowire. None of these features were observed in the SEM images.

To determine if compositional changes occurred along the length of the nanowire, a color space analysis technique was employed. Color space analysis uses the spectral properties of the color filters of an optical microscope to determine the emission wavelength from CCD camera images.[90] The color space analysis uses the CIE's 1931 color space to map the colors from a micrograph to specific wavelengths. Color matching functions ($\bar{x}(\lambda)$, $\bar{y}(\lambda)$ and $\bar{z}(\lambda)$), shown in Figure 3.4, are the numerical descriptions of the chromatic response of a standard observer. A standard observer being the average human's physical response in the fovea of the eye to changes in color. Color matching functions act as weight functions describing how much of each component is required to produce a pure color on the horizontal axis.[91, 92, 93] These color matching functions can be used to calculate tristimulus values that can then be mapped onto CIE 1931 color space (Figure 3.4 (b)).¹

¹ The International Commission for Illumination (Commission Internationale de l'Éclairage, CIE) held a meeting at Cambridge in September of 1931 to establish five resolutions that

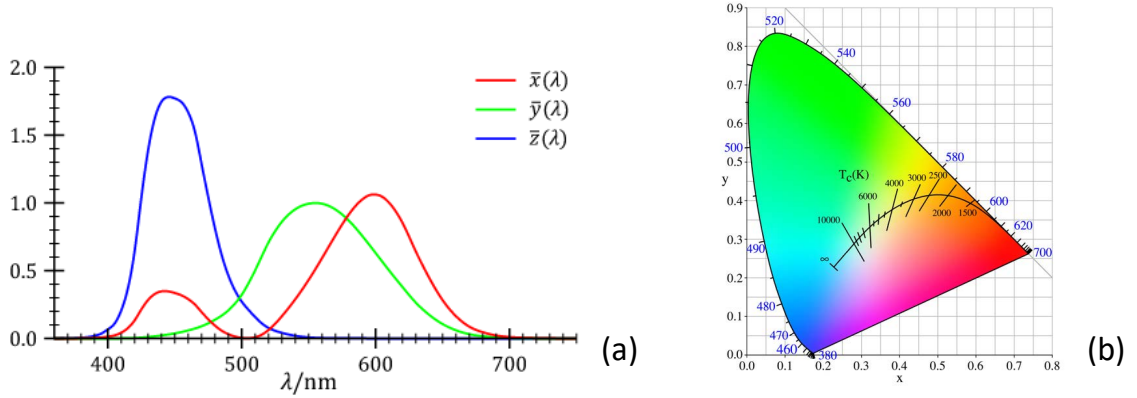


Figure 3.4: (a) CIE standard color matching functions. (b) The CIE 1931 color space chromaticity diagram.

The CIE Color space is a device independent, comprehensive representation of all the colors that the average human eye can detect. The color space maps physically produced colors to color sensations registered by the eye (tristimulus values).[92] For a given spectral power distribution $S(\lambda)$, the tristimulus values can be given in terms of the color matching functions according to the following equations[91]

$$X = \int \bar{x}(\lambda)S(\lambda)d\lambda \quad (3.1)$$

$$Y = \int \bar{y}(\lambda)S(\lambda)d\lambda \quad (3.2)$$

$$Z = \int \bar{z}(\lambda)S(\lambda)d\lambda \quad (3.3)$$

aided in defining links between wavelengths in the electromagnetic visible spectrum and the colors perceived by the human eye.[92] The commission created the CIE 1931 RGB color space based on the experiments conducted by Wright and Guild.[92, 94, 91, 93]

The coordinates on the chromaticity diagram are then given as functions of all three tristimulus values by the following equations

$$x = \frac{X}{X + Y + Z} \quad (3.4)$$

$$y = \frac{Y}{X + Y + Z} \quad (3.5)$$

$$z = \frac{Z}{X + Y + Z} \quad (3.6)$$

Using this same technique but replacing the color matching functions with the specific transmission data of the red, green and blue filters for the detection camera in the optical microscope (Olympus IX70), that collectively produce a colored image, a new chromaticity plot was calibrated (Figure 3.5).

Figure 3.6 shows the color space measurements conducted on the same nanowire using the calibrated color space. The emission wavelengths from spots 1-3 are shown. For ternary compounds like $\text{CdS}_x\text{Se}_{1-x}$, changes in the composition translate to changes in the band-gap and hence in the detected emission wavelength.[95] Figure 3.7 shows the normalized PL spectra for nanobelts with compositions ranging from pure CdS to pure CdSe and the combinations in between. Assuming a single emission band at energies close to the band edge, the detected change in emission corresponds to a change in composition along the wire that is less than 3%. The average composition was found to be $\text{CdS}_{0.2}\text{Se}_{0.8}$. There is no indication that such subtle changes in composition result in noticeable changes of the extinction coefficient for light with energies far above the band gap. Halsted et al. found negligible energy changes for transitions between 4 and 6 eV for compositions that ranged from 60% to 100%.[96]

With the exclusion of a variation in initial carrier density due to changes in either the excitation fluence or the extinction coefficient, the variation in the temporal ASE dynamics at spots 1, 2 and 3 must be as a result of differences in the non-radiative recombination rates. In particular, differences in the Shockley-Read-Hall

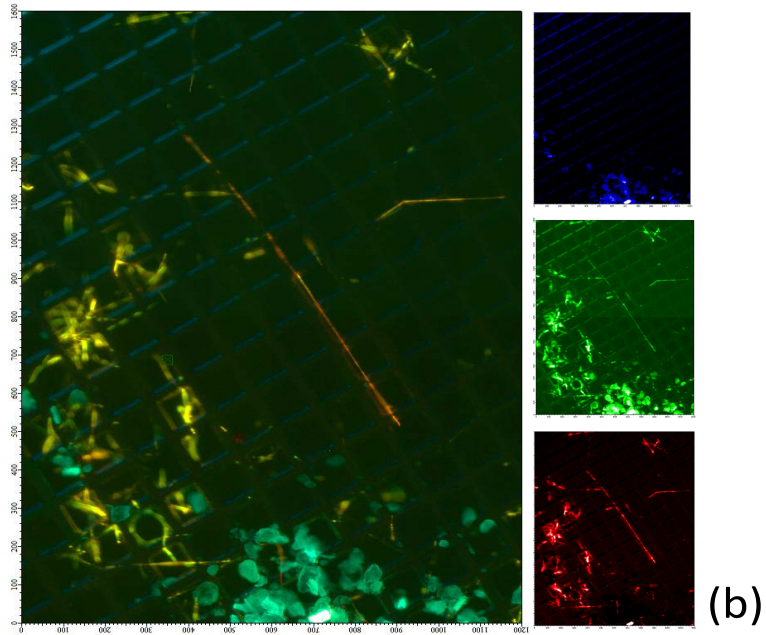
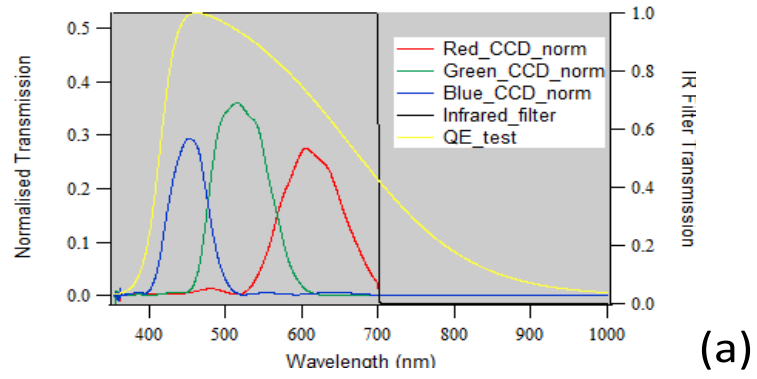


Figure 3.5: (a) Color matching functions for red, green and blue filters of the optical microscope. (b) Color image a $\text{CdS}_x\text{Se}_{1-x}$ nanowire and the pure color filter images that are combined to produce it.

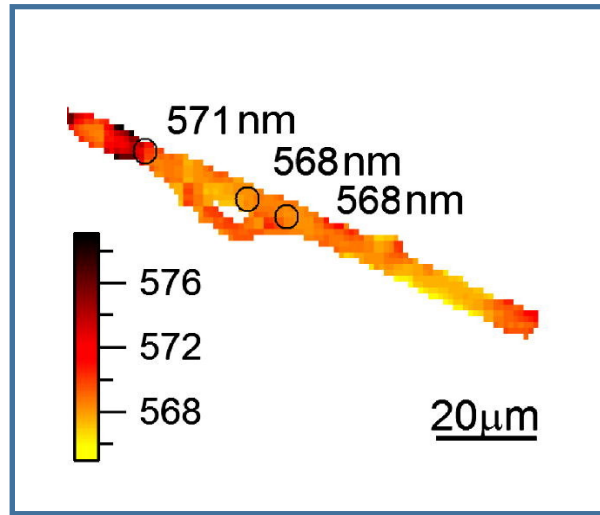


Figure 3.6: Spatially resolved color space analysis of the single $\text{CdS}_x\text{Se}_{1-x}$ nanobelt. Reprinted with permission from Elsevier.[89]

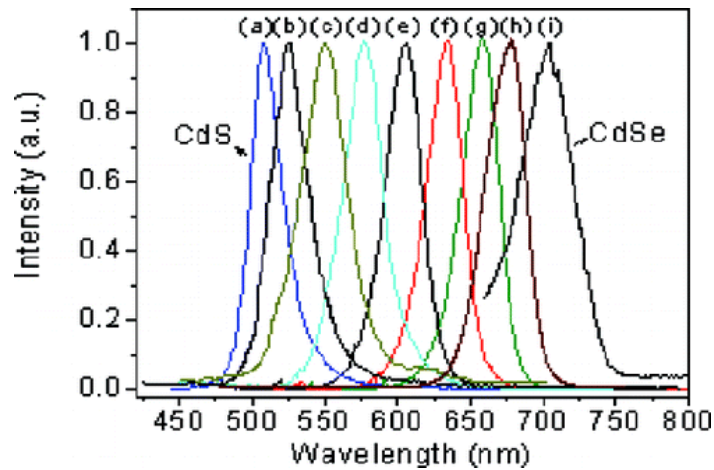


Figure 3.7: The normalized PL spectra for CdS, CdSe and $\text{CdS}_x\text{Se}_{1-x}$ nanobelts. Curves (a) and (i) are the PL spectra for CdS and CdSe respectively and curves (b)-(h) are the PL spectra for varying compositions of $\text{CdS}_x\text{Se}_{1-x}$ nanobelts. Reprinted with permission from Journal of American Chemical Society.[95]

recombination rate which is the apparent leading term. The Shockley-Read-Hall rate as well as the other non-radiative recombination rates can be extracted from the intensity dependent fits shown in Figure 3.3. From the Shockley-Read rate the charge carrier mobility can be calculated as detailed in section 1.1. To conduct a quantitative analysis through the global fitting routine requires very stable experimental conditions and emission transients with high signal-to-noise ratio. This was not possible with this preliminary data but carried out for another nanowire as discussed in section 3.3. It can be concluded, however, that there was a qualitative difference in the luminescence dynamics at all three spots and that ASE is a sensitive probe of local changes in Shockley-Read-Hall scattering rates. Additionally, such measurements could provide insight into the origin of spatial modulation of the defect density.

3.3 Extracting non-radiative recombination rates in a single $\text{CdS}_x\text{Se}_{1-x}$ nanowire

3.3.1 Introduction

Ternary alloys are known to have a higher defect density compared to their binary counterparts. A higher concentration of impurities has led to reports on increased non-radiative recombination centers due to Shockley-Read-Hall recombination in $\text{Al}_x\text{Ga}_{1-x}\text{As}$ as well as band-gap variations along $\text{CdS}_x\text{Se}_{1-x}$ nanobelts due to exciton localization.[97, 98] Ultrafast measurements on the single nanowire scale are therefore imperative to understand how variations in defect density, morphology or composition translate to changes in the recombination dynamics and in the observed ultrafast luminescence. Extrapolating on the preliminary measurements presented in section 3.2.1, the early luminescence dynamics in a single $\text{CdS}_x\text{Se}_{1-x}$ nanowire was investigated. The single nanowire was excited at different fluences and the luminescence was detected with the Kerr-gated ultrafast microscope. The non-linear, short-lived emission was ascribed to ASE and the emission transients fit to the ASE model. The fits to the ASE model allow the non-radiative carrier lifetimes and the non-geminate recombination to be extracted. The extraction of the non-geminate recombination coefficient and

the subsequent calculation of the carrier mobility, demonstrates the capability of the ultrafast Kerr-gated technique to probe carrier dynamics on short enough timescales and high enough carrier densities, that a non-diffusion limited recombination regime can be accessed for low carrier mobility nanowires.

3.3.2 Materials and Methods

The $\text{CdS}_x\text{Se}_{1-x}$ nanowires used for these measurements were grown via the same VLS method outlined in section 3.1.1. This technique is known to produce single crystalline nanowires with wurtzite phase. Nanowires were drop-cast onto TEM grids and the samples evacuated in a vacuum cryostat. Initial characterization of the nanowires involved fluorescence microscopy with an Olympus IX70 while SEM imaging was conducted after ultrafast measurements using a Hitachi S4700.

Figure 3.8 shows multiple images of the nanowire selected for this investigation. Figure 3.8 (a) shows a true color fluorescence micrograph of the nanowire. Color space analysis was also employed to map the emission wavelengths along the length of the nanowire and hence identify any composition variations that may occurred during growth (Figure 3.8(b)). Assuming the dominant emission is as a result of band edge emission,[98] then the average emission wavelength along the nanowire was $\sim 563\text{nm}$. There was a less than 5% variation in emission wavelength occurring along the length of the nanowire. This average emission wavelength corresponds to a composition formula $\text{CdS}_{0.8}\text{Se}_{0.2}$, when the compositional dependence found in Pan et al. is utilized.[95] The SEM images (Figure 3.8 (c) and (d)) shows the nanowire to be free of loose debris and the magnified image reveals the surface to be smooth with no significant morphological changes. The nanowire was approximately 200 nm thick and 500 nm wide and 200 μm in length. Figure 3.8(e) shows the EDS spectra obtained for the nanowire ensemble sample. The composition calculated from the EDS spectra was found to be $\text{CdS}_{0.64}\text{Se}_{0.36}$. This is in agreement with the color space analysis as variations in composition across the bulk sample is expected.

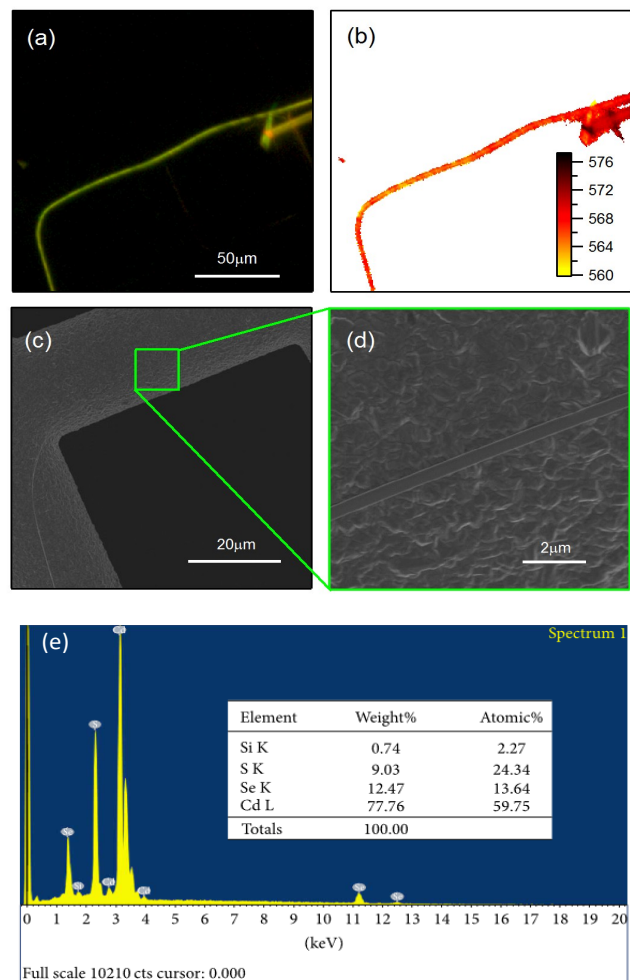


Figure 3.8: (a) A fluorescence micrograph of the studied CdSSe nanowire on a TEM grid. (b) The results of a color space analysis of the micrograph displaying the extracted emission wavelength in nanometers. (c) and (d) SEM images of the same nanowire. (e) EDS measurement for the bulk sample.[99]

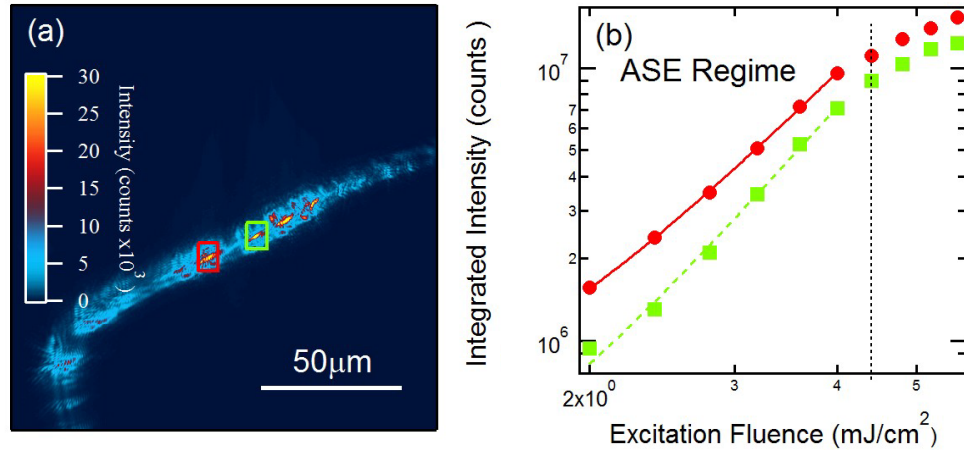


Figure 3.9: a) A time-integrated open gate image displaying the luminescence along the nanowire in a false-color scale. (b) The integrated intensity at two different locations along the wire as a function of excitation fluence on a log-log plot.[99]

3.3.3 Results and discussion

Figure 3.9 (a) shows the steady-state, false-color luminescence image of the same nanowire excited at a fluence of $3.5 \text{ mJ}/\text{cm}^2$. Several regions of high intensity emission were observed along the length of the nanowire. Two of these regions of high intensity, the red and green box indicated on the micrograph, were selected. The integrated intensity for these two selected positions were plotted in Figure 3.9 (b) on a log-log plot for a fluence ranging from 2 - $6.5 \text{ mJ}/\text{cm}^2$. At fluences below $4.4 \text{ mJ}/\text{cm}^2$, marked by the dotted line, the emission intensity shows a non-linear increase with increase in excitation fluence. A power-law fit to this non-linear increase shows a near cubic growth in luminescence intensity with power. This growth is higher than previous reports for free electron and hole or exciton recombination in CdSe nanowires.[100] From the data in reference [101], the absorption coefficient for $\text{CdS}_{0.8}\text{Se}_{0.2}$ at 290 nm was estimated to be $2 \times 10^4 \text{ cm}^{-1}$. The carrier densities generated in the nanowire were therefore estimated to range from $5 - 10 \times 10^{19} \text{ cm}^{-3}$ which is higher than the Mott

Table 3.1: ASE Model Fitting Parameters

Fit Parameters	Location 1
Relaxation rate γ_r (s^{-1})	2.5×10^{11}
Escape rate γ_Φ (s^{-1})	1.3×10^{13}
Shockley-Read-Hall γ_s (s^{-1})	2.0×10^{-10}
Nongeminate rate constant γ_g ($cm^3 s^{-1}$)	3.0×10^{-7}
Auger rate constant ($cm^6 s^{-1}$)	3.55×10^{-26}

density of both CdS and CdSe.[102, 103] Above 4.4 mJ/cm², there was a reduction in non-linearity in the emission intensity indicated by the change in the slope. The apparent plateauing of the emission intensity is either the result of carrier heating or Auger recombination. Since the focus of the investigation is on ASE dynamics, the discussion will be limited to resolving the temporal emission for fluences <4.5 mJ/cm², the ASE regime.

In transient mode, closed gate configuration, luminescence images of the nanowire were recorded at different pump-probe delays and excitation intensities. For the region of high intensity marked by the green box (Location 1), in Figure 3.8 (a), the emission was integrated for each image and plotted as a function of time. Figure 3.9 is a plot of the recorded transients at two excitation fluences, 2.2 mJ/cm² and 4.4 mJ/cm². At 2.2 mJ/cm², the emission is broad and the peak intensity occurs at approximately 3.5 ps. Increasing the fluence to 4.4 mJ/cm², the onset of emission shifts to earlier times and the emission intensity increases. Two peaks are also observed, the higher of which occurs at 2 ps and the second at a later delay time around 2.5 ps.

The solid lines represent the fitting of the data to the ASE model, described previously (section 3.2.1). For the global fitting routine the only parameter that was changed was the carrier density which is given by the increase in the excitation fluence. The measured transient data fit reasonably well to the ASE model and was able to fit both the shift in the onset of emission as well as the second peak observed at the higher fluence in Figure 3.10. The fitting parameters are shown in Table 3.1. The extracted Shockley-Read-Hall lifetime, which is a measure of the impurity mediated non-radiative

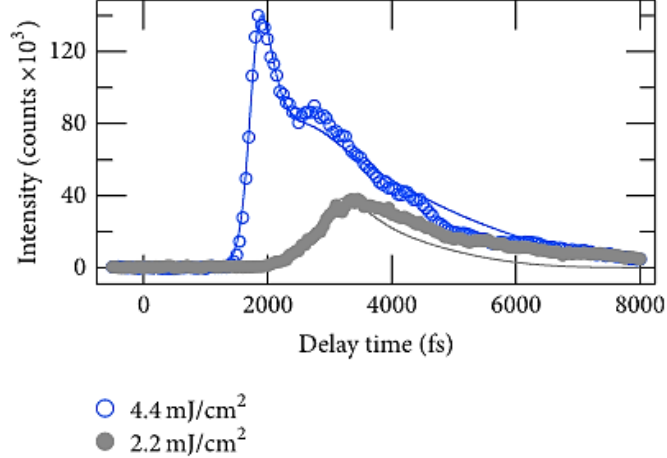


Figure 3.10: Measured luminescence transients from the single nanowire at two different excitation fluences (gray and blue markers) and the fits to the ASE model (solid) line at each fluence.[99]

lifetime,[104, 105] was ~ 200 ps. This value was comparable to the measured non-radiative recombination lifetimes reported for $\text{CdS}_x\text{Se}_{1-x}$ nanobelts.[106] Although the Shockley-Read-Hall term was expected to dominate as was reported previously,[59] for the fit of this data, the non-geminate recombination rate constant was found to be the leading damping term as the extracted value was $3.0 \times 10^{-7} \text{ cm}^3\text{s}^{-1}$.

According to reference [63], depending on the mobility of the material, two different regimes exist for non-geminate recombination either the diffusion controlled or non-diffusion controlled, as discussed in section 1.1. Assuming the diffusion limited condition applies to the undoped $\text{CdS}_x\text{Se}_{1-x}$ nanowire in this study, then the non-geminate rate can be given by

$$\gamma_g = e\mu_L/\epsilon \quad (3.7)$$

The calculated Langevin mobility was $0.2 \text{ cm}^2/\text{Vs}$. This value is comparable to the electron mobility recorded from field-effect-transistor (FET) measurements on pure CdS nanowires ($1.7 \text{ cm}^2/\text{Vs}$)[107] but is several orders of magnitude lower than the

more recent time-resolved terahertz measurements ($81.6 \text{ cm}^2/\text{Vs}$).[106]

Although large mobilities in these nanowires were not expected, there is a possibility that at these high carrier densities the carriers recombine before they undergo significant phonon, impurity or defect scattering. The criteria for being in the diffusion limited regime was most likely not satisfied. Using a scattering time of 100 fs, [108] it can be confirmed by a rough approximation, that at the high carrier densities generated in these measurements $v_T\tau_s$ is approximately equal to $(N_r)^{-1/3}$ only when the carrier temperature is on the order of 10 K. Therefore on these ultrafast timescales and high carrier densities achievable with the Kerr-gated microscope, the non-diffusion controlled regime, typically inaccessible by other techniques that operate at lower densities and longer timescales, can be entered for low mobility material systems like $\text{CdS}_x\text{Se}_{1-x}$ nanowires.

3.3.4 Conclusions

Spatial variation in carrier dynamics along a single $\text{CdS}_x\text{Se}_{1-x}$ has been observed with ultrafast luminescence measurements. This type of excitation fluence dependent, non-linear dynamics has been identified as amplified spontaneous emission (ASE) in previous work. It was demonstrated that it is possible to observe differences in ASE dynamics measured under identical conditions at different spots on a single nanowire. These variations are a result of differences in the recombination rates. The changes in recombination rates can be determined by fitting to the ASE rate model. It was found that transient data with high signal-to-noise ratio was required to achieve an adequate fit to the ASE model. Through globally fitting the emission data of a nanowire with increased signal-to-noise ratio to the ASE model, the position dependent non-radiative recombination rates and the non-geminate recombination rates at each location can be extracted. From the measurement of the non-geminate recombination rate it can be concluded that the majority of the excited carriers recombine before significant impurity, phonon, or defect scattering. Therefore, carrier recombination is not diffusion controlled at high densities even in low mobility materials.

Chapter 4

ZINC OXIDE SEMICONDUCTOR MATERIAL

This chapter takes a detailed look at one of the metal oxides, ZnO, that is at the center of this study. A formal presentation of the physical properties and synthetic methods of ZnO is necessary before a discussion of the ultrafast measurement of single nanostructures is given. This ensures a fluent explanation of the observed ultrafast phenomenon. This chapter will therefore present ZnO as a semiconductor material, its applications, fundamental properties and the common synthetic methods for nanostructures of ZnO. The synthetic pathways that lead to specific morphologies are also explored as part of an extension of this study.

4.1 Historical Timeline

Investigations on ZnO are reported to have begun as early as 1912, with systematic studies into ZnO as a semiconductor occurring in the 1930s- 1940s, the semiconductor age, around the time of the invention of the transistor.[109, 110] Research momentum picked up in the decades to follow and peaked around the 1970s, where the first electronic application of ZnO in acoustic wave devices [111] came in 1976 following the discovery of the piezoelectric properties of ZnO in 1960.[112, 113] Interest in ZnO work faded in the early 1980s. The decline was attributed to two major factors, the first of which was the inability to dope ZnO in both an n- type and p-type. Secondly, the direction of interest switched to structures with increasingly smaller dimensionality, such as quantum wells, that were based solely on III-V systems.[110, 114, 115] Research on diminutive structures of ZnO would not start until almost a decade later

in the 1990s where there was a resurgence in scholarly work on the semiconductor material. Prior to this, most research was conducted on bulk crystal samples and covered areas such as growth, deep centers, luminescence and lasing to name a few.[116]

The current revival of ZnO research has been spurred on by the pursuit of reproducible and stable p-type doping in ZnO. It has proven difficult to obtain p-type doping [117, 118] because ZnO has the proclivity towards n-type conductivity.[119, 120] A detailed discussion on p-type doping will not be undertaken in this work, instead the past and present activities toward doping in ZnO can be found elsewhere.[120, 121, 122, 123]

4.2 Fundamental properties and applications

Despite the slow progress towards p-type doping, there has not been a shortage of applications for ZnO. The list of favorable properties of ZnO has made it an ideal candidate for incorporation into various devices. Table 4.1 summarizes some of these properties discussed below.

Direct bandgap. Zinc oxide is a member of the II-VI class of compound semiconductors. The direct band gap, 3.37 eV at room temperature and 3.44 eV at low temperatures [124], is one the most attractive properties of ZnO. The wide bandgap has made it suitable for optoelectronic applications in the blue/UV region of the spectrum such as laser diodes [119, 120] and photodetectors. [125, 126, 127].

Strong luminescence. The photoluminescence spectrum of ZnO typically shows three distinct bands, a peak at 386 nm, a weak blue peak 440-480 nm and broad peak 510-580 nm.[128] The peak in the green region of the spectrum, attributed to intrinsic defects, exhibits strong luminescence which can be used for phosphor applications such as thin-film electroluminescence displays. [119, 109, 129]

Large exciton binding energy. ZnO has a large exciton binding energy of 60 meV. [130] This property makes ZnO suitable for optoelectronic applications based on excitonic effects since it exhibits efficient excitonic emission at room temperature and higher.[119]

Table 4.1: Properties of wurtzite ZnO. Reprinted with permission from Elsevier. [130]

Property	Value
a_0	0.32495 nm
c_0	0.52069
a_0/c_0	1.602 (ideal hexagonal structure shows 1.633)
u	0.345
Density	5.606 g/cm ³
Stable phase at 300 K	Wurtzite
Melting point	1975 °C
Thermal conductivity	0.6, 11.2
Linear expansion coefficient(/C)	a_0 : 6.5 10 ⁶ C_0 : 3.0 10 ⁶
Static dielectric constant	8.656
Refractive index	2.008, 2.029
Energy gap	3.4 eV, direct
Intrinsic carrier concentration	<10 ⁶ cm ³ (max n-type doping > 10 ²⁰ cm ³ electrons; max p-type doping <10 ¹⁷ cm ³ holes
Exciton binding energy	60 meV
Electron effective mass	0.24
Electron Hall mobility at 300 K for low n-type conductivity	200 cm ² /V s
Hole effective mass	0.59
Hole Hall mobility at 300 K for low p-type conductivity	550 cm ² /V s

Piezoelectric properties. ZnO has large piezoelectric constants due to the low symmetry of the wurtzite crystal structure discussed in detail in section 4.2.1 . It has been utilized in surface-acoustic wave devices and piezoelectric sensors.[119, 109]

Strong surface sensitivity. Although the mechanism is not fully understood,[131] the conductivity of the surface of thin films of ZnO are sensitive to surrounding gas atmosphere. ZnO therefore can be used as a sensor for food freshness, poisonous hazardous chemicals, soil and water pollutants and gas alarms.

Other applications that rely on the above properties include solar cells,[132] field effect transistors (FET),[133] transparent electronics,[134] photocatalysts[135] and ohmic contacts.[136]

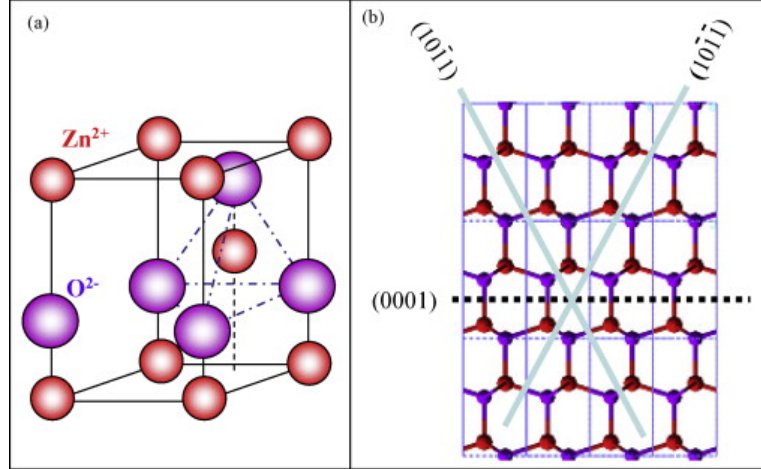


Figure 4.1: (a) Model of the wurtzite structure of ZnO, showing the tetrahedral coordination of Zn-O . (b) The three crystal facets of ZnO nanostructures (0001) $\{2\bar{1}\bar{1}0\}$, $\{01\bar{1}0\}$. Reprinted with permission from Elsevier. [137]

4.2.1 Crystal structure

The II-VI group of binary compound semiconductors can crystallize in either cubic zinc-blende or hexagonal wurtzite structure.[120] ZnO preferentially crystallizes in hexagonal wurtzite structure, shown in Figure 4.1 (a), under standard conditions and has lattice parameters $a = 0.32495$ nm and $c = 0.52069$ nm and hexagonal space group $P6_3mc$. [137] The cubic zincblende structure is metastable and can be stabilized by heteroepitaxial growth on certain cubic substrates such ZnS[138] and GaAs/ZnS [139]. The rocksalt structure, however, can be obtained from wurtzite ZnO only under external hydrostatic pressure and not by epitaxial growth.[116, 140, 120]

The tetrahedral coordination of the Zn^{2+} and O^{2-} ions creates a non-central symmetric structure that leads to the excellent piezoelectric and pyroelectric properties discussed above (section 4.2).[109, 141] The ZnO structure consists of alternating planes of tetrahedrally coordinated Zn^{2+} and O^{2-} ions stacked along the c -axis. The polar faces of the ZnO crystal are another important feature. Although the hexagonal unit cell is neutral the cations and anions are spatially distributed in such a manner as to cause some surfaces to be terminated solely by either cations or anions.[137] The

polar surfaces in ZnO include $\pm(0001)$ and $\{01\bar{1}1\}$ type surfaces. The basal plane is the most common charged surface. The positively charged (0001) and negatively charged $(000\bar{1})$ surfaces set up a dipole and spontaneous polarization along the c-axis. Convention states that the $[0001]$ axis points in the direction of the O-plane to the Zn-plane and is the z-positive direction and referred to as Zn polarity.[120] The ionic nature of the charges on the polar surfaces makes them immobile and non-transferable so the interactions rely on the distribution of these charges. The crystal formation and growth are therefore dictated by configurations that minimize the electrostatic energy.[141]

The growth tendency towards minimizing the energy of the surfaces means that lower energy facets such as the nonpolar $\{2\bar{1}\bar{1}0\}$ and $\{01\bar{1}0\}$ surfaces are maximized as shown in figure 4.2. Similarly, $\langle 2\bar{1}\bar{1}0 \rangle$, $\langle 01\bar{1}0 \rangle$ and $\pm[0001]$ are the three types of fast growth directions in ZnO, whose growth rates can be controlled during synthesis. Other than the energy of surfaces, the relative surface activities, determined by the kinetics specific to each crystal plane, also determines the morphology and can be finely tuned by growth parameters.[141] The combination of polar and nonpolar surfaces with tunable growth rates allows ZnO nanostructures to be deliberately synthesized.

4.3 Synthesis and growth

The multitude of synthetic pathways for ZnO contributes to its appeal as a semiconductor material. The versatility of ZnO stems from the variety of different morphologies it can assume and how the subtle adjustment of growth parameters can affect the optical properties. Because this study focuses on nanostructures of ZnO, only synthetic methods specific to synthesis of single crystalline nanostructures will be specifically addressed. Methods such as molecular beam epitaxy (MBE),[142] rf magnetron sputtering,[143] metal organic chemical vapor deposition (MOCVD)[144] and pulsed laser deposition (PLD),[145] although heavily utilized in synthesis of ordered arrays, will not be addressed in detail as none of these methods were explored for the synthesis of the nanostructures in this study. The ZnO nanostructures investigated

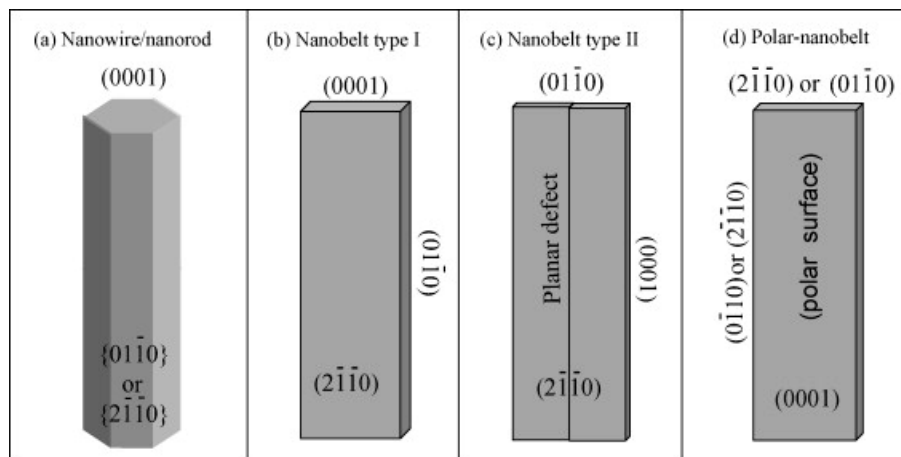


Figure 4.2: The common growth morphologies of one-dimensional ZnO nanostructures and the corresponding facets. Reprint permission granted by Elsevier. [137]

in this study were synthesized by two main synthetic routes, vapor phase deposition via the vapor-liquid-solid (VLS) method, as was detailed in section 3.1.1, and solution based growth. The solution based growth methods can be further grouped into either high or low temperature procedures. Regardless of the specific synthetic route each method was uniquely sensitive to changes in the experimental parameters such as temperature, carrier gas flow rate and precursor preparation. The adjustment of these parameters, which allowed for manipulation of the growth morphology of single ZnO nanowires, is explored with particular focus on growth via the solution based methods.

4.3.1 Vapor Phase Synthesis of ZnO

The two most important vapor phase techniques for growth of ZnO nanostructures are the VLS and MOCVD methods.[146, 144] The VLS method has been more intensely investigated because of the lower cost and ease of the technique.[87] As outlined previously, VLS synthetic methods are conducted in a horizontal tube furnace at high temperatures. Similar to the synthesis of $\text{CdS}_x\text{Se}_{1-x}$ nanomaterial, the reactant source powders in an alumina boat, are placed at the center of the furnace at the appropriate growth temperature while the substrates are placed downstream at a lower temperature or on top of the precursor boat. A gas stream is provided to the system and for certain setups vacuum pressure, usually around $\approx 2 \times 10^{-3}$ Torr.[141]

The synthesis of ZnO via vapor phase through a carbo-thermal reduction method is one the most popular synthetic routes.[147, 148, 149] The ZnO nanowires measured in chapter 5 and chapter 6 were synthesized by a VLS carbo-thermal method according to the following method.[147, 150] ZnO nanopowder and active carbon were combined in equal parts in ethanol and sonicated for 30 minutes. The mixture was then dried in an oven at 80 °C. The dried mixture was transferred to an alumina boat. Cleaned sapphire wafers were used as the growth substrate. A 10 mm thick layer of Au catalyst was sputtered onto the sapphire wafers before placing them with the gold face down on top of the alumina boat containing the precursor. The boat-wafer assembly was placed in a horizontal tube furnace and the tube purged for an hour with Ar gas at

a flow rate of 40 sccm at room temperature. The temperature ramp was then set to 900 °C at 80 °C per minute while the Ar flow was kept constant. The dwell time at 900 °C was set at 2 hours before the tube was opened to atmospheric oxygen. The reaction was allowed to continue for another 3 hours at 900 °C, before naturally cooling to room temperature.[151] The method produced nanostructures that follow a three-stage growth model and both VLS and VS mechanisms. The resulting morphology was that of hexagonal rods and belts. Details of the growth morphology as a result of the selected growth parameters are outlined in section 6.2.4.

As in most synthetic procedures of nanostructures the resultant product quality and morphology is dependent on the processing parameters. For vapor phase techniques these include temperature, pressure, the type of carrier gas and the flow rate, substrate, growth time, type of catalyst, system geometry and starting material. The temperature range used in a vapor phase process depends on both the source material as well the location of the growth substrate.

Different starting materials can be used as the source for ZnO nanostructures in vapor phase methods. The most common materials are pure zinc metal or a mixture of ZnO and carbon powder.[152] For pure Zn, typical source temperatures are approximately 500 °C and 800-1100 °C for ZnO-carbon mixtures.[153, 147] The source temperature is usually selected based on the volatility of the source material and is usually chosen to be slightly lower than the melting point of the source.[141] For other methods that use zinc acetylacetonate hydrate, the source temperature is lower and can range from 130-140 °C.[154] The temperature of the substrate and hence the growth temperature of the nanostructures can range from 450-550 °C if the substrate is positioned downstream of the source materials or will be at the source material temperature if placed on top of the alumina boat.

Another important parameter is the nature of the growth substrate. For aligned arrays, the crystal structure of the substrate is critical for the orientation of nanowires. ZnO nano arrays have been successfully grown on sapphire, GaN, AlGaN and AlN substrates using the VLS process.[155] The epitaxial growth of ZnO nanowires on specific

single crystal substrates determines the growth orientation while the vertical alignment quality is controlled by many other parameters.[156] Sapphire and nitride substrates have been particularly successful at producing well aligned ZnO nanowires because of the small lattice mismatch between ZnO and the substrates. Nitride substrates such as GaN and AlGa_xN, have the same wurtzite structure as ZnO and so growth along the [0001] direction is adhered to very closely with epitaxial confinement in all the planes equivalent to (01 $\bar{1}$ 0).[156] The c-plane of Al_xGa_{1-x}N substrate is therefore ideal for growing well ordered ZnO nanowire arrays. For sapphire substrates, although the lattice mismatch along the c-axis of sapphire and the a-axis of ZnO is approximately zero, the (11 $\bar{2}$ 0) plane of sapphire is a rectangular lattice and so the epitaxial relationship is only true for one direction.

Although ZnO shows a strong dependence on the substrate crystal structure, well aligned, high aspect ratio ZnO nanowires have also been grown on Si(100) and Si(111) surfaces by fine tuning the growth parameters. [157, 158, 87] The VLS synthesis of ZnO is particularly sensitive to the oxygen concentration in the closed system. In particular, the oxygen partial pressure and the total system pressure can have a strong effect on nanowire growth. The oxygen concentration in the system can influence the volatility of the source material and the stoichiometry of the vapor phase. These changes in growth conditions ultimately affect the optical properties and intrinsic defects in the individual nanostructures.[141] A more in-depth discussion of growth conditions and defects will be undertaken in section 4.4 and chapter 6.

In VLS synthetic methods the metal catalysts employed also play an important role in the initial stages of the nanowire growth. Alongside the other parameters such as temperature and system pressure, the type of metal catalyst and thickness of the layer need to also be carefully considered. The typical metal catalysts used are Au, Cu, Ni and Sn.[87] Changing the metal catalyst has been shown to determine whether nanowires grow via VLS, VS, VSS or a combination of these mechanisms.[159]

The primary aim of VLS techniques are to produce ordered arrays of vertically

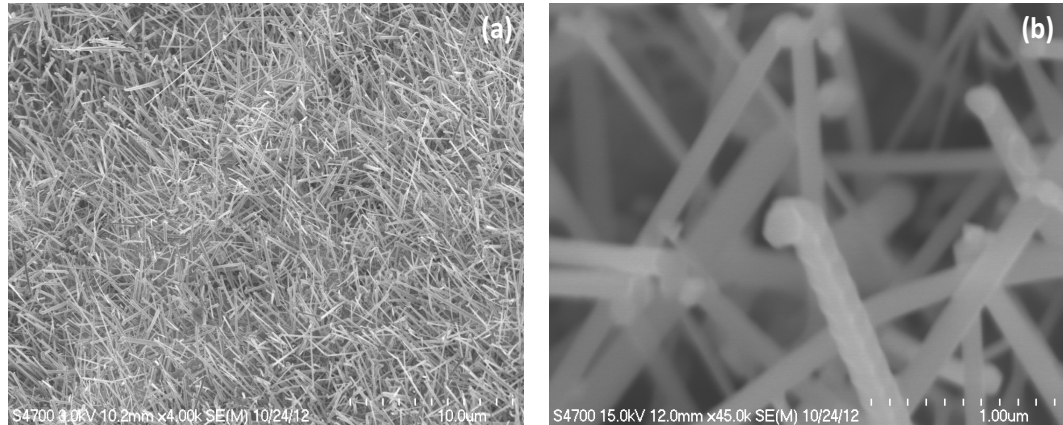


Figure 4.3: (a) SEM image of ZnO nanowire array grown via second VLS method. (b) Magnified image of a single ZnO nanowire showing the characteristic gold catalyst tip.

aligned nanowires, the collective set of growth conditions can, however, occasionally create an environment conducive to the horizontal alignment of nanowires on a substrate. Horizontally grown nanowires, like their vertical counterparts, have found applications in next generation devices.[160] They have the potential to replace the need of post-growth manipulation of delicate, vertically grown nanowires. The guided horizontal growth would make it easier for large scale integration of nanowires in circuits and planar devices.[161] Lateral growth of nanowires has been observed in numerous studies occasionally as an unexpected growth anomaly as well as in specific parameter controlled investigations.[162, 163] For studies that pursue deliberate growth of horizontal nanowires the focus is primarily on epitaxial relationships between the nanowire and the substrate. Joselevich et al. have suggested that there are three general modes of guided nanowire growth via VLS. There is epitaxial growth along lattice directions, graphoepitaxial growth along L-shaped nanosteps and graphoepitaxial growth in V-shaped nanogrooves.[160]

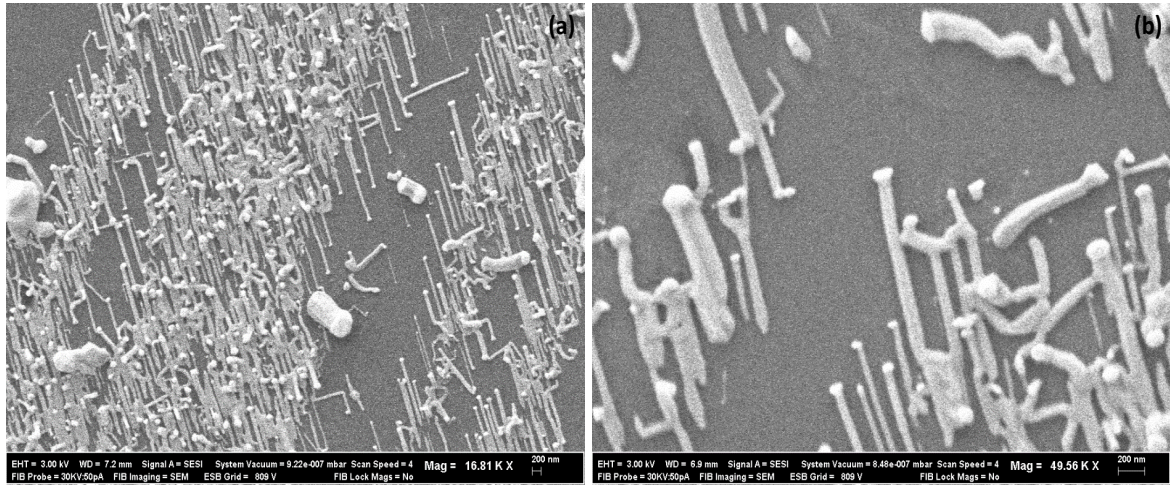


Figure 4.4: (a) and(b) SEM images of horizontally aligned ZnO nanowires grown via second VLS method.

The epitaxial horizontal growth is reported to be accompanied by the expected vertically aligned growth. Figure 4.3 shows ZnO nanowires grown via a different carbo-thermal method than described above. In this second method the 1:1 ZnO to carbon powder mixture was ground together thoroughly before transferring to an alumina boat. An a-plane sapphire wafer, sputtered with 3.0 nm gold, was placed on top of boat with the sputtered face down. The boat wafer assembly was then positioned in a small inner quartz tube before placing it at the center of a larger quartz tube in the tube furnace. The small inner quartz tube served to concentrate the reactant vapors within the vicinity of the substrate. The temperature was ramped to 900 °C at a rate of 42 °C/minute after a purge cycle at 150 °C. An Ar gas flow rate of 23 sccm was maintained throughout the purge and growth cycle. This method yielded very uniform nanowires approximately 200 nm in diameter and with the characteristic gold tip in one area as shown in Figure 4.3, as well as much smaller horizontally aligned nanowires approximately 10 nm in diameter in other regions (Figure 4.4).

The a-plane of sapphire has been preferentially used as the crystallographic

plane for growth of ZnO thin films and nanowires. Horizontal growth of ZnO nanowires has also been previously reported on a-plane sapphire substrates. In these investigations the growth direction of the nanowires were in two opposite directions, $\pm[1\bar{1}00]$. Nikoobakht et al. showed that the vertical mode of growth competed with horizontal growth.[162] The horizontal growth was also very sensitive to the size and spacing of the Au nanodroplet. Only with nanoparticles smaller than 20 nm were ZnO nanowires observed to grow horizontally. These Au nanoparticles also had to be placed 100-150 nm apart. In contrast to the VLS synthesis technique employed for this study, these reports used patterned gold catalyst on the surface of the sapphire wafer either by photolithography or gold etching using a polydimethylsiloxane (PDMS) stamp as a mask.

Figure 4.5 shows the Au nanodroplets formed when 6 nm of Au was sputtered onto the surface of a silicon wafer. The nanoparticles ranged in size from approximately 5 nm to 20 nm and the spacing between particles varied. The error in the deposition thickness is approximately ± 2 nm so the size of the Au nanodroplets formed from the deposition of 3 nm of Au, as was used in the second VLS method, would be comparable. The size of the nanoparticles would therefore be appropriate for the observation of horizontal nanowires on the whole substrate. As shown in Figure 4.3 and 4.4, there is a mixture of both growth modes. If only the size of the Au is considered, the high mobility of Au nanodroplets at elevated temperatures on Si surface can lead to agglomeration and the formation of larger nanoparticles.[164] The vertical ZnO nanowires were grown on the part of the substrate that was closer to the center of the furnace and hence at the higher temperature. The temperature gradient established in the tube furnace could lead to larger nanoparticles forming in one part of the substrate than another. The vertical nanowires were larger in diameter than the horizontally grown nanowires indicating a larger starting Au catalyst nanodroplet.

The cause of this type of horizontal growth is still not fully understood but it has been shown that this type of heteroepitaxial growth also depends on minimization of strain energy. It has also been observed, however, apart from the dependence of

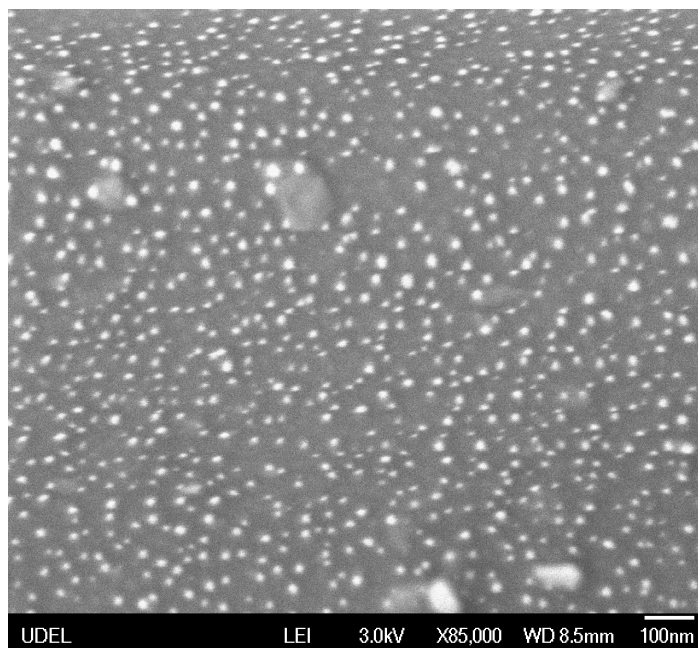


Figure 4.5: SEM image Au droplets formed from the deposition of 6 nm layer onto silicon wafer using vacuum sputtering system.

Au nanodroplet size, that epitaxial relationships of the nanowires and the substrates match that reported for thin films. This suggests thermodynamic influences in the control of the growth mode. Contrary to this, growth of nanowire facets that are not the lowest energy facets have also been observed. This suggests kinetic control at work in the determination of the growth mode.[161]

The growth simulation model proposed by Schwarz et al. proposes that in the initial stages of growth a droplet sits on top of a tapered pedestal where new facets are introduced to continue with steady-state nanowire growth. If the energetic effects of the facet edges become too large then the initial tapered base continues to taper rapidly and the catalyst droplet rolls off the top. Growth then continues from the base of this catalyst along the surface of the substrate. The set growth conditions would change the edge energies but little is known about how parameters such as temperature and partial pressure affect it.[165]

4.3.2 Solution based Synthesis of ZnO

Although high temperature vapor phase methods are known for producing more optical quality crystalline nanostructures, solution based methods can be performed at much lower temperatures and have more controllable parameters to manipulate. This particular feature of solution based methods can serve as either a hindrance or as an advantage. More parameters can be difficult to control when trying to reproduce a synthetic method while it can also provide more ways of adjusting growth conditions. Additionally, as the ultrafast measurements did not require vertically aligned nanowires, epitaxial growth was one less restriction in the high temperature solution based synthesis. The free growth of the nanostructures in solution meant less manipulation while preparing samples and decreased chance of damage to the nanostructures before measurement. The high temperature solution-based methods were therefore preferred over the low temperature methods. Solution based methods can be classified as either hydrothermal or solvothermal. Hydrothermal methods use water as a solvent while solvothermal methods use solvents.[127] The low temperature synthetic

trials were solely hydrothermal while the high temperature trials explored both types of methods.

High temperature methods. The high temperature method required the use of a 300-mL stainless steel autoclave with a teflon liner. The high pressure system allowed the aqueous reaction to be raised to temperatures above 100°C. The two procedures that were compared were, a hydrothermal method adapted from Zhang et al.[166] and a solvothermal-type method adapted from Fan et al. [167] Both methods were prepared without surfactants as an exploration of the limits of the tunability of the ZnO structures without additional reactants.

For the hydrothermal method the growth solution was prepared by combining 80 mL of 0.15- 0.5 M ZnCl₂ solution and 4 M NaOH solution and mixing rapidly for 20 minutes before transferring to the autoclave. Growth was conducted at 200 °C for varying growth times. The growth systems were either allowed to grow undisturbed or subjected to low speed stirring. The autoclave was allowed to cool to room temperature naturally. The samples were washed repeatedly with distilled water and then centrifuged and dried in a tube furnace for an hour before SEM or ultrafast measurements were conducted.

The chart shown in Figure 4.6 details the growth conditions and resulting morphology of the ZnO nanostructures. The general morphology was hexagonal nanorods of varying dimensions and shapes. Figure 4.7 (a)-(d) shows the effect of increasing the ZnCl₂ concentration while maintaining a constant NaOH concentration of 4 M. Increasing the ZnCl₂ concentration from 0.15 M to 0.2 M resulted in only subtle changes to the morphology. The tips of the rods became more defined and prismatic compared to rough, irregular shaped tips in the lower concentration solution. In the reaction solutions with concentrations above 0.2 M, nanoflowers consisting of multiple hexagonal nanorods were observed. The reaction solution with 0.5 M ZnCl₂ showed nanoflowers with nanorods densely packed around a core while the nanoflowers in the reaction solution with 0.3 M ZnCl₂ were an assorted mix of densely packed nanoflowers and

Temperature (°C)	Concentration (M)		Time (Hours)	Morphology	Notes
	NaOH	ZnCl ₂			
200	4	0.15	10	<ul style="list-style-type: none"> Hex rods with round and irregular pointed tips Different sizes 	
200	4	0.15	10	<ul style="list-style-type: none"> Hex rods with irregular pointed, pencil point tips Hex rods of uniform size 	mixing
200	4	0.2	10	<ul style="list-style-type: none"> Hex rods, round and pointed tips 	
200	4	0.2	10	<ul style="list-style-type: none"> Hex rods, round tips 	mixing
200	4	0.2	15	<ul style="list-style-type: none"> Hex rods, less sharp tips, indentation along growth length Short pieces 	
200	4	0.3	10	<ul style="list-style-type: none"> Hex rods with pointed tips Nano flowers of Hex rods with sharp and flat tips 	
200	4	0.3	15	<ul style="list-style-type: none"> Hex rods flat tip, indentation along growth length 	
200	4	0.3	20	<ul style="list-style-type: none"> Hex rods flat tip, indentation along growth length Broken pieces and conglomerates 	
200	4	0.3	20	<ul style="list-style-type: none"> Hex rods flat tips Nanoflowers of long rods, sharp tips 	mixing
200	4	0.3	30	<ul style="list-style-type: none"> Large Hex rods with flat tops Broken pieces and conglomerates 	
200	4	0.5	10	<ul style="list-style-type: none"> Nanoflowers of Hex rods with pointed tips 	
200	4	0.5	20	<ul style="list-style-type: none"> Nanoflowers of Hex rods, densely packed, less sharp tips Broken pieces 	
200	6	0.3	10	<ul style="list-style-type: none"> Amorphous conglomerates Pieces of Hex rods 	

Figure 4.6: Chart showing growth conditions and morphology for alkali method.

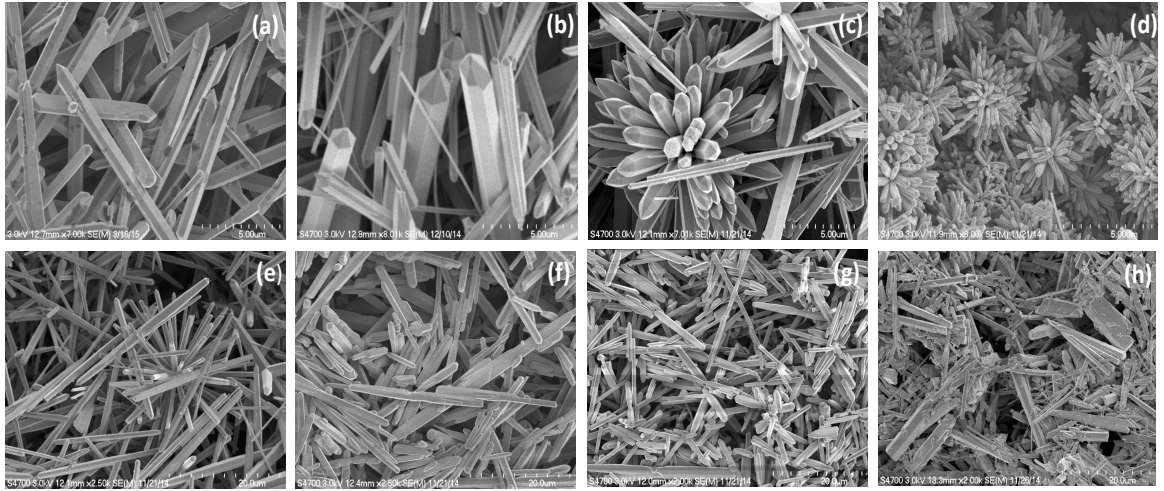
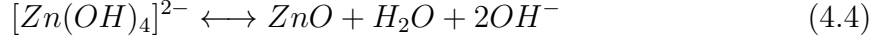


Figure 4.7: SEM images of ZnO nanostructures obtained with alkali hydrothermal method with ZnCl_2 concentrations (a) 0.15 M, (b) 0.2 M, (c) 0.3 M and (d) 0.5 M. ((e)-(h) SEM images of nanostructures grown with increasing growth times of 10 , 15, 20, 30 hours respectively for fixed ZnCl_2 concentration of 0.3 M and NaOH concentration of 4M.

nanoflowers with as few as 6 hexagonal nanorods per structure. At ZnCl_2 concentrations above 0.2 M there were also fewer single hexagonal nanorods with the 0.5 M ZnCl_2 solution consisting of only nanoflower structures. Increasing the growth time (Figure 4.7 (e)- (h)) from 10 hours to 30 hours resulted in a significant change in morphology. The nanostructures changed from well defined hexagonal nanorods and nanoflowers to larger hexagonal microrods with flat ends and fused conglomerates.

In the system described, the ratio of NaOH to ZnCl_2 establishes a strongly alkaline solution with the source of the Zn^{2+} being a $\text{Zn}(\text{OH})_4^{2-}$ complex. The formation of ZnO then follows the equations





The morphology control of ZnO in hydrothermal reactions is determined by two main factors the internal crystal structure and external conditions such as temperature, pressure and the presence of surfactants.[168] It has been reported that the starting solutions for hydrothermal growth can be more critical to crystal shape than the external conditions.[166, 169] The starting solutions determine the initial nucleation and different nuclei morphologies cause the different crystal shapes. The external conditions, however, mainly affect the continued growth.[170] Since $[\text{Zn}(\text{OH})_4]^{2-}$ acts as the building block of the ZnO nanostructures, the availability of $[\text{Zn}(\text{OH})_4]^{2-}$ in solution affects the nuclei size and crystal growth. The nuclei of ZnO result from the condensation of soluble $[\text{Zn}(\text{OH})_4]^{2-}$ clusters through a dehydration process detailed in equation 4.4. The high growth temperature (200 °C) can generate active growth sites around the circumference of the nuclei. Coupled with the fast incorporation of the $[\text{Zn}(\text{OH})_4]^{2-}$ growth units into these condensed clusters, growth can occur along the c-axis in multiple directions. Increasing the concentration of Zn^{2+} in solution increases the rate of condensation and subsequent precipitation, forming the nanoflower morphology observed in Figure 4.7 (c) and (d). From a kinetics stand point, the anisotropic crystal growth in ZnO is a result of the different growth rates at each of the crystal faces with $V(0001) \gg V(01\bar{1}0) > V(01\bar{1}1) > V(000\bar{1})$.[171] Figure 4.8 shows the location of each of these crystal planes in a idealized ZnO crystal hexagonal rod. From the given growth rates, it would seem possible to synthesize ZnO nanorods with high aspect ratios by just increasing the growth time. Figure 4.7 (e)- (h) shows that this is not the case and longer growth times lead to lower aspect ratios and larger clustered structures. The absence of a suitable surfactant is responsible for this. The growth time experiments

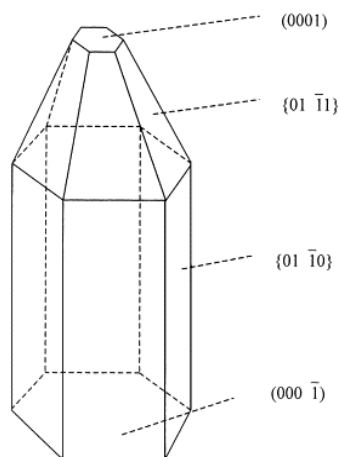


Figure 4.8: Idealized growth morphology of ZnO crystal. Reprint permission granted by Crystal Growth. [171]

highlight the growth limits of ZnO nanostructures with the hydrothermal method without surfactant. The surfactant would aid in sufficiently inhibiting lateral growth of the side walls facilitating higher aspect ratios without aggregation.[168]

Figure 4.9 shows the affect of stirring on two different starting concentrations of ZnCl_2 . The samples that were stirred, Figures 4.9 (b) and (d), both showed increased aspect ratios. The unstirred samples, Figures 4.9 (a) and (c), showed nanorods with indentations along the length. This feature was completely absent in the stirred samples. It is proposed that the indentations are a result of two nanorods growing head-on as shown in the inset of Figure 4.9 (a). The agitation caused by stirring the reaction mixture reduces the chances of nanorods remaining in the same growth position to grow head on.

In the solvothermal method, the starting solution consisted of 25 mL of 1 M NaOH and 1 M $\text{Zn}(\text{NO}_3)_2 \cdot 6 \text{H}_2\text{O}$ added and stirred for 10 minutes before 150 mL of ethanol was then added to the mixture to form a colloid. The colloid mixture was stirred for an additional 10 minutes before being transferred to a stainless steel

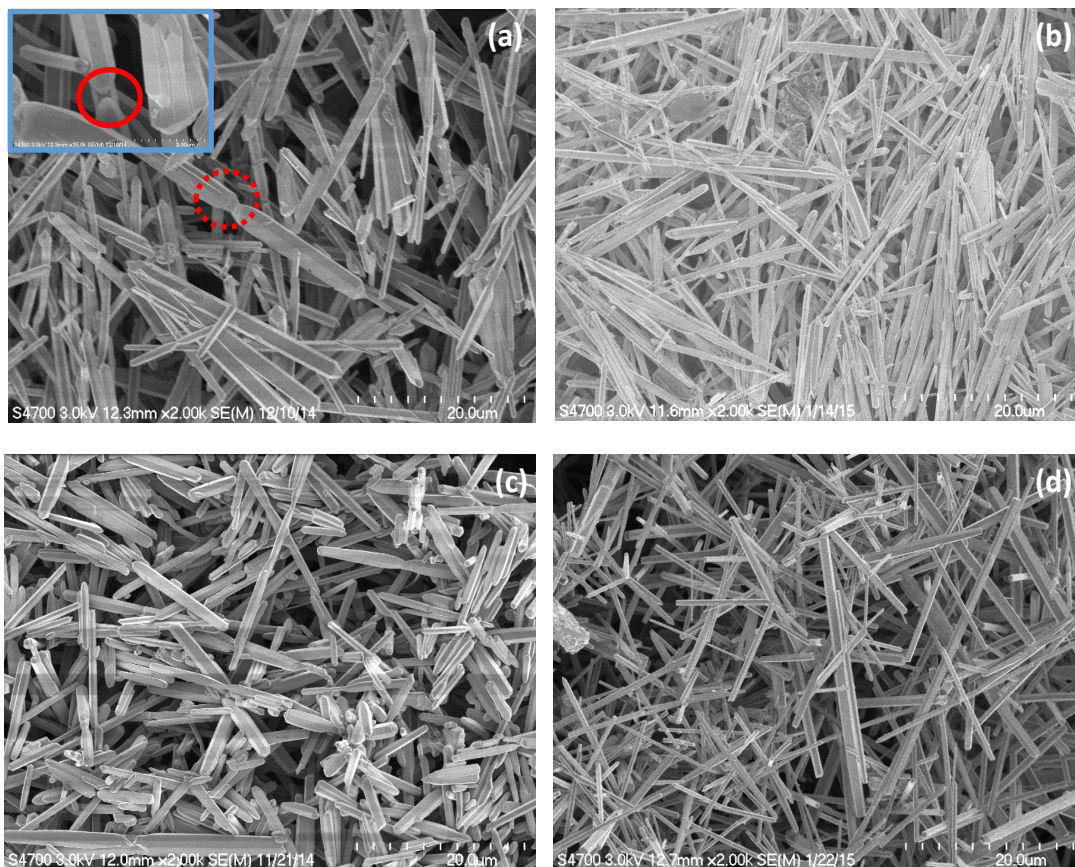


Figure 4.9: SEM images of ZnO nanostructures grown with starting reagents 4 M NaOH and .2 M ZnCl₂ (a) unstimulated (b) stimulated reactions. Inset shows the possible cause of the indentations observed. SEM images of ZnO nanostructures grown with starting reagents 4 M NaOH and .3 M ZnCl₂ (c) non-stimulated and (d) stimulated reactions.

autoclave where the growth process is carried out at temperatures ranging from 180-200 °C for varying growth times. The autoclave was allowed to cool naturally before the sample was removed. Similar to the alkali method the samples were washed with distilled water, centrifuged and dried before characterization. Table 4.10 shows the details of the different trials and the resulting morphologies. In general, the results of the colloid method showed mixed morphologies, regardless of the growth conditions as opposed to the alkali method that showed more homogeneous morphology distribution for each trial. Additionally, the overall size of the nanostructures were smaller in the colloid method than in the alkali method. Figure 4.11 shows the effect of increased growth time on morphology. At 10 hours the ZnO nanostructures were spindle shaped, small nanoflowers and even smaller hexagonal pieces that were the starting crystals of nanorods. Increasing the growth time to 15 hours, the morphology changed to slightly larger nanoflowers, and rods as well as amorphous clumps of ZnO material. Smaller hexagonal pieces were also still present. For a growth time of 20 hours, larger more defined nanoflowers were observed along with nanorods and large misshaped rods.

Figure 4.12 shows the effect of NaOH concentration and temperature on morphology. The increase in pH and temperature had a more dramatic effect on the morphology than growth time. When the NaOH concentration was increased from 1 M to 6 M the morphology changed to broad hexagonal rods. Decreasing the temperature from 200 °C to 180 °C changed the morphology from an assortment of nanoflowers and hexagonal pieces to dumbbells of varying sizes with holes through the center.

To understand the morphology changes in the colloid method it is useful to examine the reaction equations that govern the formation of ZnO shown above. In lower pH (less alkaline) and colloid solutions the source of Zn^{2+} is predominantly in the form $Zn(OH)_2$. Equation 4.3 shows that the reaction equilibrium would shift to the left in low pH conditions, decreasing the $[Zn(OH)_4]^{2-}$ growth units available in solution. With insufficient growth units the ZnO structures are unable to grow as large into the well defined hexagonal rods as in the alkali method. This dependence on chemical equilibrium is confirmed by the change in morphology shown in Figure 4.12

Temperature (°C)s	Concentration (M)		Time (Hours)	Morphology
	NaOH	Zn(NO ₃) ₂		
200	1	1	10	<ul style="list-style-type: none"> - Spindle rods - nanoflowers with flat tops
200	1	1	15	<ul style="list-style-type: none"> - Small Hex rods - nanoflowers with rods flat top (few) - Amorphous clumps
200	1	1	20	<ul style="list-style-type: none"> - Small nanoflowers with rods with flat tips - Small dumbbells
200	6	1	10	<ul style="list-style-type: none"> - Flat hex rods with sharp tip - Flat hex mini rods
180	1	1	20	<ul style="list-style-type: none"> - Dumbbells with holes - Spindles

Figure 4.10: Chart showing growth conditions and morphologies for the solvothermal method.

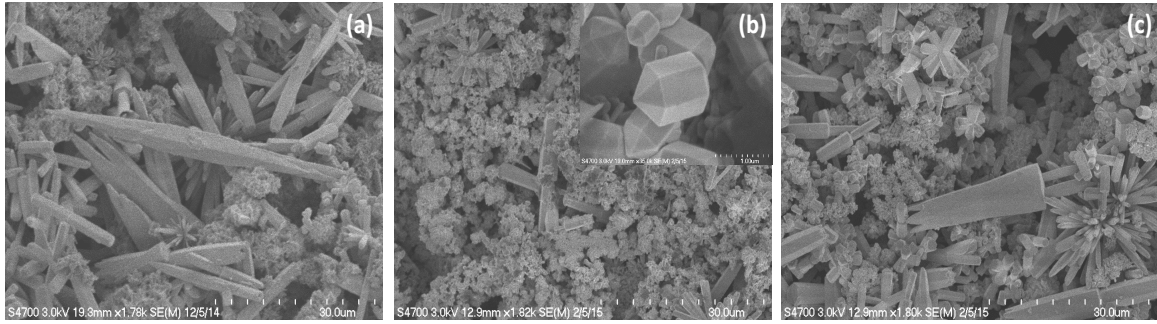


Figure 4.11: SEM images of ZnO nanostructures grown via the solvothermal-colloid method with 1 M NaOH and 1 M $\text{Zn}(\text{NO}_3)_2$ at (a) 10 hours, (b) 15 hours and (c) 20 hours.

(a) to (b) with the increase in NaOH concentration.

The effect of the decrease in temperature on the morphology involves both the initial nucleation phase as well as the continued growth parameters. At 180 °C the predominant morphology is that of dumbbell-shaped, twinned ZnO crystals. The growth mechanism and formation of dumbbell shaped ZnO nanostructures and microstructures has been discussed in numerous studies.[172, 173, 174] Each assigning different growth mechanisms. Most of these studies have assigned additives such as surfactants or different mineralizers as the cause of observed morphology. In the current hydrothermal method, as no surfactants were used, no surfactant-bonded species are involved in the growth mechanism hence the driving force must be the energetics associated with the individual crystal planes as well as the external growth conditions.

Decreasing the growth temperature would decrease the number of active growth sites around a newly formed ZnO nuclei and inhibit the formation of nanoflower-like structures that were observed at the 200 °C. Hence, no densely packed nanoflower structures are observed at 180 °C. The dominant dumbbell morphology at 180 °C is not uncommon as the arrangement of the polar crystal of ZnO makes twin formation favorable with either the positive or negative faces serving as the interface contact

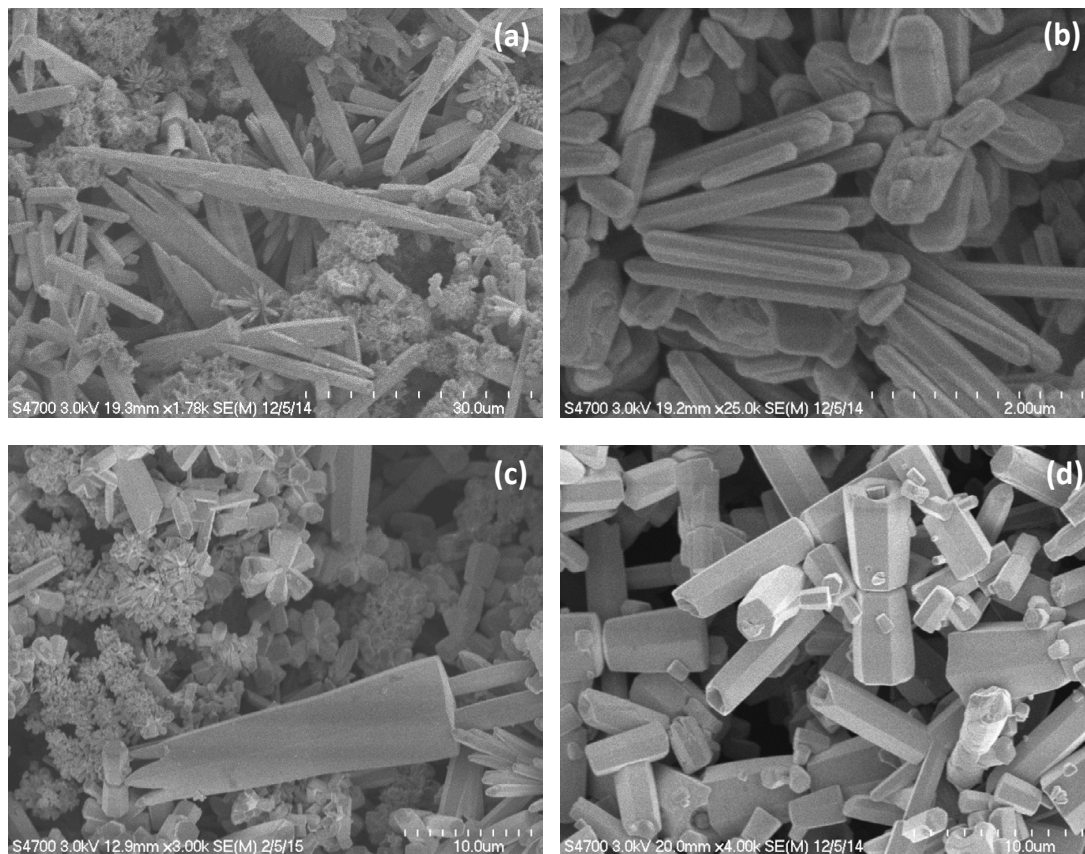


Figure 4.12: SEM images of ZnO nanostructures grown with 1 M $\text{Zn}(\text{NO}_3)_2 \cdot 6 \text{H}_2\text{O}$ and (a) 1 M NaOH and (b) 6 M NaOH. SEM images of ZnO nanostructures grown at (c) 200 °C and (d) 180 ° with a constant reactant concentrations.

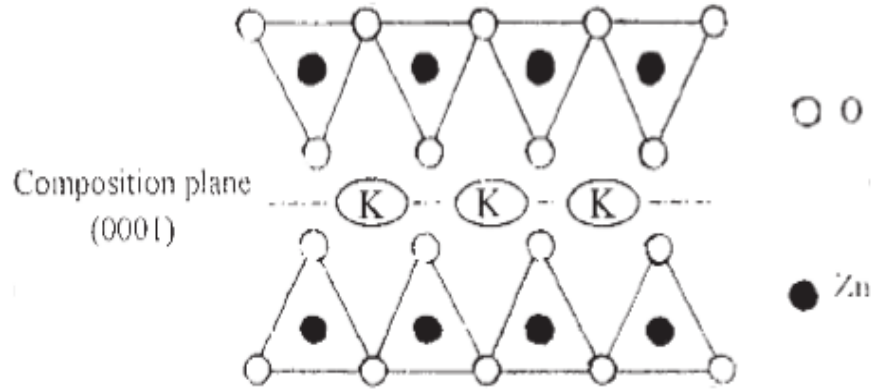


Figure 4.13: Formation of twin crystal nucleus by the linkage of ZnO_4^{-6} tetrahedral growth units by K^+ bridge. Reproduced with permission from John Wiley and Sons.[175]

point. Wang et al. suggested that in the nucleation step, the small crystals have large surface energy that can be lowered by the addition of ions in either the twin or normal positions.[175] If ZnO_4^{-6} tetrahedral ions are considered the growth units, then the K^+ or Na^+ from the addition of mineralizing salts can form bridges, $\text{ZnO}_4^{-6} - \text{Na}^+ - \text{ZnO}_4^{-6}$, which increase the stability of the units (Figure 4.13). Although the current preparation does not add additional mineralizing salts to the reaction mixture the free Na^+ from the NaOH would act as a stabilizing ion bridge. The stability of the ZnO_4^{-6} growth unit, however, compared to the more commonly accepted $[\text{Zn}(\text{OH})_4]^{2-}$ growth unit is still discussed in the literature and differs dependent on the energy model utilized.[175]

Alternatively, basal plane defects with inversion domain boundaries (IDB), a

type of homophase boundary,[176] have been found at the interface of twin dumbbell structures.[177] In the noncentrosymmetric structure of ZnO, inversion domain boundaries are the most common planar fault.[173] In the formation of the inversion boundary the crystal structure assumes a head-to-head configuration where the positive end, [0001] direction, of each end of the dumbbell is pointing to the IDB. The exposed end faces of the dumbbells are therefore the negative $(000\bar{1})$ planes. The growth rate of the $[000\bar{1}]$ direction is faster than that of the [0001] direction for dumbbell structures as the structures grow outwards from the exposed planes. The equal ratio of NaOH to $\text{Zn}(\text{NO}_3)_2 \cdot 6 \text{H}_2\text{O}$ used for the colloid synthesis also creates an environment with excess Zn^{2+} . These ions would adsorb to the oxygen-terminated or negative polar face $(000\bar{1})$ forming a surface rich in Zn^{2+} that mimics the positive polar face. The newly positive face can then adsorb $[\text{Zn}(\text{OH})_4]^{2-}$ growth units preferentially to the intrinsically positive (0001) polar face which is at the IDB boundary interface.

Many of the dumbbells are also hollow or exhibit small holes as the center of the exposed end faces. The structures are not hollow all the way through, however, but have holes that extend to differing depths. The suggested mechanism for the growth of the hollowed dumbbells is similar to that observed for tellurium nanotubes.[178, 179, 180] A secondary nucleation process occurs, early in the formation of the structure, preferentially on the circumferential edges of each of the hexagonal rods of the dumbbells because of the relatively higher free energies. The rapid growth and subsequent depletion of the growth units reduces the growth unit concentration in the bulk solution. Nucleation-induced concentration depletion has been observed in colloidal systems previously. After the secondary nucleation and growth begins, mass transport to the growing regions leads to under-saturation or depletion of the $[\text{Zn}(\text{OH})_4]^{2-}$ in the central region of the dumbbell, eventually forming a hollowed out hexagonal rod.[168, 178]

Low temperature methods. Low temperature methods are classified as such because they are conducted in an oven as opposed to a furnace and are kept below 80 °C as they are usually hydrothermal based methods. In low temperature methods a treated or untreated substrate is suspended in a growth solution which is usually

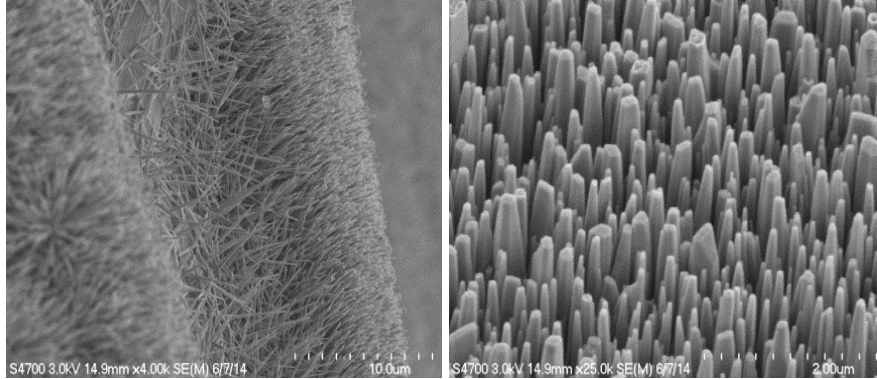


Figure 4.14: SEM images of nanowires grown on the same wafer by the low temperature hydrothermal method.

adjusted for Zn content and pH. A ZnO seed layer is often applied to the substrate for low temperature synthesis although there are low temperature methods where Zn metal foil was used as the seed layer instead.[159] The seeding solution was a 5 mM zinc acetate dihydrate solution in ethanol that was drop cast and dried onto a silicon wafer.[181, 182] The seeded layer is then annealed. The annealing temperature, seed layer thickness, crystallite size and deposition technique can affect the growth orientation of the nanowire array and the photoluminescence of the nanowires.[159] The drop casting method of seeding although effective was found to be sometimes inconsistent with respect to even distribution of seeds on wafers. This resulted in samples with mixed morphologies and also difficulty in reproducing experimental runs. Figure 4.14 shows two different regions on the same sample wafer where different nanowire morphologies were grown.

Other factors that affect aligned growth of nanowires in the low temperature method are the use of additives. These additives play the role of pH buffering agent, control the defect densities in nanostructures and facilitate axial growth.[183] Hexmethylenetetramine (HMTA) and polyethyleneimine (PEI) are common additives in low temperature growth.[181, 184] Figure 4.15 shows SEM images of nanowire arrays grown with and without PEI. The solution grown without PEI shows nanowires very

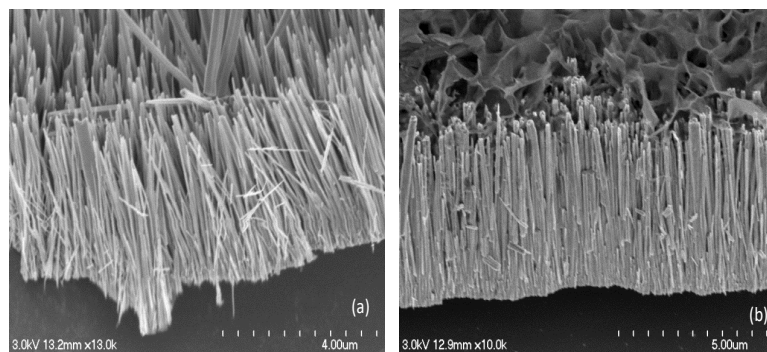


Figure 4.15: SEM images of nanowires grown (a) with 0.005 M PEI and (b) without PEI in the growth solution.

closely packed and fused together at the base. Additives such as PEI and HMTA are thought to adsorb to the (lateral) non-polar facets of the nanowire due to electrostatic affinity and effectively inhibit lateral growth.[87, 185]

4.4 Point defects

Point defects are the imperfections that occur in lattice of a crystal. Efficient or shallow donors and acceptors have energy levels close to the conduction or valence band, while others reside energetically deep within the forbidden band-gap and are considered deep centers.[186] Deep centers and defects can be classified as either native (intrinsic) or extrinsic. The common extrinsic deep centers in ZnO are the transition metal ions of Cu, Fe, Co and Mn and the ions of Li and Na.[186, 187] Intrinsic defects involve only the constituent elements of the crystal and include vacancies, interstitials and antisite defects. Vacancy defects are lattice sites, typically occupied in a perfect crystal, but are missing atoms. Interstitial defects occur when extra atoms occupy interstices in the lattice or sites in the crystal that usually do not have an atom. Lastly, antisite defects occur when atoms in the lattice exchange positions such as a O atom occupying a Zn position.

Defects, both extrinsic and intrinsic, can strongly affect the electrical and optical properties and doping of ZnO. Specifically, they can lead to additional absorption bands and emission bands at photon energies significantly below the band-gap.[186] Intrinsic defects are believed to be responsible for the unintentional n-type conductivity of ZnO.[119] Both oxygen vacancies (V_O) and zinc interstitials (Zn_i) have been separately cited as the root cause of this phenomenon.[188, 189] The source of the green emission in ZnO is another heavily debated material property. Again, both V_O and Zn_i have been ascribed as the source of this emission either separately or as combined contributors. In both cases the assignments are based on the indirect evidence such as trends in the increase or decrease of electrical conductivity with oxygen partial pressure and oxygen or zinc vapor annealing with the decrease in emission.[190, 191] Few studies have performed density functional calculations to confirm these hypotheses.[192]

In addition to the experimental work on point defects, extensive work has been done to understand them theoretically. The formation energies of point defects have been calculated with the intention of determining the point defects that dominate under certain conditions. Using first- principles density-functional calculation methods, the formation energies, transition levels and migration barriers of point defects can be calculated. The most common type of calculation method is the plane-wave pseudopotential density-functional calculation.[120] In density-functional theory, the total energy of a system of electrons at the ground-state, when subjected to an external Coulomb potential given by nuclei or ions, can be calculated. From the total energy the formation energy of defects can then be calculated.[119]

In this approach the concentration of native defects in a solid is related to the formation energy E^f by the equation [193, 119, 194]

$$C = N_{sites} \exp\left(\frac{-E^f}{k_B T}\right) \quad (4.5)$$

where N_{sites} is the number of sites in the crystal where the defect can occur. Equation 4.5 shows that at low formation energies there will be a high equilibrium concentration of the defects while at high formation energies the defects are unlikely to form and

the concentration will be low. The formation energy is also affected by growth or annealing conditions and if the defect is charged, it will also depend on the Fermi level (E_F). For an oxygen vacancy for example, the formation energy is determined by the number of Zn and O atoms in the environment given by the chemical potentials μ_{Zn} and μ_{O} . The chemical potentials depend on the experimental growth conditions which are either Zn-rich ($\mu_{Zn} = \mu_{Zn(bulk)}$), O-rich ($\mu_O = \mu_{O_2}$) or conditions in between.[120] The formation energy can then be written in terms of μ and E_F according to the following equation[119]

$$E^f(V_O^q) = E_{tot}(V_O^q) - E_{tot}(ZnO) + \mu_O + q(E_F + E_{VBM}) \quad (4.6)$$

where $E_{tot}(V_O^q)$ is the total energy of the a supercell containing the oxygen vacancy with a charge state q, $E_{tot}(ZnO)$ is the total energy of a ZnO perfect crystal in the same supercell and E_{VBM} is the valence band maximum (VBM). Equation 4.6 can be formulated for all of the native defects at any of their natural charge states. The Fermi level is taken with respect to the VBM and varies from 0 to the conduction band minimum (CBM) which is equivalent to the fundamental band-gap (E_g).

Figure 4.16 shows the formation energies of the different charge states of the native defects of ZnO as a function of Fermi energy. Calculated formation energies are typically presented this way to demonstrate the behavior of the defects with changes in the doping level. The transition level between charge states of a defect observed on the plots are indicated by kinks in the curve. The transition level ($\epsilon(q/q')$) is the Fermi energy at which the formation energies of the charge states q and q' are equal and is given by the equation

$$\epsilon(q/q') = [E^f(D^q; E_F = 0) - E^f(D^{q'}; E_F = 0)] / (q' - q) \quad (4.7)$$

where $E^f(D^q; E_F = 0)$ is the formation energy of the defect sate D at the charge state q when the Fermi level is at the valence band. At Fermi-level positions below this transition level q is stable, while above it q' is stable. The transition level also

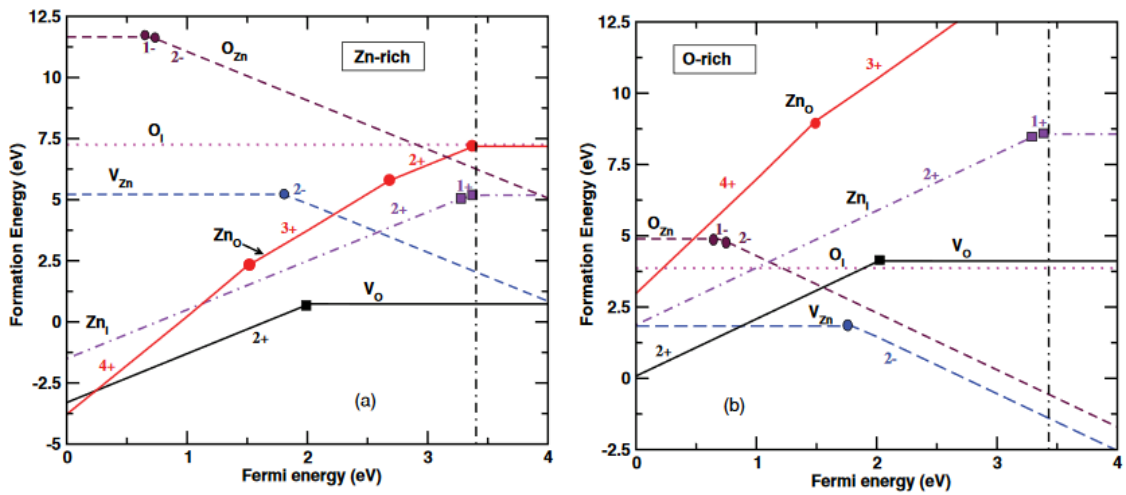


Figure 4.16: Formation energies as a function of Fermi level for Zn-rich and O-rich growth conditions calculated using GGA + U method. Dotted line represents the conduction band minimum of ZnO. Reproduced with permission from Physical Review B .[195]

corresponds to the thermal ionization energies. Shallow defects are more likely to be ionized at room temperature.

Various approaches have been used to calculate the formation energies and transition levels of native defects in ZnO. [196, 195, 119, 197] The results obtained from these approaches have differed from each other. For the local-density approximation (LDA) and generalized-gradient approximation (GGA), commonly used methods, the band-gap is severely underestimated by approximately 75%. [119] To overcome this, self interaction corrections such as LDA+U, GGA+U and B3LYP have been employed to compensate for the band-gap deficiency in the method. Vidya et al. reported a doubling in the value of the band-gap with a GGA+U calculation. [195] Figure 4.16 and 4.17 shows the formation energies for the native defects of ZnO as a function of Fermi level for both Zn-rich and O-rich conditions using GGA+U and LDA+U approaches respectively. The discrepancies in the results of the two methods are readily observable. For the Zn-rich conditions calculated using the GGA+U method oxygen vacancies (V_O) followed by zinc vacancies (V_{Zn}) and zinc interstitials (Zn_i) were the most abundant defects at the CBM. While for the LDA+U method zinc vacancies had the lowest formation energy, followed by zinc interstitials and oxygen interstitials. These differences in results make it somewhat difficult to definitively assign a single dominant defect at any one Fermi level.

Increasing the concentration of defects can also lead to the formation of defect complexes. There can be strong Coulombic interaction between donor-like and acceptor-like defects as well as strong attractive forces between donor defects. [198, 199] The implication of defect complexes on the electronic properties of ZnO are discussed in more detail in section 6.2.4.

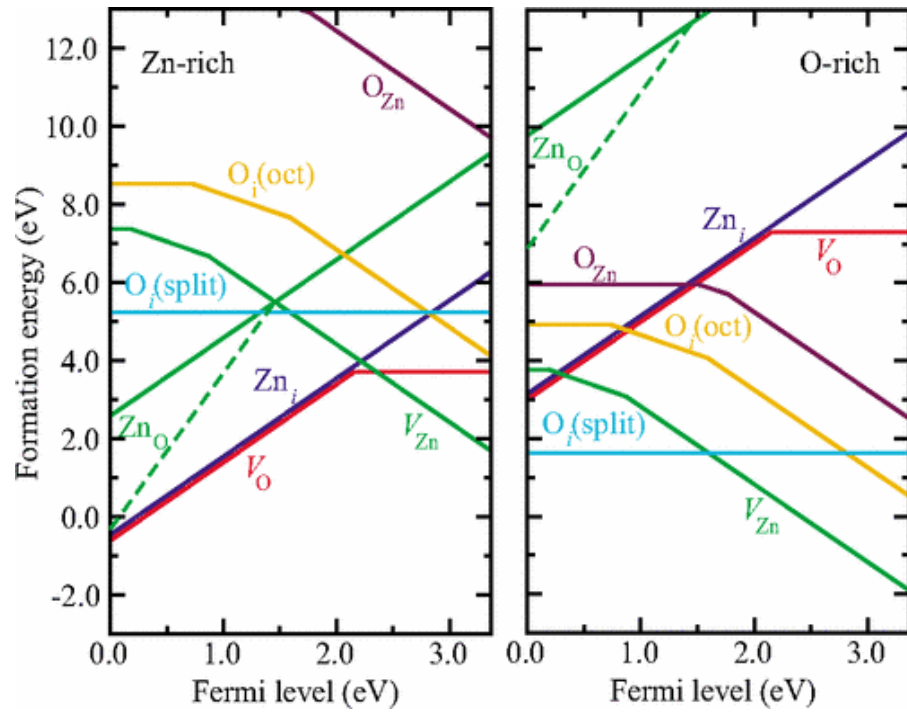


Figure 4.17: The formation energies as a function of Fermi level for Zn-rich and O-rich growth conditions calculated using LDA + U method. Reproduced with permission from Physical Review B .[119]

Chapter 5

ULTRAVIOLET FEMTOSECOND KERR-GATED MICROSCOPY

Equation 2.6 shows that if the emission wavelength of the sample is decreased then higher transmission could be achieved. Configuration of the setup for the UV detection range was necessary for measuring the wide bandgap metal oxides, outlined in the primary objectives in chapter 1, but it was also anticipated that the higher transmission of the signal from the sample would allow for a wider range of single nanowires that could be measured. In the configuration for visible detection only nanowires with emission intensities that saturated the CCD camera in the open gate configuration could be gated for measurement. This chapter outlines the results of the UV conversion of the setup and explores the capability of the setup through preliminary measurements of a single ZnO nanowire.

5.1 Kerr Medium Selection for the UV

The Kerr-gate is the heart of the setup and special consideration was taken when choosing the Kerr medium that would be used for measurements in the UV. In selecting the most appropriate Kerr medium, it is necessary to determine what compromise between time resolution and gating efficiency is appropriate for the samples to be measured. For this setup, the first criteria was that the Kerr medium be a solid crystal as opposed to a liquid. Although more popular in early applications of Kerr-gating,[201] the slow response time of liquid Kerr mediums outweigh the higher third-order nonlinearity (Kerr efficiency) exhibited. The response time of liquid or solution based Kerr mediums is primarily dependent on the rotational relaxation of the molecules and hence the average response-time is approximately 1.4 ps.[202, 203] While the Kerr response in optical glasses, on the other hand, is purely electronic

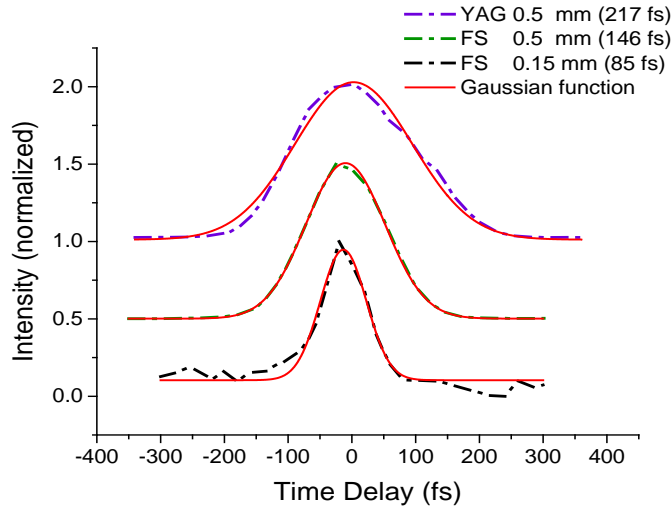


Figure 5.1: The instrument response function for YAG 0.5 mm and fused silica 0.5mm and 0.15 mm Kerr medium at 360 nm. Reprinted with permission from The Optical Society. [200]

[40]. CS_2 and benzene are the most commonly used liquid Kerr mediums. CS_2 has the larger nonlinear refractive index at both visible and UV wavelengths but benzene is usually favored because its Kerr response is dominated by electronic contributions (85%) and hence provides both a high Kerr efficiency and a faster response time. [40] The best reported response time for benzene is approximately 0.5 ps. [204, 205] Lastly, the vertical orientation of the setup is also better suited for a solid Kerr mediums which have the added advantage of ease of handling and do not need to be replenished periodically.

The selection of the Kerr medium was guided by the previous Kerr-gating study conducted by Yu et al. [203] The researchers showed that at maximum gating energy, yttrium aluminium garnet (YAG) and fused silica (FS) displayed high Kerr efficiency without excessive broadening of the transmitted signal. Although FS had the lowest nonlinear refractive index of all the materials measured, the fast temporal response was an attractive feature to examine in the new setup. To measure the instrument

response function (IRF), a 360 nm excitation pulse from the NOPA was reflected off a TEM grid that was placed at the sample position. Three different Kerr mediums were investigated, YAG (0.5 mm), FS (0.5 mm) and FS (0.15 mm). Figure 5.1 shows the normalized IRF for each Kerr medium. YAG (0.5 mm) showed the slowest response (217 fs) followed by FS (0.5 mm) at 146 fs. When the thickness of the FS was reduced to 0.15 mm the temporal response was also reduced to 85 fs.

The differences in the temporal resolution between the Kerr media is as a result of the group velocity mismatch (GVM) between the signal and the gate pulse. GVM or temporal walk-off occurs when pulses with different optical frequencies or polarizations propagate in a transparent medium because the respective group velocities are different.[206, 68] Pulses with an initial temporal overlap can eventually lose this overlap with propagation distance through the medium. The GVM is given by the equation

$$GVM = \frac{1}{\nu_{g1}} - \frac{1}{\nu_{g2}} \quad (5.1)$$

where ν_{gx} is the group velocity defined by the equation

$$\nu_g = \frac{c}{n_g(\omega)} \quad (5.2)$$

where $n_g(\omega)$ is the group index as a function of frequency. For YAG, the GVM between 800 nm and 400 nm is 3.94×10^{-10} s/m while for FS it is 1.56×10^{-10} s/m. The larger GVM in YAG would explain the slower temporal response. The GVM also plays a role in the difference in temporal response observed in the two FS windows. For FS (0.15mm) the pulses propagate a shorter distance than in the thicker FS (0.5 mm) window. Group velocity dispersion (GVD) also plays a role in temporal responses of the Kerr mediums, particularly in the asymmetry observed in the IRF for YAG. The GVD for YAG and FS at 400 nm is 244 fs^2 and 98 fs^2 respectively. Apart from the temporal resolution, the gating efficiency was also an important factor in choosing a Kerr medium. The peak transmission for YAG was 27% compared to 0.5 mm FS at 4

% and 0.15 mm at $\sim 0.5\%$. YAG was chosen as the Kerr medium for the new setup because it provided sufficient temporal resolution and the Kerr efficiency was greater than either of the FS windows. The ease with which the Kerr medium can be changed, however, provides the option for tailoring the setup to the sample being measured.

5.2 Preliminary Ultrafast Measurements

5.2.1 ZnO single nanowire samples

ZnO nanowires were epitaxially grown on fused silica wafers following a gold catalyzed vapor-liquid-solid (VLS) method outlined in section 4.3.1.[147, 150] The nanowires ranged from 300-800 nm in diameter and were approximately 50 μm in length. The predominant morphology was that of hexagonal cross section nanowires but SEM images of the bulk sample showed a mixed morphology where many of the nanostructures also displayed cylindrical and broader ribbon structures. Single nanowire samples were prepared by drop casting nanowires suspended in acetone onto silicon substrates and allowing it to dry. Ultrafast measurements were performed under ambient conditions and only on single nanowires unobstructed by loose debris or other nanostructures. The single nanowires were further characterized by SEM and with an inverted fluorescence microscope.

5.2.2 Steady State Measurements

Figure 5.2 shows images of the single ZnO nanowire measured in this study. The SEM image (Figure 5.2 (a)) shows the unobstructed nanowire of interest. The inset shows a magnified image of one end facet of the wire. The nanowire appears cylindrical in cross section with a smooth surface morphology. Figure 5.2 (b) and (c) show the false-color steady-state (open gate) images of the nanowire at low (4.4 mJ/cm^2) and high (13.2 mJ/cm^2) fluence, respectively. At low excitation fluence, the photoluminescence is isotropic along the full length of the nanowire. Increasing the pump fluence results in enhanced emission intensity from a localized region on the nanowire and from one end of the nanowire. It should be noted that the localization

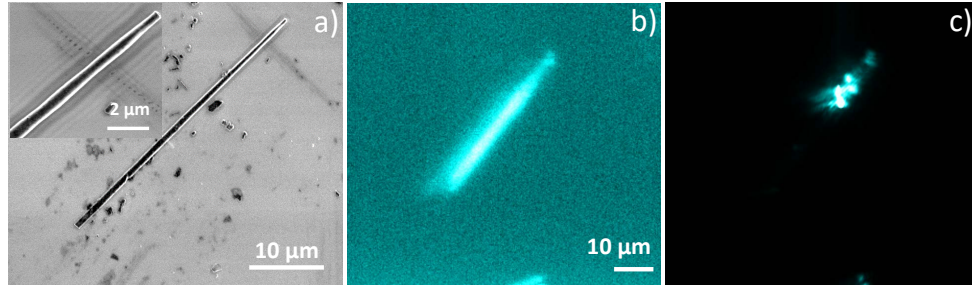


Figure 5.2: (a) SEM image of a single ZnO nanowire. (b) Open-gate image of the same nanowire at (b) low fluence (4.4 mJ/cm^2) and (c) high fluence (13.2 mJ/cm^2). Reprinted with permission from SPIE.[207]

cannot be attributed to the intensity profile of the excitation beam. When the sample was moved while the excitation beam kept in place, there were no change in the intensity or pattern of the emission on the nanowire.

The enhanced localized emission observed in Figure 5.2 (c) is indicative of a transition to amplified spontaneous emission (ASE) or the early onset of lasing (section 1.1).[57] This transition is also observed in the steady state spectra (Figure 5.3(a)) when the fluence is increased above 4.4 mJ/cm^2 . At 4.4 mJ/cm^2 the spectrum is a broad and featureless band representative of spontaneous emission. At 6.2 mJ/cm^2 the emission intensity increases by a factor of 15 and the full-width at half-maximum of the emission peak at 385 nm narrows sharply to 2.4 nm . Above the estimated threshold fluence of 6.2 mJ/cm^2 spectral peaks broaden and blue shift. The blue shifting of emission peaks is attributed to a high carrier density in the gain region. Increasing the carrier density can result in a reduction of the refractive index as well as occupation of higher lying states due to a saturation of low-lying states.[208, 209] The latter can result in a blue shift as well as broadening of the bandwidth.[47, 210] Due to the high excitation intensity sample heating effects can also occur and result in spectral line broadening.[209]

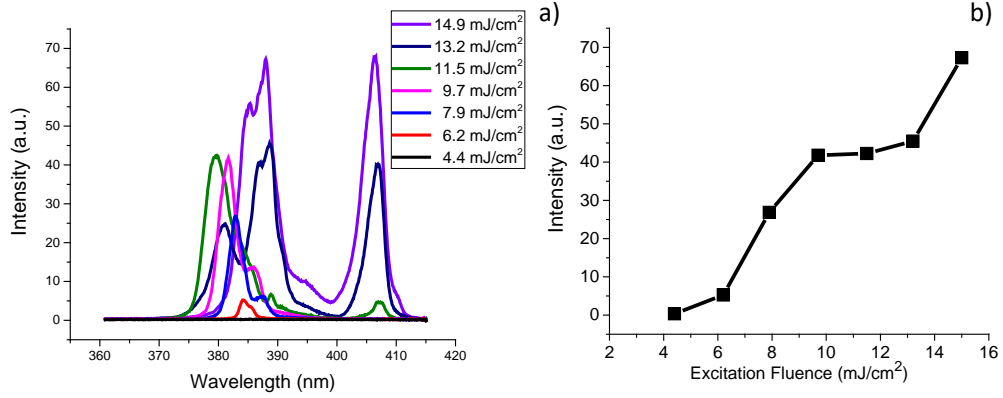


Figure 5.3: a) Power dependent emission spectra of the same ZnO nanowire. (b) The emission intensity dependence of the pump fluence. Reprinted with permission from SPIE.[207]

Red shifted peaks also accompany the blue spectral shift. These low energy modes appear in the spectra at 7.9 mJ/cm² and increase in intensity with the increase in excitation fluence while the preexisting high energy modes decrease and eventually completely disappear from the spectra at 14.9 mJ/cm². The observed features in the spectra are a result of mode competition occurring in the nanowire. The nascent low energy modes compete for the available optical gain while the high energy modes become quenched.[209]

A red-shift in emission peaks is also often observed in the transition from low pump fluence, the exciton-exciton recombination regime, to high fluence, electron-hole plasma (EHP) regime, in stimulated emission processes of wide bandgap semiconductors like ZnO and GaN.[47, 211] The transition to the electron-hole plasma recombination in nanostructures occurs when the excitation fluence is sufficiently high to produce carrier densities higher than the Mott density of ZnO. The Mott density for thin films of ZnO has been reported to lie within a range of 10^{17} cm⁻³ to 10^{20} cm⁻³. [209, 210, 110]

The charge carrier densities were estimated using the expression [212]

$$N = (1 - R)I\alpha \quad (5.3)$$

where R is the reflectivity coefficient ($R=0.15$), I is the photon fluence and α is the absorption coefficient.[213] Assuming that all incident pump photons were absorbed by the nanowire based on the large absorption coefficient ($2 \times 10^5 \text{ cm}^{-1}$), the calculated carrier density was estimated to range from 5.5×10^{20} to 2.4×10^{21} for fluences of 4.5 mJ/cm^2 to 16.4 mJ/cm^2 . [214] At the lowest excitation fluence the calculated carrier density is at the higher end of the above designated range for the Mott density while at the highest measured fluence the calculated carrier density is a magnitude higher than the higher end of the range. A consequence of such high carrier density is band gap renormalization (BGR).[209, 210, 215] The excitation fluence provided suggests that the carrier density is well within the range for this phenomenon to occur. The above expression for carrier density does not take into account recombination so the actual carrier density will be lower than this approximation. Similar studies on ZnO nanowires have reported surpassing the Mott density with fluences orders of magnitude lower than that used in this study. [211, 216] The actual carriers generated, therefore, should still be sufficient enough to approach that of the Mott density and enter the regime of electron-hole plasma states.

Figure 5.3 (b) shows the emission intensity of the spectral peaks as a function of the excitation fluence. Below the threshold fluence (6.2 mJ/cm^2) there was only one excitation intensity measured but a linear trend between the spectral peak intensity and excitation fluence is suggested. Above the threshold fluence the spectral intensity dependence on fluence increases superlinearly indicating either ASE or the initial onset of stimulated emission.[215]

Fulfilling the criteria of sufficiently high carrier densities that exceed the Mott density does not definitively prove that ZnO nanowires have transitioned from exhibiting ASE to stimulated emission.[110] At the Mott density excitons become destabilized and are completely dissociated to form an EHP.[216] To achieve the gain process, the

EHP must be degenerate and the chemical potential of the electron-hole pair system or the difference in the energy level of the quasi-Fermi level of the electrons and holes must be larger than the reduced band gap according to the equation

$$\mu(n_p, T) = E_e^F(n_p, T) - E_h^F(n_p, T) \geq E_g'(n_p, T) \quad (5.4)$$

At room temperature the carrier density that satisfies equation 5.5 is $\approx 10^{19}$ cm^{-3} which is an order of magnitude lower than the carrier density generated at the lowest fluence in this study.[110] The microscope setup therefore easily facilitates excitation that generates charge carrier densities in single ZnO nanowires that fulfill the EHP lasing condition.

The observed features of the spectra are, however, inconsistent with a purely stimulated emission process. The emission bandwidth broadens after 6.2 mJ/cm^2 as previously mentioned and there are no distinguishable Fabry- P erot modes. The broadening of the bandwidth has been previously associated with enhanced ASE in nanowires.[215] Additionally, although the end facet of the nanowire displays a high intensity of emission at higher fluence, the region with the most enhanced emission is not from the end of the wire but from along the length where there is no noticeable faceted mirror surface (Figure 5.2(c)). It is therefore postulated that the emission from the nanowire is dominated by ASE. The physical imperfections of the nanowire make it difficult to observe true Fabry- P erot type lasing where a well-defined cavity is a major prerequisite as previously mentioned. ASE can however still be achieved.[51]

5.2.3 Time-resolved Spectroscopy

Figure 5.4 (a) and (b) shows the transient spectra measured for the same ZnO nanowire at 14.9 mJ/cm^2 and 16.4 mJ/cm^2 . Each spectra shows two distinct high intensity peaks, outlined with solid black contour lines, that occur sequentially. The first peak reaches a maximum intensity at 0.5 ps while the second peak is blue-shifted and reaches a maximum at a time delay of 1.3 ps. Figure 5.2 (c) shows that at high fluence the enhanced emission intensity along the wire is established at two separate

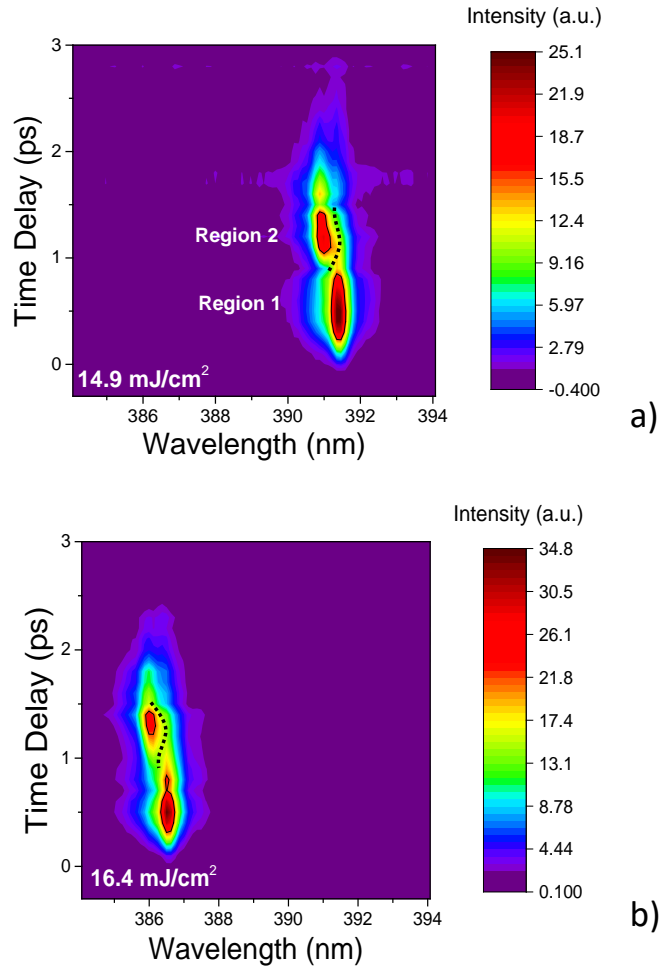


Figure 5.4: a) Time resolved spectrum of the same ZnO nanowire at (a) 14.9 mJ/cm^2 and (b) 16.4 mJ/cm^2 . Black dotted line shows the red-shift due to BGR with delay time. Reprinted with permission from SPIE. [207]

regions along the length of the nanowire. The time delay of the emission between each region is also detectable in the sequential imaging or movie of the emission from the nanowire, as discussed under time resolved imaging (section 5.2.4). The two separate peaks in the transient spectra are therefore due to two different regions of confinement on the nanowire that emit at slightly different wavelengths, 391.4 nm and 390.9 nm for region 1 and region 2 respectively, at 14.9 mJ/cm². The emission from each region appears to be independent of each other. When the fluence is increased from 14.9 mJ/cm² to 16.4 mJ/cm² the emission intensity increases and emission from both regions become blue-shifted by 258 eV while the same blue-shift between the peaks is maintained. The blue shift with increase in fluence was discussed previously and attributed to the dependence of the refractive index on the carrier density.

At both fluences the peak due to region 2 shows an asymmetrical bandwidth broadening, highlighted by a black dotted line, that is more prominent towards the longer wavelengths followed by recovery back to shorter wavelengths with time. This is characteristic of band gap renormalization (BGR) where hot carriers cool via a quasi-thermalized equilibrium process that builds up to the EHP and the bandgap is renormalized.[215, 217, 218] The carrier density decays via recombination and the normal band gap is reestablished. The time scale for the buildup of the EHP and recovery of the bandgap is much faster (≈ 250 fs) than in previous studies which reported timescales ranging from 3-6 ps.[215, 217, 219] These studies have reported time resolutions above 300 fs so changes that may occur on timescales in the sub 300 fs range would likely be undetectable. Additionally, the excitation fluences used in this study were three orders of magnitude larger than in the previously reported studies. The higher excitation fluences would generate higher carrier densities on a faster time scale and lead to faster decay times.

For region 1 the bandwidth appears to broaden more evenly in both the long and short wavelength direction at both fluences. The competing effects of the BGR, which causes the red-shift, and the transient reduction in refractive index, which causes a blue-shift, with the increase in carrier density could lead to the homogeneous spreading in

the bandwidth with time. The bandwidth broadens and recovers on a time scale of 600 fs at 14.9 mJ/cm² while at 16.4 mJ/cm², region 1, appears to exhibit two instances of bandwidth broadening and recovery with the first instance occurring on a time scale of ≈ 420 fs and the second at ≈ 140 fs.

The scale of the transient spectra shown in Figure 5.4 was truncated to omit the longer wavelength region. None of the longer wavelength peaks (> 400 nm) that were observed in the steady state spectra appeared in the transient spectra. There are several explanations for this absence. Firstly, in the closed gate configuration, the microscope is only sensitive to ultrafast signals (≤ 100 ps), therefore, longer lived signals are subtracted as constant background on the short timescales on which measurements are performed. Alternatively, higher temperatures due to higher excitation fluences typically cause an increase in refractive index and a red-shift in the emission peaks.[47, 210] Further red-shifts of already red-shifted emission peaks could be at the edge of the detection range of the microscope (≈ 420 nm) resulting in low signals that cannot be sufficiently gated by the microscope.

5.2.4 Time-resolved Imaging

Figure 6.3 (a) shows transient images depicting the emission from the single ZnO nanowire collected at different delay times at an excitation fluence of 16.4 mJ/cm². The Kerr-gated microscope setup supports the capability of observing the location of the emission from the single nanowire as well as the change in the emission with time. The ZnO nanowire in this study had multiple regions of enhanced localized emission apart from the ends of the nanowire. These regions have different emission onset times and different emission wavelengths, as discussed previously. Figure 5.4 (b) shows that the onset of emission from region 2 does not occur until approximately 1 ps which correlates with the appearance of region 2, highlighted by the yellow box, in Figure 6.3 (a). Hence the peak assigned to Region 2 in Figure 5.4 (b) can be attributed to the emission region highlighted by the yellow box.

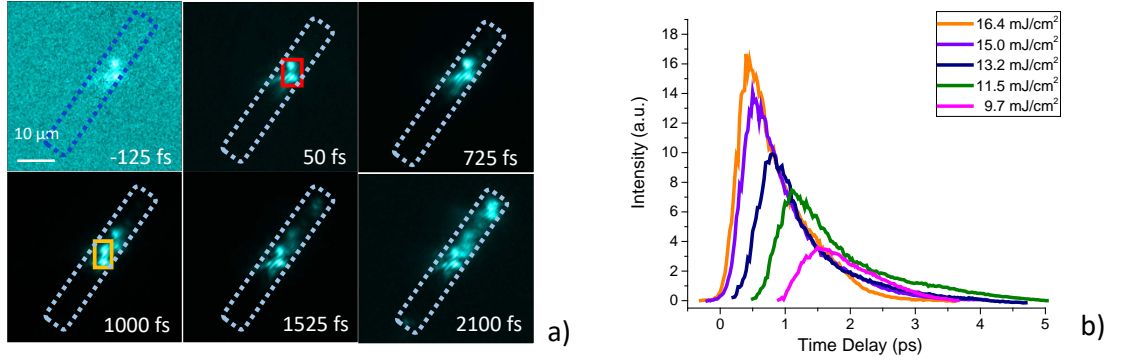


Figure 5.5: (a) Transient image sequence of a single ZnO nanowire excited at 16.4 mJ/cm^2 . The red and yellow boxes demarcate region 1 and 2 respectively. (b) Transient dynamics extracted from region 1 on the nanowire at fluences ranging from 9.7 mJ/cm^2 to 16.4 mJ/cm^2 . Reprinted with permission from SPIE.[207]

The discrete areas of emission from regions other than the ends of the nanowire suggest possible growth initiated anomalies in the morphology. In both region 1 and 2, two obliquely opposite bright areas are observed indicating that light is confined in these regions although the SEM images of the nanowire show a cylindrical morphology without flat, lateral end faces to make up a resonant cavity. If a lateral cavity is assumed to have been established in both region 1 and 2 then the cavity resonance frequency is

$$\nu \approx cm/2n(\lambda)L \quad (5.5)$$

where m is the longitudinal mode number, $n(\lambda)$ the wavelength dependent refractive index described by a Sellmeier model and L is the cavity length.[210] If there are changes in the thickness of the nanowire along the length, then the established cavity distance (L) would change and hence the emission wavelength could differ between region 1 and region 2. The size of the nanowire or cavity size, however, has

been reported to not affect the onset time of nanowire lasers.[220] The difference in emission delay times for both regions is most likely as a result of differences in the density of carriers generated in each region. The carrier density is dependent on the absorbance and so changes in the position or geometry of the crystal axis can affect the absorbance and hence change the carrier density.[59] A more detailed discussion on changes in carrier density generation and hence dynamics in individual nanowires is undertaken in chapter 6.

Figure 6.3 (b) shows the transient dynamics extracted from region 1 at different excitation fluences. Increasing the excitation fluences causes shifts to earlier delay times as well as faster decay times. Increasing the fluence from 9.7 mJ/cm^2 to 16.4 mJ/cm^2 results in $\approx 1 \text{ ps}$ shift to earlier time. This effect has previously been reported and is attributed to the increase in carrier density generated by the increase in excitation fluence.[211, 59] For extracted transients shown in Figure 6.3 (b), the ASE rate model can be applied to fit the measured data and the recombination rates for Shockley-Read, non-geminate and Auger processes can be determined. Chapter 6 discusses fitting the ASE model to transient emission extracted from a single ZnO nanowire.

5.3 Conclusion

Converting and optimizing the femtosecond Kerr-gated microscope system for detection of UV emission has made it possible to measure the transient emission of single ZnO nanowires. The higher transmission affords larger signal-to-noise ratio and allows for greater number of nanowires with sufficient gated signal to be measured.

The preliminary ultrafast measurements conducted on a single ZnO nanowire show that the set up can provide large excitation fluences to generate large carrier densities in the single nanowire. These carrier densities are large enough to exceed the Mott density of ZnO. The high temporal resolution of the setup also facilitated the observation of the ultrafast phenomenon associated with large carrier densities like band-gap renormalization. The sensitivity of the setup allowed for small changes in emission wavelength to be distinguished between two different regions on the single

nanowire. The combined transient spectral and temporal imaging modes are shown to be a powerful tool for accurately assigning ultrafast phenomenon occurring in single wide band-gap nanostructures.

Chapter 6

KERR-GATED MICROSCOPY FOR MEASURING DEFECT DENSITY

Defects naturally abound in semiconductor crystal structures and their presence either debilitate or improve device functionality. The increasing trend to strategically implant or remove specific defects to tailor the properties in materials via defect engineering has made it imperative to quantify these defects in nanostructures. Here we report the use of an ultrafast Kerr-gated microscope system to characterize the changes in defect density at different locations on a single nanowire. By measuring the evolution of nonlinear luminescence dynamics from a single nanowire with an engineered defect profile we are able to extract the individual non-radiative recombination constants and obtain the defect density at locations along the nanowire length. This new method promises fast, reliable and contactless characterization of single nanoparticles.

6.1 Introduction

Imperfections in the crystal lattice of nanostructured materials are an unavoidable part of the synthetic process. Common irregularities in the crystal periodicity such as native point defects affect the performance of semiconductor devices dramatically and significant effort is taken to reduce or minimize their occurrence. Apart from influencing the electrical and optical properties of the semiconductor itself by affecting carrier lifetime and luminescence efficiency, defects increase device switching times, lower gain in transistors, reduce power production in solar cells and accelerate the degradation of a device.[119, 221, 222] Although both native and extrinsic point defects are often considered undesirable, rather than combat them some recent approaches have chosen to harness their characteristics as a means of optimizing specific optoelectronic properties. Defect engineering of nanostructures has yielded promising

advances such as enhanced sensor sensitivity and electrical properties,[223] and increased photocatalytic behavior.[224] Whether they are beneficial or detrimental to an application, being able to quantify defects on the single nanostructure scale is essential to fully control and exploit device properties.

The vast majority of studies conducted on point defects have focused on either identification or computationally predicting their stability.[198] Other works describe changes in defect density qualitatively through the increase or decrease of a spectroscopic band signal.[225] For quantifying defect density, techniques such as deep level transient spectroscopy (DLTS) and impedance spectroscopy are the most commonly used but both require contacts for an external electrical connection and DLTS is also only sensitive to deep level defects.[226, 227] Techniques that do not require contacts are usually either spectroscopy or microscopy based such as Raman spectroscopy.[228] These methods are, however, often restricted to bulk sample measurements. Other methods with the spatial resolution to measure single nanostructures, which include scanning tunneling microscopy, transmission electron microscopy and scanning transmission X-ray microscopy, are laborious and time consuming or involve material specific reactions.[229, 230] SEM-cathodoluminescence imaging and spectroscopy, although a highly utilized tool for investigating defects on the nanoscale, is also only qualitative and more appropriate for identifying spatial distribution of defects. [231]

Here we present an alternative approach based on evaluating femtosecond non-linear luminescence dynamics. The ultrafast luminescence dynamics that is observed after strongly exciting a semiconductor is generated by amplified spontaneous emission (ASE). ASE dynamics is very sensitive to non-radiative decay processes that are associated with defect induced recombination. The recombination rates can in turn be used to quantify defect densities. The advantage of ASE over linear luminescence is the ability to distinguish between different recombination processes. Figure 6.1 shows a scheme for the generation of ASE and the defect induced non-radiative recombination processes that are involved. To date, the wealth of information that is contained in an ASE signal has not been fully utilized. This is primarily because ASE decays on

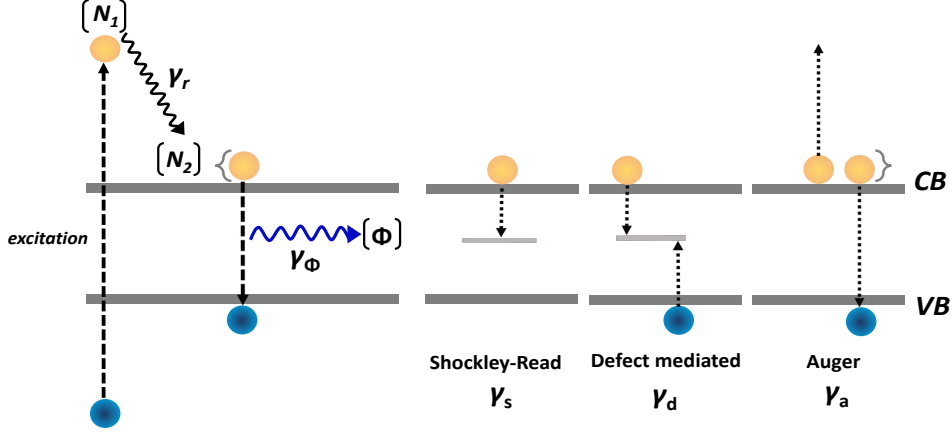


Figure 6.1: Scheme showing the amplified spontaneous emission rate model. The N_1 is excited initially and then relaxes to the N_2 state at the band edge at a rate of γ_r . The rate of loss of photons due to radiation is given by γ_Φ . The photon field population ($\Phi(t)$) and the carrier population in N_2 are linked by a feedback mechanism that results in oscillations in the emission intensity. The three competing recombination pathways Shockley-Read-Hall (γ_s), non-geminate (γ_d) and auger (γ_a) act to dampen these oscillations and serve as channels for non-radiative recombination.

a few picosecond time scale for systems without optical confinement. The ability to record luminescence movies with micrometer spatial resolution and femtosecond time resolution allows us to employ ASE dynamics for studying non-radiative decay rates and the related defect densities in single nanoparticles.

Femtosecond luminescence movies are recorded via a Kerr-gated luminescence microscope (KGM). KGM provides the required spatial resolution and sub 90 fs time resolution for resolving non-linear ASE along a single nanowire. In conjunction with an established model for ASE and lasing dynamics, this method allows the determination of recombination constants and defect densities in single nano-particle and along single nanowires.

We exemplify the new method on ZnO nanowires. ZnO nanoparticles are used in a broad range of applications. Its dominant point defects, oxygen vacancies and Zn

interstitials, have been investigated extensively. ZnO nanoparticles have been synthesized through various routes in a plethora of morphologies. Since the presence of point defects in a nanostructure is dependent on growth parameters, morphology and the post growth environment, the defect profile of a single nanowire can be manipulated by altering preparation conditions. We use a well established CVD synthesis, that alternates between zinc-rich and oxygen-rich conditions, to prepare ZnO nanowires with a defect density gradient to test the sensitivity of ASE to defect densities.

In this study we use a femtosecond Kerr-gated microscope to probe the non-linear temporal luminescence dynamics in the near UV on a single ZnO nanowire. The signal was modeled and used to quantify defect mediated non-radiative recombination. We were able to correlate rate constants for defect mediated recombination at different spots along the wire to a gradient in defect density.

6.2 Results and Discussion

6.2.1 Steady state measurements

The single ZnO nanowire measured in this study is shown in Figure 2. The SEM image of the ZnO nanowire (Figure 2 (a)) shows the morphology to be a tapered cylindrical nanostructure with flat end facets and a surface morphology that was rough on the nanometer scale. The nanowire was $14.5 \mu\text{m}$ in length, measured 575 nm at the base and narrowed to 325 nm at the tip with a tapering angle of approximately 1.02° . The two nodules located on the lower portion of the nanowire are debris from other nanostructures created during the sample preparation process and are not part of the intrinsic morphology of the nanostructure. They show no luminescence either under high excitation or in a fluorescence microscope (SI 2).

Figure 6.2 (b) and (c) are the false-color luminescence emission images of the nanowire at low (7 mJ/cm^2) and high (14 mJ/cm^2) excitation fluence respectively. At low fluence the photoluminescence from the nanowire was isotropic along the full length of the nanostructure. Increasing the fluence resulted in localized regions of enhanced emission from the both end facets of the nanowire. The enhanced emission region from

the tip of the nanowire was larger and more intense than the emission from the base. The debris nodules located on the nanowire surface did not overlap with the regions of enhanced emission selected from either end of the nanowire.

The fluence dependence of the luminescence is a clear indication of amplified spontaneous emission.[57, 49] ASE is the process of amplification of spontaneously emitted photons by stimulated emission as light propagates in a medium. [48, 232]. This type of *mirrorless* lasing exhibits characteristics between that of a coherent laser and an incoherent light emitting source.[233] These intermediate features are observed in the spectra (Figure 6.2 (d)) taken of the field of view of the microscope containing the nanowire. At low fluence (5.29 - 7.05 mJ/cm^2) the spectra is broad and feature-less. Increasing the excitation fluence above this threshold results in an increase in emission intensity by a factor of 6 and the emergence of multiple modes. The full width half maximum of the spectra narrows from 35 nm to 9 nm with increase in fluence from 7.05 mJ/cm^2 to 8.81 mJ/cm^2 . Re-broadening of spectral peaks has previously been observed for ASE in nanowires.[234] The dependence of the emission on the fluence is shown Figure 6.2 (e). At fluences above the apparent threshold the emission intensity rises sharply with increase in excitation fluence which is indicative of onset of ASE. [235, 49] It should be pointed out that the sensitivity of the setup to ultrafast (sub 50 ps) and ultraviolet (360-420 nm) fluorescence precludes the detection of emission from ZnO defect states which are commonly observed between 500-600 nm visible range with photoluminescence lifetime on the nanosecond time scale.

Nanowire lasing has frequently been reported for ZnO nanowires in connection with luminescence emission from the tips as shown in Figure 6.2.[234] However, as discussed above, the observed spectral and power dependence can be explained without the need for optical confinement. In addition, the SEM image in Figure 6.2 (a) does not show well-defined end facets that form a cavity. Finite-difference time-domain (FDTD) calculations, Figure 6.7 in section 6.4, were also performed to calculate the spatial distribution of the optical field intensity of the excitation pulse. These calculations show that the field on both ends is about a factor 30 higher compared to the center.

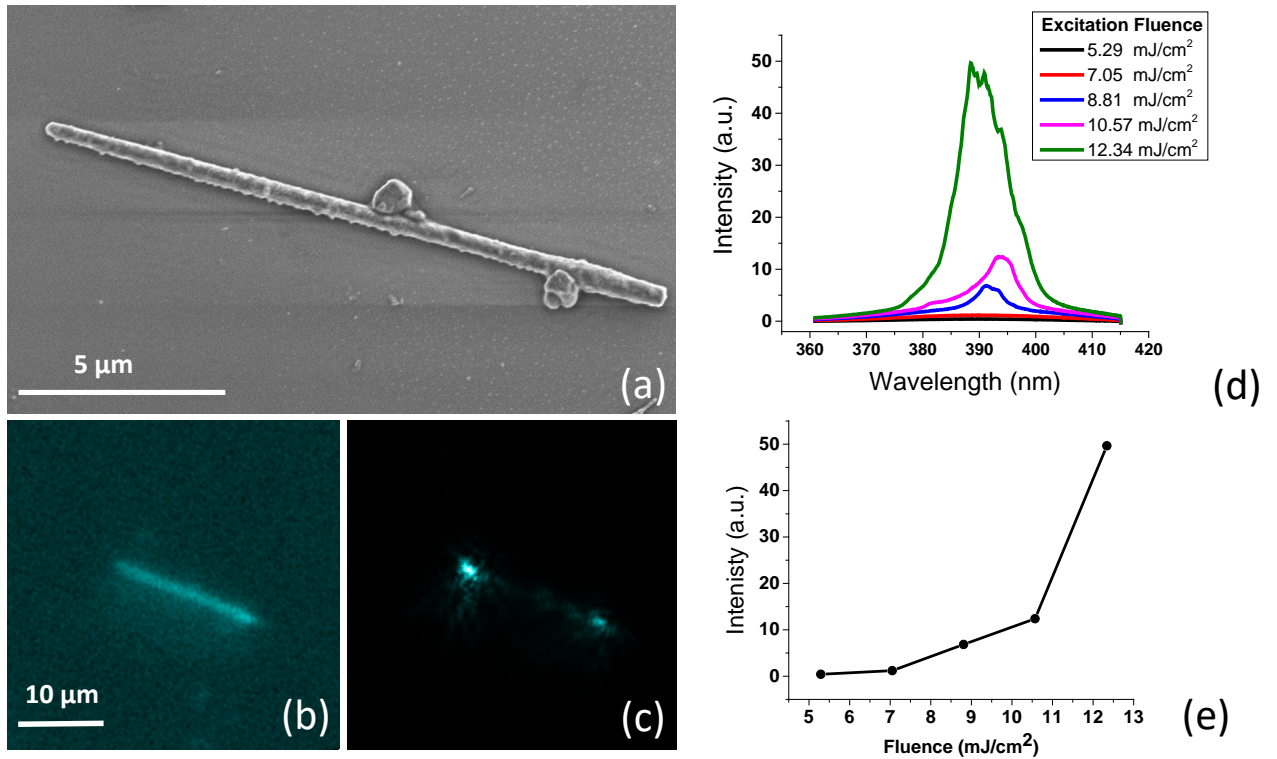


Figure 6.2: (a) Scanning electron microscopy image of the single ZnO nanowire measured in this study. Loose ZnO debris particles on the surface of the nanowire were from sample preparation and are not apart of growth morphology. False-color fluorescence micrographs at (b) 7 mJ/cm^2 and (c) 14 mJ/cm^2 . Discrete regions of enhanced emission are observed on the nanowire above the the threshold fluence of 5.5 mJ/cm^2 . (d) Power dependent emission spectra (inset: the power dependence of emission with excitation intensity) and (e) The power dependence of the emission with excitation intensity.

This explains why non-linear ASE is much stronger from the tips at high fluences. It should be noted that, while the center region of the wire in Figure 6.2(c) appears to be dark there is still notable luminescence.

The excitation provided by the setup, however, easily generated carrier densities that exceeded the Mott density of ZnO which has been reported to lie within the range of 10^{17} to 10^{20} cm^{-3} . [50, 110] Assuming all photons incident on the nanowire were absorbed due to the large absorption coefficient of ZnO (2×10^5) [236], the calculated carrier densities were estimated to range from 6.6×10^{20} cm^{-3} to 2.25×10^{21} cm^{-3} for 5.3 mJ/cm^2 to 18.2 mJ/cm^2 , respectively. At the lowest excitation fluence the carrier density is still larger than the largest reported value of the Mott density for ZnO. At carrier densities that surpass the Mott density, the electron-hole plasma (EHP) recombination mechanism occurs and enhanced emission phenomenon such as ASE and onset of stimulated emission is observed. [50, 110]

6.2.2 Time resolved measurements

The temporal emission from the single ZnO nanowire was tracked via fluorescence micrographs taken at predetermined time steps at progressively longer delay times (Figure 6.3 (a)). Two regions of interest along the nanowire, the two end facets, were selected (colored boxes) for comparing Zn-rich and oxygen-rich regions. The sequential time resolved images show the two bright end facets of the nanowire appeared at approximately 0.5 ps and then disappeared at 4.3 ps. The images also show that emission from the tip, the region enclosed by the orange box, was more intense than the emission from the base, the region enclosed by the blue box. Additionally, emission intensity from both ends were brighter than the middle region of the nanowire which appeared dark in contrast. Figure 6.3(b) shows the regions labeled 1 and 2 overlaid on the SEM image of the nanowire. The highlighted regions shown did not encompass the debris on the nanowires surface. The transients extracted from both regions at excitation fluences 11.5 - 18.2 mJ/cm^2 , shown in Figure 6.3 (c)-(d), are obtained by integrating the emission intensity at each location for a designated time step. The

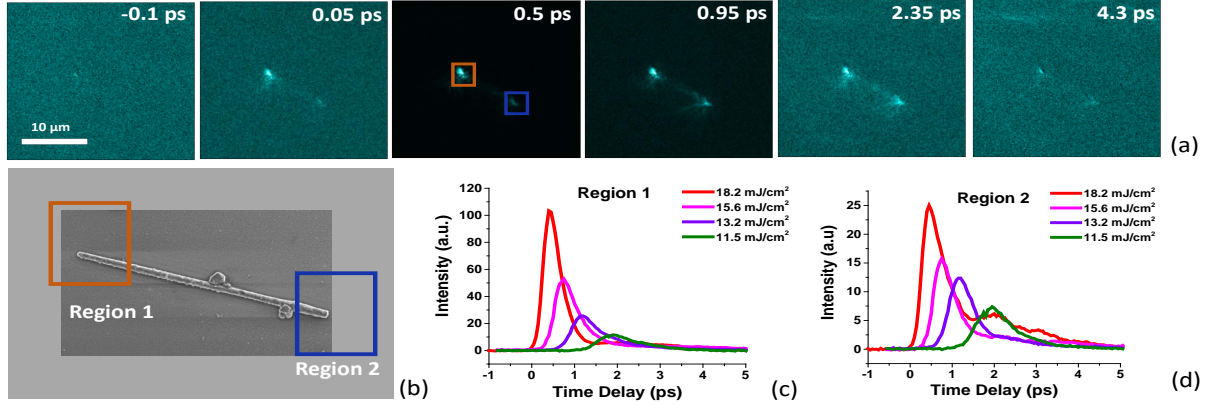


Figure 6.3: (a) False-color luminescence images of the single ZnO nanowire at different delay times after excitation at 18.2 mJ/cm^2 in transient mode. The two colored boxes at 0.5 ps represent the end facets of the nanowire. (b) The corresponding SEM image of the nanowire and the location of the regions (Region 1 and 2) of interest with respect to the debris particles on the surface. (c) and (d) The extracted transient dynamics from region 1 and 2 at excitation fluences $11.5\text{-}18.2 \text{ mJ/cm}^2$.

temporal emissions from each region show a strong excitation fluence dependence. As the fluence was increased the peak emission shifted to progressively earlier onset times. This time dependence is typical for ASE and is attributed to the decrease in time required to form emissive states at high carrier densities and the induction time to threshold.[234] At higher fluences a second maximum was also observed at region 2.

The extracted single transients from each region at the highest excitation fluence (18.2 mJ/cm^2) are shown in Figure 6.4 (a)- (b) for comparison of the dynamics. Emission from region 1, which is shown to be the brighter region in the temporal images above, had a measured intensity that was approximately four times the intensity at region 2. This difference in emission intensity can not be attributed to the beam intensity profile as the spot size ($85\mu\text{ m}$) was larger than the full length of the nanowire by a factor of 6 and the change with intensity along the nanowire would have steadily increased or decreased from one end of the nanowire to the other. In addition to the

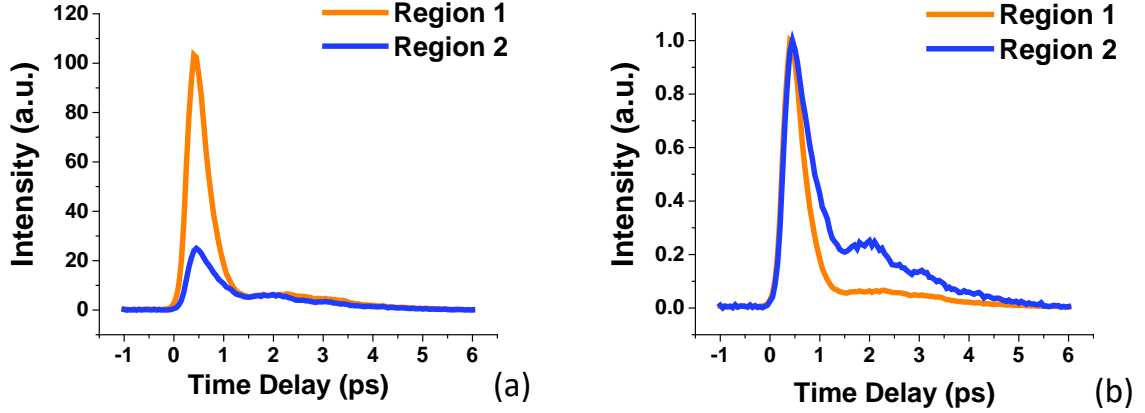


Figure 6.4: (a) Transients extracted from each region depicting the evolution of the emission and the relative emission intensity at a fluence of $18.2 \text{ mJ}/\text{cm}^2$. (b) Normalized emission transients from each region showing the change in emission dynamics at each location on the nanowire.

change in emission intensities, each region exhibited distinctive temporal dynamics. Figure 6.4 (b) shows the normalized transient emission at each region at a fluence of $18.2 \text{ mJ}/\text{cm}^2$. Both regions have the same onset time (0 ps) but region 2 shows a second maximum occurring at a delay time of 2 ps while region 1 shows a significantly less prominent peak at the same delay time. Transients extracted from the middle region of the nanowire are discussed in section 6.4.

6.2.3 Recombination rates from the Amplified Spontaneous Emission Model

Expounding the different relaxation pathways that influence the observed emission dynamics unique to each region on the nanowire was done by applying an ASE model, described in section 1.1 to the emission data. To recall, the system is described by a set of coupled rate equations

$$\frac{d}{dt} N_1(t) = AV_p(t) - \gamma_r N_1(t)$$

$$\frac{d}{dt} N_2(t) = \gamma_r N_1(t) - B\Phi(t)N_2(t) - \gamma_s N_2(t) - \gamma_d N_2(t)^2 - \gamma_a N_2(t)^3$$

$$\frac{d}{dt} \Phi(t) = B\Phi(t)N_2(t) - \gamma_{\Phi}\Phi(t) \quad (6.1)$$

where N_1 and N_2 are the carrier densities generated in the short-lived high excited state and band edge respectively, A is the Gaussian pump pulse (excitation fluence), B is the stimulated emission rate, γ_r is the relaxation rate from N_1 to N_2 , and $\Phi(t)$ is the photon field. Most importantly, γ_s , γ_d γ_a represent three competing, decay pathways, the linear Shockley-Read-Hall (γ_s), quadratic defect mediated (γ_g) and cubic Auger (γ_a) respectively.

Generally, EHP recombination is described by an equation in the form[237]

$$R(n) = An + Bn^2 + Cn^3 + R_{st}N_{ph} \quad (6.2)$$

where the linear term A is associated with non-radiative defect induced recombination (Shockley-Read-Hall) and the quadratic term B is assigned to spontaneous radiative recombination. The band gap luminescence lifetime of ZnO is however, on the nanosecond time scale so spontaneous recombination can be neglected in our femtosecond measurements.[238] Therefore, the quadratic and cubic terms were assigned to the defect mediated electron-hole recombination and defect mediated Auger recombination respectively. Finally, $R_{st}N_{ph}$ represents stimulated radiative recombination that results in the luminescence that is imaged in our microscope.

The coupled rate equations were used to globally fit the extracted transient emission data measured at two different excitation intensities. Figure 6.5 (a) and (b) shows the integrated luminescence dynamics from each region at two different excitation fluences, 18.2 mJ/cm^2 and 11.5 mJ/cm^2 , represented by red and green markers respectively. The fit to the ASE model (blue line) is shown to be in good agreement with the measured luminescence data and reproduces both the temporal shift in the onset of the high and low fluence emission data as well as the more pronounced second maximum observed in region 2. The fitting parameters for each region are shown in Table 1. It should be noted that the fits were also performed at different intensities

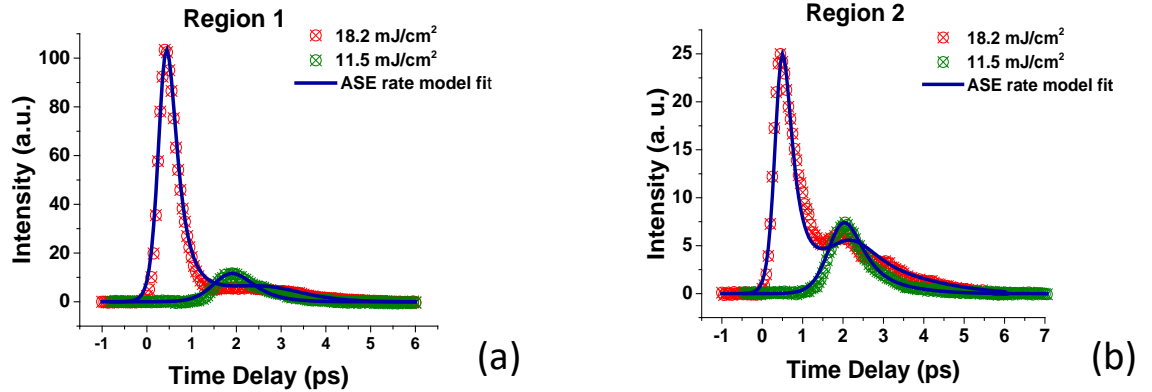


Figure 6.5: (a)-(b) The red and green markers represent the transient dynamics extracted from each region at high (18.2 mJ/cm^2) and low excitation (11.5 mJ/cm^2) fluences respectively. The fit to the ASE model is represented by the blue line.

using the same parameters only varying the carrier density according to the change in fluence.

The Shockley-Read-Hall (SRH) recombination rate term can not be determined in the application of the ASE model to the emission data in this study due to the high charge carrier density. This is discussed in detail below. The second maximum that appears in region 2 is the most marked difference between the two regions. The maxima represent the relaxation oscillations in the emission output from the nanowire which is characteristic of early onset lasing.[57] The non-radiative recombination pathways in the model act to dampen these oscillations. Between the two actively competing pathways the defect mediated rate constant is orders of magnitude larger than the Auger for both regions, suggesting that this pathway is the most prominent loss channel. For region 2 both the defect mediated and Auger rate constants were higher than that of region 1. The defect mediated rate constant for region 2 was approximately 1.7 times larger than region 1. The Auger recombination rate constant increased by a factor of 3.5 along the nanowire from tip (region 1) to base (region2). The larger recombination

rate constants suggest that more damping at region 2 was required to reproduce the observed undulations in the emission data.

The dependence of both the defect mediated and Auger recombination rate constants on carrier density would require that there also be an increase in carrier density generated at regions 2 compared to region 1. The prominent second maximum that occurs in the emission profile of region 2 is in fact indicative of high carrier densities. The fit-generated carrier density for each region at 18.2 mJ/cm^2 shows that there was a three-fold increase in carriers produced in moving along the nanowire from tip to base. Fewer carriers were therefore produced at the tip (region 1) by the same excitation fluence than at the base area (region 2). This trend correlates with the increasing diameter of the nanowire and with newest to oldest crystal growth. Both the stimulated emission rate (B) and the relaxation rate (τ_r) parameters also followed this trend of increase from tip to base while the escape rate (γ_Φ) remained approximately steady.

SRH recombination or trap assisted recombination rate is a measure of the impurities or crystal defects in a semiconductor. The SRH lifetime is therefore dependent on defect density as well as the energy level of these traps.[104] In the application of the ASE model to the measurements it was found that the fits were able to more closely reproduce the measured data without the SRH term. From the good agreement of the fits with the measurements, this would imply that a linear trap-mediated type recombination did not play a significant role in contributing to the dynamics observed at either location on the nanowire. If the calculated carrier densities are considered, then exceeding the Mott density of ZnO could lead to the quadratic and cubic recombination rates, which represent the two-body and three-body recombination pathways respectively, to be more dominant under these conditions and have a greater effect on the dynamics.[239] Higher carrier densities would increasingly favor many-particle recombination processes and the non-radiative nature of these processes would suggest that traps or recombination centers due to defect states are involved.[240]

Table 6.1: ASE Model Fitting Parameters for Global Fit of Luminescence Dynamics from Region 1 and 2

Fit Parameters	Region 1	Region 2
Relaxation time τ_r (ps)	1.99	3.09
Escape time γ_Φ (fs)	7.97	8.87
Stimulated emission rate (B) ($10^{-8} \text{ cm}^3 \text{ s}^{-1}$)	3.45	5.69
Shockley-Read rate γ_s (s^{-1})	0	0
Defect mediated rate constant γ_g ($10^{-10} \text{ cm}^3 \text{ s}^{-1}$)	1.88	3.16
Auger rate constant ($10^{-30} \text{ cm}^6 \text{ s}^{-1}$)	1.89	6.67
Carriers per unit density	4054	13354

6.2.4 The influence of a defect density profile

In order to relate the physical meaning of the values extracted from the model to the transient dynamics at each of the regions on the nanowire, the growth conditions and mechanism behind obtaining a tapered morphology of the nanowire need to be examined. The nanowire in this study is without the gold tip typically observed in VLS grown nanowires.[241] The growth is described by a three-stage growth model. In the initial nucleation phase a supersaturated Zn- Au alloy droplet, formed from Zn vapor dissolving in gold particles, reacts with oxygen to precipitate ZnO below the catalyst droplet as ZnO seeds. This phase is dictated by VLS growth. The ZnO seeds created in the first stage provide new nucleation sites for ZnO vapor in the second stage where both VLS and VS growth mechanisms compete. The catalyst droplet is eventually completely encased and in the third stage only the catalyst-free VS mechanism is possible. The tapered morphology is achieved when the axial and radial growth rates differ. [242] According to Barnard et al. most nanowire cross sections that appear cylindrical are likely dodecagonal upon closer inspection with high-resolution TEM.[243] The size and nature of the sample in this study prevented such crystallographic characterization. ZnO, however, preferentially crystallizes in the hexagonal wurtzite-type structure owing to the fact this structure is slightly lower in energy than the zinc-blend structure with primary cleavage planes ($(10\bar{1}0)$, $(11\bar{2}0)$) and (0001) .[243] If a wurzite crystal structure and dodecagonal morphology is assumed with

fast growing, high surface energy top end facet ((0001)) and much lower surface energy side walls ((10 $\bar{1}$ 0)) and (11 $\bar{2}$ 0)) then the tapered morphology observed in this nanowire, produced by different rates of VS growth on all surfaces, would be energetically feasible.

Nanowires that are both cylindrical (dodecagonal) and have a tapered morphology have been associated with more defect states than hexagonal nanowires with fixed aspect ratios. [244, 245, 246] For the proposed growth model the nanowire base would consist of a ZnO crystal structure assembled by both VLS and VS mechanisms while the tip would be solely VS assembled crystal. Additionally, two different growth environments Ar gas flow (Zn-rich) versus the air (oxygen-rich) are provided during the growth of the nanowire. This would mean that the nanowire could not only exhibit a defect density gradient along its growth length but also that different point defects could dominate at different locations along the length. Defect concentration gradients have previously been reported for ZnO microwires.[247] The spatial distribution of the defects in the nanowire was examined by SEM-cathodoluminescence imaging (supplementary information). The results confirm a disproportionate concentration of defects at the base of nanowire compared to the tip.

The multitude of both computational and spectroscopic studies on the defect states of ZnO, although extensive, often differ when it comes to identifying specific energy levels of point defects. It is therefore difficult to make definitive assignments based on the body of work available especially in the case of defect induced non-radiative transitions which lack a spectroscopic signature. The formation enthalpy can act as an initial starting point to determine the ease with which a particular point defect would form and whether it would be dominant under certain conditions. The formation enthalpy of point defects depends on growth and annealing conditions, either Zn-rich or O-rich environments, and if the defect is charged then the enthalpy will also depend on the Fermi level energy (E_f).[119] Since ZnO is well known to be inherently n-type without intentional doping, formation energies of defects were considered for the Fermi energies $>2\text{eV}$ up to the maximum level at the conduction band minimum (CBM).

The oxygen vacancies (V_o) and zinc interstitial (Zn_i) point defects are frequently cited as the dominant intrinsic defects in ZnO.[195, 248, 119] Under zinc-rich conditions at $E_f = 2.0$ eV to $E_f = 2.8$ eV, V_o followed by Zn_i have the lowest formation energies with V_o being the dominant point defect. Above $E_f = 2.8$ eV and at the CBM reports differ for whether V_o or Zinc vacancies (V_{Zn}) have the lowest formation energy, and is hence the dominant defect.[195, 249] The formation energy of the Zn_i^{2+} resonance for the Fermi energies 2.0 -2.8 eV is cited as ranging from 1.5 eV to approximately 4.8 eV. At the higher end of this range, formation of Zn_i^{2+} becomes energetically unfavorable. At increasingly high defect concentrations, however, interactions between defects become significant and defect complexes are formed.[198, 248] Strong attractive interactions between donor-like defects such as V_o and Zn_i occur and the hybridization (V_o+Zn_i) between electronic orbitals causes a reduction in the formation energy of the system. The hybridization, which is strengthened by the decrease in mutual distance between the pairs, lowers the deep donor state V_o (V_o^*) and raises the shallow donor Zn_i into the conduction band (Zn_i^*).[198, 248]

First-principles theoretical band structure calculations show electronic states due to excess Zn exist below the valence band and above the conduction band facilitating inter defect transitions in excess of 4.0 eV.[198, 248] Figure 6.6 shows the transition schematics for both Zn_i and the hybridized states of the (V_o+Zn_i) complex. Although the large formation enthalpy of the Zn_i point defect makes the probability of its existence smaller at higher Fermi energies, formation of the complex would require higher concentrations of both individual point defects. We therefore propose that the base of the nanowire, which is formed under Zn-rich conditions, would have an abundance of Zn_i point defects in addition to hybridized complex defects. The excess defects would allow for defect induced absorption at the excitation wavelength of 290 nm (Figure 6.6). The enhanced absorption from the base of the nanowire would mean more photons would be absorbed and hence more electron-hole pairs produced at the base compared to the tip with the exposure to the same excitation fluence. This would explain the 3-fold increase in the carrier density for the base region produced

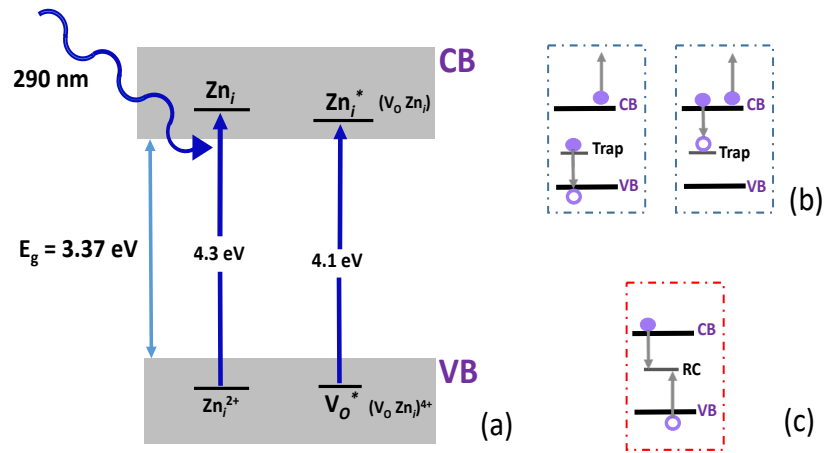


Figure 6.6: (a) Diagram of the energy levels of the intrinsic defects and defect complexes that induce absorption in the base of the nanowire. (b) Schematic of the two non-radiative trap-assisted Auger recombination mechanisms which reduce the intensity of emission at Region 2. (c) Defect mediated recombination mechanisms at a defect state acting as a recombination center (RC).

by the fits compared to the tip of the nanowire. The tip of the nanowire, in contrast to the base, is grown under an oxygen-rich environment. In oxygen-rich conditions reports show V_{Zn} to be consistently dominant at $E_f > 2.0$ eV up to the CBM while the formation energy of both Zn_i and V_o increase by as much as 4 eV each.[248, 195] The prohibitively high increase in formation energy under oxygen rich conditions makes the formation of Zn_i , V_o and the complex of the two defects less likely. The tip of the nanowire would therefore have fewer absorption inducing defects and hence would generate fewer electron-hole pairs and have a lower charge carrier density.

Although large carrier densities are generated at the base of the nanowire, the repercussions of the accompanying higher number of defects are the increased traps that lead to non-radiative emission. This is in addition to the anticipated increase in many-body recombination processes associated with higher carrier densities.[250] The increase in the defect mediated and Auger rate constants produced by the fit along the nanowire from tip to base corresponds with the increase in defect states expected with the growth conditions of the nanowire. These defect states, in particular, deep level defects such as V_o^* act as either traps or recombination centers.[251, 252] Acting as traps, an excess of deep level donor or acceptor defects allow the non-radiative recombination to proceed via the trap-assisted Auger recombination mechanisms illustrated in Figure 6.6(b). In the first scheme an electron from a donor defect transitions non-radiatively to the valence band by giving its energy to an electron in the conduction band. The second scheme an electron in the conduction band recombines with an acceptor defect and the energy is transferred to another electron which is promoted higher in the conduction band. The schematic of the defect mediated recombination mechanism is shown in Figure 6.6(c). The defect state in this case will act as a recombination center and facilitate the recombination of majority and minority carriers. A larger non-radiative recombination occurring at the base of the nanowire due to increased defect levels would ultimately quench the emission from the base of the nanowire compared to the tip as was observed in the measurement.

At a high rate of pumping of non-equilibrium carriers the Auger process typically the predominant non-radiative recombination pathway.[253] In the applied ASE model, however, the quadratic defect mediated recombination rate constant is orders of magnitude larger than the Auger. The non-radiative defect mediated recombination rate, as the leading loss channel, is therefore also a measure of the rate of capture of either electrons and holes at the deep level defect states given by the the equations

$$R_n = C_n N_n n \quad (6.3)$$

$$R_p = C_p N_p p \quad (6.4)$$

Where $C_{\{n,p\}}$ is the electron (hole) capture coefficient, $N_{\{n,p\}}$ is the density of the acceptor or donor trap states and n and p are the electron and hole densities respectively. $C_{\{n,p\}}$ is related to the effective capture cross section $\sigma_{\{n,p\}}$ by the equation $C_{\{n,p\}} = \sigma_{\{n,p\}} \nu_{\{n,p\}}$, where $\nu_{\{n,p\}}$ is the thermal velocity. For bulk ZnO the estimated capture cross sections is reported to be approximately 10^{-15}cm^{-2} , [254] the calculated capture coefficients for electrons and holes were then $6 \times 10^{-8} \text{cm}^3 \text{s}^{-1}$ and $3 \times 10^{-8} \text{cm}^3 \text{s}^{-1}$ respectively. These values are well within the range of previous reports. With the calculated capture coefficients the total defect density ($N_{\{n\}} + N_{\{p\}}$) is calculated at each region on the nanowire. Region 1 had a defect density of $9.05 \times 10^{10} \text{cm}^{-3}$ while region 2 was $1.67 \times 10^{11} \text{cm}^{-3}$. The defect density at the base of the nanowire was approximately twice as large as that of the base. The larger concentration of defect densities at the base of the nanowire is well aligned with the density gradient predictions made from the growth model (vide supra).

6.3 Experimental methods

6.3.1 Single ZnO nanowire samples

The ZnO nanowires were prepared using a gold-catalyzed vapor-liquid-solid (VLS) and vapor-solid (VS) technique previously reported.[150, 255] Briefly, ZnO

nanowires were epitaxially grown on fused silica wafers spin coated with 10 nm gold (Cresington 308R coating system). Ar gas was used to transport Zn vapor produced by a carbothermal reaction to the prepared wafer for 2 hours then air was used as the source of oxygen for 3 hours. This changed the growth conditions from Zn-rich to Zinc-poor (oxygen-rich) and leads to a gradient in defect states. The as-grown bulk samples were characterized by scanning electron microscopy (SEM) measurements (Hitachi S5700) and found to be of both hexagonal cross section and round cylindrical tapered nanowire morphologies. The ZnO nanowires ranged from 300-800 nm in diameter and grew to approximately 50 μm in length. Single ZnO nanowires were isolated for measurement by drop casting nanowires suspended in acetone onto silicon substrates. Single nanowire samples were measured first with the Kerr-gated microscope before characterization via SEM.

6.3.2 Computational Techniques

Finite-difference time-domain calculations were performed using the commercial software Optiwave OPTIFDTD. A 3D model of the nanowire measured in this study was constructed from the energy-dependent refractive indices of ZnO. The parameters were set to mimic the experimental conditions as closely as possible. Details of the computational domain and selected calculation parameters are provided in section [6.4](#).

6.3.3 SEM-CL measurements

The SEM-CL measurements were conducted in a Tescan XEIA FEG SEM. A constant e-beam of 30 kV and 0.3 nA was used at each measurement location. A $2 \times 2 \mu\text{m}$ location was selected at either end of the nanowire and measurements were performed for no more than 10 minutes at each region. A rainbow CL detector, which enables simultaneous panchromatic and colour CL imaging of a sample, was used to observe the blue and green channels corresponding to bandedge and defect emission respectively.

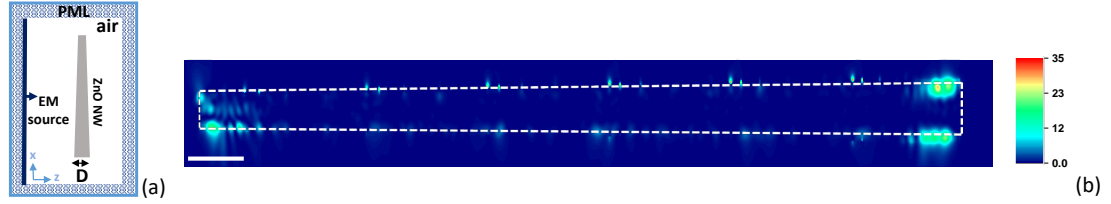


Figure 6.7: (a) FDTD computational domain showing the propagation direction of the Gaussian pulse source perpendicular to the long axis of the nanowire. (b) Electrical field intensity distribution of the long axis cross-section of the nanowire (Scale represents $1 \mu\text{m}$).

6.4 Additional characterization

6.4.1 Finite Difference Time Domain Calculations

Finite-difference time-domain (FDTD) calculations were employed as a check of the spatial distribution of the optical field for an ideal ZnO nanowire under the same excitation conditions as the ultrafast measurements conducted. The optical field around a ZnO nanowire with a circular cross-section, tapered morphology and the same dimensions as the nanowire measured in this investigation was simulated. Figure 6.7 (a) shows a 2D depiction of the 3D computational environment in which calculations were performed. A sine-modulated Gaussian pulse source (290 nm) was used and allowed to propagate perpendicular to the long axis of the nanowire. A 2D observation area selected from the 3D simulation is shown in Figure 6.7(b) at the maximum amplitude of the pulsed excitation. The figure shows the longitudinal cross-section of the full nanowire and the spatial intensity distribution along the nanowire length. Although the transverse modes supported by the circular cross-section are expected to dominate the calculated resonances, due to the orientation of the excitation source propagation, the field distribution view along the long axis of the nanowire is important. It highlights both the periodic intensity modulation along the nanowire length as well as the difference in field intensity at the ends of the nanowire compared to the middle.

The oscillations in field intensity seen in the middle of the nanowire have previously been attributed to Fabry- Perot (FP) and whispering gallery (WG) modes which are both dependent on the diameter of the nanowire.[256, 257] The change in diameter with the tapering of the nanowire causes the excitation wavelength to go in and out of resonance as the light travels along the length of the nanowire.[258] FP modes are not expected to contribute significantly in this case because the system was modeled with a circular rather than hexagonal geometry so there are no flat reflective side walls. The higher field intensity distribution at the ends of the nanowire compared to the middle matches the observed emission pattern from the measurements. The model further shows that the localized field intensity at the ends of the nanowire, usually attributed to lasing in nanowires, can occur outside of lasing conditions in the early time after peak excitation. The pattern of end facet emission commonly observed from an excited nanowire may therefore not be definitively characteristic of lasing.

6.4.2 SEM-cathodoluminescence measurements

SEM- cathodoluminescence (SEM-CL) imaging measurements were performed on the nanowire measured in this study. Although SEM-CL is not directly quantitative, the spatial distribution of the characteristic UV and green defect emission is informative to the study. The overall intensity at the base of the nanowire for both the green and blue channels is higher than at the tip and neither tip nor base exhibited a high intensity at the end facets as is observed in the fluorescence measurements. It should be noted that differences in SEM-CL images and ultrafast micrographs were expected as the excitation mechanisms, electron bombardment versus femtosecond photon pulses respectively, would result in different emission mechanisms. The former mechanism not readily facilitating amplification or early onset lasing like the latter would.

The tip showed relatively uniform intensity for both channels while the base showed peak intensity at approximately $1 \mu m$ away from the end facet. This region appears slightly broader in diameter as a result of lateral growth during the synthesis process. A smaller region, indicated by the white box, near the end of the tip and the

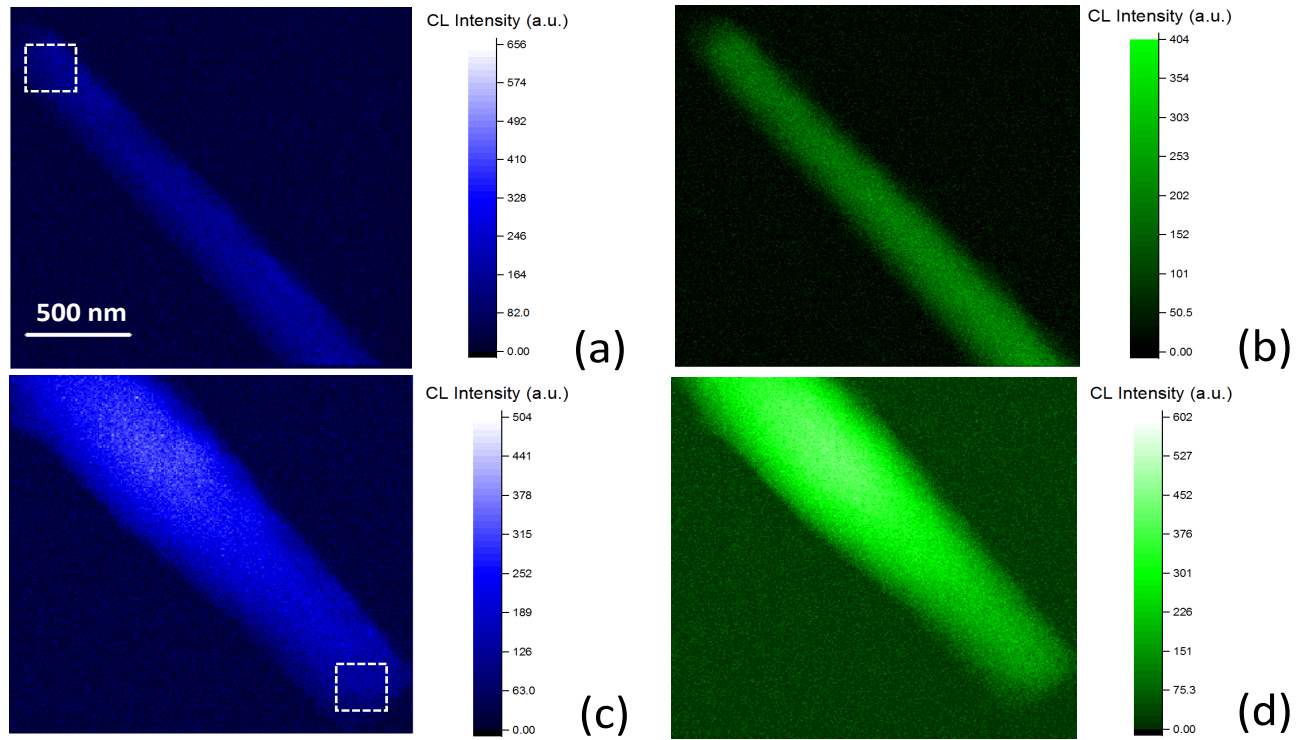


Figure 6.8: (a)-(d) SEM-CL images of the tip and base of the nanowire for band-edge emission (blue) and visible emission (green) respectively. White box represents region where integrated intensity was measured for each region.

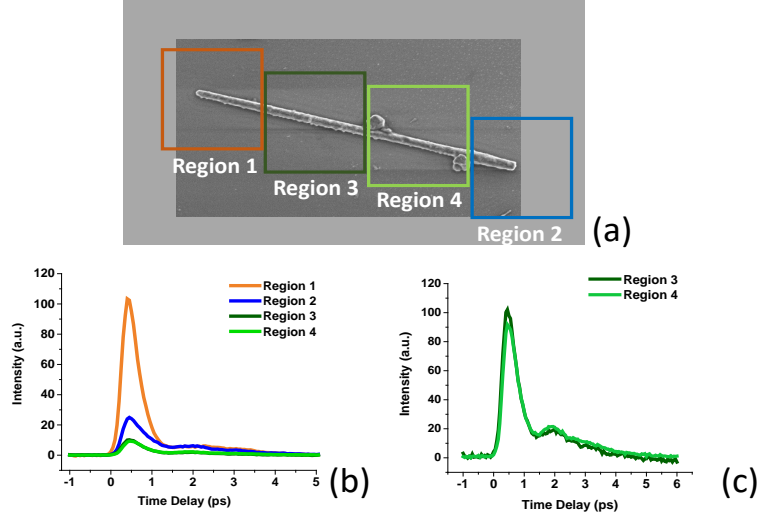


Figure 6.9: (a) SEM image of the nanowire and the location of all regions (Region 1-4) of interest. (b) Transient extracted from all regions at a fluence of 18.2 mJ/cm^2 (b) Transients extracted from region 3 and 4 at a fluence of 18.2 mJ/cm^2 .

base of the nanowire was selected and the integrated intensity calculated to provide a quasi-quantitative comparison of the channels. There was an approximately 0.98:1 ratio in integrated intensity for the green to blue channel for the tip. For the base, the integrated intensity ratio for the selected region was 1.14:1 for the green vs blue channel.

In the blue channel the tip to base ratio was 1.1:1 while the in the green channel the ratio was 0.94:1. The SEM-CL images show that the green channel intensity, defect emission intensity, was higher for the selected area at the base of the nanowire compared to the tip. These results agree with the growth model as well the trend of the calculated defect density.

6.4.3 Middle region

The middle region of the nanowire was separated into two regions (region 3 and 4). Figure 6.9 shows the position of region 3 and 4 in relation to the end facet regions. Transients were extracted from the middle portion of the nanowire where the loose

debris particles were located. The emission intensity from both middle regions of the nanowire were approximately half the intensity measured at the base (Region 2) and approximately 10 times less than the intensity at the tip (Region 1)(Figure 6.9(b)). Figure 6.9(c) highlights the detail in the dynamics at region 3 and 4. In moving from the tip (region 1) to the base (region 2) features of the transients gradually changed to match that of the emission dynamics of the end facet that was in proximity. Region 3 shows a slightly higher peak intensity than region 4 and was closer to region 1 which had the highest intensity. Region 4 had a higher second maximum than region 3 and is closer to region 2 which had the more prominent second maximum. The progressive change in dynamics from tip to base as shown in the transients extracted from the middle delineate the changes occurring in the nanowire morphology and density profile.

6.5 Conclusion

We have developed an ultrafast technique capable of detecting defect density changes in a single nanowires through changes in the transient fluorescence. The method is powerful tool for the quantitative characterization of single nanostructures that removes the restriction of contacts. Additional information about the ultrafast recombination processes occurring in nanostructures can also be extracted. The linear Shockley-Read, quadratic defect mediated and the cubic Auger recombination constants can also be extracted from the ASE model. These rate constants provide a description of the transient emission profile as well as help correlate the observed optical response to structural changes in the nanostructures.

Chapter 7

SUMMARY

The charge carrier dynamics of individual $\text{CdS}_x\text{Se}_{1-x}$ and ZnO nanowires were measured using a femtosecond Kerr-gated microscope system. The objective of this study was to develop a contact-less method to probe the early time dynamics of single nanostructures, specifically to gain insight into factors that influence charge carrier mobility in single ZnO nanowires.

Measurements were initially conducted in the visible detection range on single $\text{CdS}_x\text{Se}_{1-x}$ nanowires. It was demonstrated that position-dependent dynamics along a single nanowire excited under the same conditions can be detected by the setup. The regions of high localized intensity only occurred after a certain threshold was exceeded as is characteristic of ASE. The ASE dynamics from three regions along the nanowire were compared. Two of the three regions showed a second maximum in the transient data indicative of higher carrier densities. Since the excitation spot size was much larger than the area measured and had a Gaussian intensity profile, it was assumed that the excitation fluence was constant along the measured length of the nanowire. Color space measurements along the nanowire revealed that emission wavelength changed by less than 3% and hence the composition remained relatively consistent. There were also no significant changes in the growth direction or morphology in the measured region hence variation in the dynamics must be a result of changes in the scattering rates at the different locations.

As very steady measurement data was required to obtain fits to the ASE model, additional measurements were conducted on a separate nanowire that produced emission signal with higher signal-to-noise ratio. Again the position-dependent ASE dynamics were observed along the length of the nanowire. From the fits to the ASE

model, the extracted non-geminate recombination rate was the leading de-excitation pathway. Assuming the recombination is diffusion limited in the $\text{CdS}_x\text{Se}_{1-x}$ nanowire, then the charge carrier mobility can be calculated from non-geminate recombination rate. The calculated value ($0.2 \text{ cm}^2/\text{Vs}$) was orders of magnitude lower than that of comparable literature values. These results suggested that due to the large carrier densities generated in the nanowire, recombination may enter the non-diffusion limited regime.

Conversion to UV detection range resulted in a maximum temporal resolution of 85 fs with a 0.15 mm thick fused silica Kerr medium. The YAG Kerr medium was ultimately chosen as the best compromise between temporal resolution and gating efficiency. In the UV detection range the larger transmission through the gate afforded more nanowires to be measured as the gating efficiency increased 4 times that when the setup was configured for the visible detection range. Phenomenon such as band-gap renormalization was observed in the transient spectra. Ultrafast measurement of a single tapered ZnO nanowire showed differences in the temporal dynamics from the emission from the tip and the base. Fits to the ASE model revealed that the Shockley-Read-Hall rate had no significant influence on the dynamics and so was neglected. The quadratic de-excitation pathway, the two-body defect mediated recombination rate, dominated. From this rate a defect density was calculated for either end of the nanowire and the middle region. The defect density gradient is expected to have been established by the the change in growth conditions. The Kerr-gated microscope is therefore a new contact-less method for quantifying defect density in single nanowires.

BIBLIOGRAPHY

- [1] N. P. Dasgupta, J. Sun, C. Liu, S. Brittman, S. C. Andrews, J. Lim, H. Gao, R. Yan, and P. Yang. 25th anniversary article: semiconductor nanowires—synthesis, characterization, and applications. *Advanced Materials*, 26(14):2137–2184, 2014.
- [2] R. P. Prasankumar, P. C. Upadhyaya, and A. J. Taylor. Ultrafast carrier dynamics in semiconductor nanowires. *physica status solidi (b)*, 246(9):1973–1995, 2009.
- [3] A. Pan, W. Zhou, E. S. P. Leong, R. Liu, A. H. Chin, B. Zou, and C. Z. Ning. Continuous alloy-composition spatial grading and superbroad wavelength-tunable nanowire lasers on a single chip. *Nano Letters*, 25(2):784–788, 2009.
- [4] R. Agarwal and C.M. Lieber. Semiconductor nanowires: optics and optoelectronics. *Applied Physics A*, 85(3):209, Sep 2006.
- [5] D. Caselli, Z. Liu, D. Shelhammer, and C.-Z. Ning. Composition-graded nanowire solar cells fabricated in a single process for spectrum-splitting photovoltaic systems. *Nano letters*, 14(10):5772–5779, 2014.
- [6] B. Oregan and M. Grätzel. A low-cost, high-efficiency solar cell based on dye-sensitized. *nature*, 353(6346):737–740, 1991.
- [7] A. Hagfeldt, G. Boschloo, L. Sun, L. Kloo, and H. Pettersson. Dye-sensitized solar cells. *Chemical Reviews*, 110(11):6595–6663, 2010. PMID: 20831177.
- [8] J. Gong, K. Sumathy, Q. Qiao, and Z. Zhou. Review on dye-sensitized solar cells (DSSCs): Advanced techniques and research trends. *Renewable and Sustainable Energy Reviews*, 68, Part 1:234 – 246, 2017.
- [9] M. Freitag, J. Teuscher, Y. Saygili, X. Zhang, F. Giordano, P. Liska, J. Hua, S. M. Zakeeruddin, J.-E. Moser, M. Grätzel, and A. Hagfeldt. Dye-sensitized solar cells for efficient power generation under ambient lighting. *Nature Photonics*, 2017.
- [10] J. Gong, J. Liang, and K. Sumathy. Review on dye-sensitized solar cells (DSSCs): Fundamental concepts and novel materials. *Renewable and Sustainable Energy Reviews*, 16(8):5848 – 5860, 2012.

- [11] G. Richhariya, A. Kumar, P. Tekasakul, and B. Gupta. Natural dyes for dye sensitized solar cell: A review. *Renewable and Sustainable Energy Reviews*, 69:705 – 718, 2017.
- [12] S. Mathew, A. Yella, P. Gao, R. Humphry-Baker, B. F. E. Curchod, N. Ashari-Astani, I. Tavernelli, U. Rothlisberger, M. D. K. Nazeeruddin, and M. Grätzel. Dye-sensitized solar cells with 13% efficiency achieved through the molecular engineering of porphyrin sensitizers. *Nature chemistry*, 6(3):242–247, 2014.
- [13] U. Bach, D. Lupo, P. Comte, J. E. Moser, F. Weissörtel, J. Salbeck, H. Spreitzer, and M. Grätzel. Solid-state dye-sensitized mesoporous TiO₂ solar cells with high photon-to-electron conversion efficiencies. *Nature*, 395(6702):583–585, 1998.
- [14] J. Wu, Z. Lan, J. Lin, M. Huang, Y. Huang, L. Fan, and G. Luo. Electrolytes in dye-sensitized solar cells. *Chemical Reviews*, 115(5):2136–2173, 2015. PMID: 25629644.
- [15] M. S. Suait, M. Y. A. Rahman, and A. Ahmad. Review on polymer electrolyte in dye-sensitized solar cells (DSSCs). *Solar Energy*, 115:452 – 470, 2015.
- [16] S. H. Ko, D. Lee, H. W. Kang, K. H. Nam, J. Y. Yeo, S. J. Hong, C. P. Grigoriopoulos, and H. J. Sung. Nanoforest of hydrothermally grown hierarchical ZnO nanowires for a high efficiency dye-sensitized solar cell. *Nano letters*, 11(2):666–671, 2011.
- [17] O. Lupan, V. M. Gurin, I. M. Tiginyanu, V. V. Ursaki, L. Chow, H. Heinrich, and T. Pauport. Well-aligned arrays of vertically oriented ZnO nanowires electrodeposited on ITO-coated glass and their integration in dye sensitized solar cells. *Journal of Photochemistry and Photobiology A: Chemistry*, 211(1):65 – 73, 2010.
- [18] S. Gubbala, V. Chakrapani, V. Kumar, and M. K. Sunkara. Band-edge engineered hybrid structures for dye-sensitized solar cells based on SnO₂ nanowires. *Advanced Functional Materials*, 18(16):2411–2418, 2008.
- [19] J. M. Kroon, N. J. Bakker, H. J. P. Smit, P. Liska, K. R. Thampi, P. Wang, S. M. Zakeeruddin, M. Grätzel, A. Hinsch, S. Hore, U. Würfel, R. Sastrawan, J. R. Durrant, E. Palomares, H. Pettersson, T. Gruszecki, J. Walter, K. Skupien, and G. E. Tulloch. Nanocrystalline dye-sensitized solar cells having maximum performance. *Progress in Photovoltaics: Research and Applications*, 15(1):1–18, 2007.
- [20] J. B. Baxter and E. S. Aydil. Nanowire-based dye-sensitized solar cells. *Applied Physics Letters*, 86(5):053114, 2005.
- [21] Q. Peng and Y. Qin. ZnO nanowires and their application for solar cells. In *Nanowires-Implementations and Applications*. InTech, 2011.

- [22] C. Jagadish and S. J. Pearton. *Zinc oxide bulk, thin films and nanostructures: processing, properties, and applications*. Elsevier, 2011.
- [23] D.C. Look, D.C. Reynolds, J.R. Sizelove, R.L. Jones, C.W. Litton, G. Cantwell, and W.C. Harsch. Electrical properties of bulk ZnO. *Solid State Communications*, 105(6):399 – 401, 1998.
- [24] Z. M. Jarzebski and J. P. Marton. Physical properties of SnO₂ materials II. electrical properties. *Journal of the electrochemical Society*, 123(9):299C–310C, 1976.
- [25] E. Yagi, R. R. Hasiguti, and M. Aono. Electronic conduction above 4 K of slightly reduced oxygen-deficient rutile TiO_{2-x}. *Phys. Rev. B*, 54:7945–7956, Sep 1996.
- [26] X. Duan and C. M. Lieber. General synthesis of compound semiconductor nanowires. *Advanced Materials*, 12(4):298–302, 2000.
- [27] Y. Wu, H. Yan, M. Huang, B. Messer, J. H. Song, and P. Yang. Inorganic semiconductor nanowires: Rational growth, assembly, and novel properties. *Chemistry A European Journal*, 8(6):1260–1268, 2002.
- [28] H. J. Joyce, J. L. Boland, C. L. Davies, S. A. Baig, and M. B. Johnston. A review of the electrical properties of semiconductor nanowires: insights gained from terahertz conductivity spectroscopy. *Semiconductor Science and Technology*, 31(10):103003, 2016.
- [29] K. Storm, F. Halvardsson, M. Heurlin, D. Lindgren, A. Gustafsson, P. M. Wu, B. Monemar, and L. Samuelson. Spatially resolved hall effect measurement in a single semiconductor nanowire. *Nature nanotechnology*, 7(11):718–722, 2012.
- [30] J. W. W. van Tilburg, R. E. Algra, W. G. G. Immink, M. Verheijen, E. P. A. M. Bakkers, and L. P. Kouwenhoven. Surface passivated InAs/InP core/shell nanowires. *Semiconductor Science and Technology*, 25(2):024011, 2010.
- [31] S. A. Dayeh, C. Soci, P. K. L. Yu, E. T. Yu, and D. Wang. Transport properties of InAs nanowire field effect transistors: The effects of surface states. *Journal of Vacuum Science & Technology B: Microelectronics and Nanometer Structures Processing, Measurement, and Phenomena*, 25(4):1432–1436, 2007.
- [32] E. Koren, Y. Rosenwaks, J. E. Allen, E. R. Hemesath, and L. J. Lauhon. Nonuniform doping distribution along silicon nanowires measured by Kelvin probe force microscopy and scanning photocurrent microscopy. *Applied Physics Letters*, 95(9):092105, 2009.
- [33] M. A. Seo, J. Yoo, S. A. Dayeh, S. T. Picraux, A. J. Taylor, and R. P. Prasankumar. Mapping carrier diffusion in single silicon coreshell nanowires with ultrafast optical microscopy. *Nano Letters*, 12(12):6334–6338, 2012. PMID: 23130749.

- [34] L. Huang and J.-X. Cheng. Nonlinear optical microscopy of single nanostructures. *Annual Review of Materials Research*, 43:213–236, 2013.
- [35] P. Piotrowiak, L. Huang, and L. Gundlach. *Ultrafast Optical Imaging and Microspectroscopy*. 2013.
- [36] B. P. Mehl, J. R. Kirschbrown, M. M. Gabriel, R. L. House, and J. M. Papanikolas. Pumpprobe microscopy: Spatially resolved carrier dynamics in ZnO rods and the influence of optical cavity resonator modes. *The Journal of Physical Chemistry B*, 117(16):4390–4398, 2013. PMID: 23092237.
- [37] E. M. Grumstrup, M. M. Gabriel, E. E.M. Cating, E. M. Van Goethem, and J. M. Papanikolas. Pumpprobe microscopy: Visualization and spectroscopy of ultrafast dynamics at the nanoscale. *Chemical Physics*, 458:30 – 40, 2015.
- [38] M. M. Gabriel, J. R. Kirschbrown, J. D. Christesen, C. W. Pinion, D. F. Zigler, E. M. Grumstrup, B. P. Mehl, E. E. M. Cating, J. F. Cahoon, and J. M. Papanikolas. Direct imaging of free carrier and trap carrier motion in silicon nanowires by spatially-separated femtosecond pumpprobe microscopy. *Nano Letters*, 13(3):1336–1340, 2013. PMID: 23421654.
- [39] K. Suhling, P. M. W. French, and D. Phillips. Time-resolved fluorescence microscopy. *Photochemical & Photobiological Sciences*, 4(1):13–22, 2005.
- [40] S. Arzhantsev and M. Maroncelli. Design and characterization of a femtosecond fluorescence spectrometer based on optical Kerr gating. *Applied Spectroscopy*, 59:206–220, 1875.
- [41] B. Schmidt, S. Laimgruber, W. Zinth, and P. Gilch. A broadband Kerr shutter for femtosecond fluorescence spectroscopy. *Applied Physics B*, 76(8):809–814, Jul 2003.
- [42] I. Dmitruk, Y. Shynkarenko, A. Dmytruk, D. Aleksiuk, V. Kadan, P. Korenyuk, N. Zubriline, and I. Blonskiy. Efficiency estimates and practical aspects of an optical kerr gate for time-resolved luminescence spectroscopy. *Methods and Applications in Fluorescence*, 4(4):044007, 2016.
- [43] R. Nakamura and Y. Kanematsu. Femtosecond spectral snapshots based on electronic optical kerr effect. *Review of scientific instruments*, 75(3):636–644, 2004.
- [44] K. Appavoo and M. Y. Sfeir. Enhanced broadband ultrafast detection of ultraviolet emission using optical kerr gating. *Review of Scientific Instruments*, 85(5):055114, 2014.

- [45] K. Appavoo, M. Liu, and M. Y. Sfeir. Role of size and defects in ultrafast broadband emission dynamics of ZnO nanostructures. *Applied Physics Letters*, 104(13):133101, 2014.
- [46] T. Fujino, T. Fujima, and T. Tahara. Picosecond time-resolved imaging by non-scanning fluorescence kerr gate microscope. *Applied Physics Letters*, 87(13):131105, 2005.
- [47] H.-S. Shim, J.-H. Seo, N.-S. Han, S.-M. Park, Y.-R. Sohn, C.-K. Kim, and J.-K. Song. Amplified spontaneous emission of GaN nanorods. *Bulletin of the Korean Chemical Society*, 33:1075–1077, 2012.
- [48] P. Yang, G. Wirnsberger, H. C. Huang, S. R. Cordero, M. D. McGehee, B. Scott, T. Deng, G. M. Whitesides, B. F. Chmelka, S. K. Buratto, and G. D. Stucky. Mirrorless lasing from mesostructured waveguides patterned by soft lithography. *Science*, 287:465–467, 2000.
- [49] M. J. F. Empizo, K. Yamanoi, A. B. Santos-Putungan, R. Arita, Y. Minami, M. V. Luong, T. Shimizu, E. S. Estacio, A. S. Somintac, A. A. Salvador, R. V. Sarmago, and N. Sarukura. Blue-shifted and picosecond amplified UV emission from aqueous chemical grown zno microrods. *Optical Materials*, 48:179 – 184, 2015.
- [50] J. C. Johnson, H. Yan, P. Yang, and R. J. Saykally. Optical cavity effects in ZnO nanowire lasers and waveguides. *The Journal of Physical Chemistry B*, 107(34):8816–8828, 2003.
- [51] G.P. Zhu, C.X. Xu, J. Zhu, X. Li, K. Zheng, J.P. Liu, C.G. Lu, and Y.P. Cui. Characteristics of ultraviolet amplified spontaneous emission from zinc oxide nanowires. *Optical Materials*, 31(2):181 – 183, 2008.
- [52] G. I. Peters and L. Allen. Amplified spontaneous emission i. the threshold condition. *Journal of Physics A: General Physics*, 4(2):238, 1971.
- [53] H. Gao, A. Fu, Sean C. A., and P. Yang. Cleaved-coupled nanowire lasers. *Proceedings of the National Academy of Sciences*, 110(3):865–869, 2013.
- [54] R.-M. Ma, L. Wei, X.-L. and Dai, S.-F. Liu, T. Chen, S. Yue, Z. Li, Q. Chen, and G. G. Qin. Light coupling and modulation in coupled nanowire ring-fabry-prot cavity. *Nano Letters*, 9(7):2697–2703, 2009. PMID: 19534464.
- [55] R. F. Oulton, V. J. Sorger, R.-M. Zentgraf, T. and Ma, C. Gladden, L. Dai, G. Bartal, and X. Zhang. Plasmon lasers at deep subwavelength scale. *Nature*, 461(7264):629–632, 2009.

- [56] H. Yan, J. Johnson, M. Law, R. He, K. Knutsen, J. R. McKinney, J. Pham, R. Saykally, and P. Yang. ZnO nanoribbon microcavity lasers. *Advanced Materials*, 15(22):1907–1911, 2003.
- [57] M. A. Zimmler, J. Bao, F. Capasso, S. Müller, and C. Ronning. Laser action in nanowires: Observation of the transition from amplified spontaneous emission to laser oscillation. *Applied Physics Letters*, 93:051101, 2008.
- [58] H. Maeda and A. Yariv. Narrowing and rebroadening of amplified spontaneous emission in high gain laser media. *Physics Letters A*, 43(4):383–385, 1973.
- [59] L. Gundlach and P. Piotrowiak. Ultrafast spatially resolved carrier dynamics in single CdSSe nanobelts. *The Journal of Physical Chemistry C*, 113(28):12162–12166, 2009.
- [60] Yasuhiro Y. and Yoshihiko K. Determination of electron and hole lifetimes of rutile and anatase tio2 single crystals. *Applied Physics Letters*, 101(13):133907, 2012.
- [61] O. Bierwagen, T. Nagata, M. E. White, M.-Y. Tsai, and J. S. Speck. Electron transport in semiconducting sno2: Intentional bulk donors and acceptors, the interface, and the surface. *Journal of Materials Research*, 27(17):2232–2236, 2012.
- [62] Z. Fan and J. G. Lu. Electrical properties of zno nanowire field effect transistors characterized with scanning probes. *Applied Physics Letters*, 86(3):032111, 2005.
- [63] J. Mort. Geminate and non-geminate recombination in amorphous semiconductors. *Le Journal de Physique Colloques*, 42(C4):C4–433, 1981.
- [64] J. Kerr. A new relation between electricity and light: Dielectrified media birefringent. *Philosophical Magazine Series 4*, 50(332):337–348, 1875.
- [65] J. Kerr. A new relation between electricity and light: Dielectrified media birefringent (second paper). *Philosophical Magazine Series 4*, 50(333):446–458, 1875.
- [66] P. D. Maker, R. W. Terhune, and C. M. Savage. Intensity-dependent changes in the refractive index of liquids. *Physical Review Letters*, 16(0):832–832, May 1966.
- [67] R. Torre. *Time-resolved spectroscopy in complex liquids*. New York, Springer, 2008.
- [68] R. W. Boyd. *Nonlinear optics*. Burlington, MA: Academic Press, 2008.
- [69] W. Wang, C. Wang, J. Liu, and J. Tan. Wide-spectrum microscope with a long working distance aspherical objective based on obscuration constraint. *Sensors*, 16(11), 2016.

- [70] Igor A. Artyukov. Schwarzschild objective and similar two-mirror systems. *Proc. SPIE*, 8678:86780A–86780A–6, 2012.
- [71] K. Schwarzschild. Untersuchungen zur geometrischen Optik II. *Astronomische Mitteilungen der Universitaets-Sternwarte zu Goettingen*, 10, 1905.
- [72] M. J. Riedl. *Optical Design Fundamentals for Infrared Systems*. Bellingham, Wash: SPIE Press, 2001.
- [73] W. H. Steel. The design of reflecting microscope objectives. *Australian Journal of Scientific Research A Physical Sciences*, 4, 1951.
- [74] R. Salzer and H. W. Siesler. *Infrared and Raman Spectroscopic Imaging*. Weinheim: Wiley-VCH, 2014.
- [75] Y. L. Kim, J. H. Jung, K. H. Kim, H. S. Yoon, M. S. Song, S. H. Bae, and Y. Kim. The growth and optical properties of CdSSenanosheets. *Nanotechnology*, 20(9):095605, Jun 2009.
- [76] Y.-J. Choi, I.-S. Hwang, J.-H. Park, S. Nahm, and J.-G. Park. Band gap modulation in $\text{CdS}_x\text{Se}_{1-x}$ nanowires synthesized by a pulsed laser ablation with the Au catalyst. *Nanotechnology*, 17(15):3775, 2006.
- [77] A. Pan, H. Yang, R. Yu, and B. Zou. Fabrication and photoluminescence of high-quality ternary CdSSe nanowires and nanoribbons. *Nanotechnology*, 17(17):3775, 2006.
- [78] G. Li, Y. Jiang, Y. Wang, C. Wang, Y. Sheng, J. Jie, J. A. Zapien, W. Zhang, and S.-T. Lee. Synthesis of $\text{CdS}_x\text{Se}_{1-x}$ with uniform and controllable compositions via sulfurization optical and electronic properties studies. *The Journal of Physical Chemistry C*, 17(39):17183–17188, 2009.
- [79] X. Duan, Y. Huang, R. Agarwal, and C. M. Lieber. Single-nanowire electrically driven lasers. *Nature*, 421(6920):241–245, 2003.
- [80] Y. K. Liu, J. A. Zapien, Y.Y. Shan, H. Tang, C. S. Lee, and S. T. Lee. Wavelength-tunable lasing in single-crystal $\text{CdS}_{x-1}\text{CdSe}_x$ nanoribbons. *Nanotechnology*, 18(36):365606, 2007.
- [81] L. Li, H. Lu, Z. Yang, L. Tong, Y. Bando, and D. Golberg. Bandgap-graded $\text{CdS}_x\text{Se}_{1-x}$ nanowires for high-performance field-effect transistors and solar cells. *Advanced Materials*, 25(8):1109–1113, 2013.
- [82] M. A. Hossain, J. R. Jennings, N. Mathews, and Q. Wang. Band engineered ternary solid solution $\text{CdS}_x\text{Se}_{1-x}$ -sensitized mesoscopic TiO_2 solar cells. *Physical Chemistry Chemical Physics*, 14(19):7154–7161, 2012.

- [83] Y. Lu, F. Gu, C. Meng, H. Yu, Y. Ma, W. Fang, and L. Tong. Multicolour laser from a single bandgap-graded CdSSe alloy nanoribbon. *Optics Express*, 21(19):22314–22319, 2013.
- [84] R. S. Wagner and W. C. Ellis. Vapor - liquid solid mechanism of single crystal growth. *Applied Physics Letters*, 4(3):89–90, 1964.
- [85] E.I. Givargizov. Fundamental aspects of vls growth. *Journal of Crystal Growth*, 31:20 – 30, 1975.
- [86] B. Eisenhawer, V. Sivakov, and F. Christiansen, S. and Falk. A time-resolved numerical study of the vaporliquid-solid growth kinetics describing the initial nucleation phase as well as pulsed deposition processes. *Nano Letters*, 13(3):873–883, 2013.
- [87] Y. Zhang, M. K. Ram, E. K. Stefanakos, and D. Y. Goswami. Synthesis, characterization, and applications of ZnO nanowires. *Journal of Materials*, 2012:20:1–20:22, 2012.
- [88] Steven M. R., Stephen H. D., Scott A. N., Alexander A. G., Peter W. V., and M. W. Steady growth of nanowires via the vapor-liquid-solid method. *Journal of Applied Physics*, 102(3):034304, 2007.
- [89] J. C. Blake, P. S. Eldridge, and L. Gundlach. Spatial variation in carrier dynamics along a single CdSSe nanowire. *Chemical Physics*, 442:128 – 131, 2014. Papers from the 11th International Conference on Femtochemistry (FEMTO11) that took place at The Technical University of Denmark (DTU), Copenhagen.
- [90] E Fred Schubert, Thomas Gessmann, and Jong Kyu Kim. *Light emitting diodes*. Wiley Online Library, 2005.
- [91] H. S. Fairman, M. H. Brill, and H. Hemmendinger. How the CIE 1931 colormatching functions were derived from wrightguild data. *Color Research and Application*, 22(1):11–23, 1997.
- [92] T. Smith and J. Guild. The C.I.E. colorimetric standards and their use. *Transactions of the Optical Society*, 33(3):73, 1931.
- [93] *Commission internationale de l'éclairage proceedings, 1931*. Cambridge: Cambridge University Press, 1932.
- [94] W. D. Wright. A re-determination of the trichromatic coefficients of the spectral colours. *Transactions of the Optical Society*, 30(4):141, 1929.
- [95] A. Pan, H. Yang, R. Liu, R. Yu, B. Zou, and Z. Wang. Color-tunable photoluminescence of alloyed CdS_xSe_{1-x} nanobelts. *Journal of the American Chemical Society*, 127:15692–15693, 2005.

- [96] RE Halsted, M Aven, and HD Coghill. Fluorescent emission spectra in II–VI compounds. *Journal of The Electrochemical Society*, 112(2):177–181, 1965.
- [97] R. K. Ahrenkiel, B. M. Keyes, and D. J. Dunlavy. Intensity-dependent minority-carrier lifetime in III-V semiconductors due to saturation of recombination centers. *Journal of applied physics*, 70(1):225–231, 1991.
- [98] H. W. Liu, J. P. Lu, H. M. Fan, C. H. Sow, S. H. Tang, and X. H. Zhang. Temperature and composition dependence of photoluminescence dynamics in $\text{CdS}_x\text{CdSe}_{x-1}$ nanobelts. *Journal of Applied Physics*, 111(7):073112, 2012.
- [99] P. S. Eldridge, J. C. Blake, and L. Gundlach. Ultrafast probe of carrier diffusion and nongeminate processes in a single CdSSe nanowire. *Journal of Spectroscopy*, 2015, 2015.
- [100] F. Vietmeyer, P. A. Frantsuzov, B. Janko, and M. Kuno. Carrier recombination dynamics in individual CdSe nanowires. *Physical Review B*, 83(11):115319, 2011.
- [101] R. S. Mane and C. D. Lokhande. Studies on chemically deposited cadmium sulphoselenide (CdSSe) films. *Thin Solid Films*, 304(1-2):56–60, 1997.
- [102] H. M. Gibbs, P. Mandel, N. Peyghambarian, and S. D. Smith. *Optical Bistability III: Proceedings of the Topical Meeting, Tucson, Arizona, Dezember 2–4, 1985*, volume 8. Springer Science & Business Media, 2012.
- [103] T Amand, J Collet, and BS Razbirin. Exciton dynamics in highly excited CdSe studied by picosecond gain-absorption spectroscopy. *Physical Review B*, 34(4):2718, 1986.
- [104] W. Shockley and W.T. Read. Statistics of the recombination of holes and electrons. *Physical Review*, 87(5):835–842, 1952.
- [105] R. N. Hall. Electron-hole recombination in germanium. *Physical review*, 87(2):387, 1952.
- [106] J. Lu, H. Liu, S. X. Lim, S. H. Tang, C. H. Sow, and X. Zhang. Transient photoconductivity of ternary CdSSe nanobelts as measured by time-resolved terahertz spectroscopy. *The Journal of Physical Chemistry C*, 117(23):12379–12384, 2013.
- [107] J. S. Jie, W. J. Zhang, Y. Jiang, and S. T. Lee. Transport properties of single-crystal CdS nanoribbons. *Applied physics letters*, 89(22):223117, 2006.
- [108] C. Chen, M. Dutta, and M. A. Stroscio. Electron scattering via interactions with optical phonons in wurtzite crystals. *Physical Review B*, 70(7):075316, 2004.
- [109] K. Ellmer, Andreas K., and Bernd R. *Transparent conductive zinc oxide: basics and applications in thin film solar cells*. Berlin: Springer., 2008.

- [110] C. Klingshirn, R. Hauschild, Johannes F., and H. Kalt. Room-temperature stimulated emission of ZnO: Alternatives to excitonic lasing. *Physical Review B*, 75:115203, Mar 2007.
- [111] F. S. Hickernell. Zinc-oxide thin-film surface-wave transducers. *Proceedings of the IEEE*, 64(5):631–635, 1976.
- [112] A. R. Hutson. Piezoelectricity and conductivity in ZnO and CdS. *Physical Review Letters*, 4:505–507, 1960.
- [113] C. Klingshirn. ZnO: Material, physics and applications. *ChemPhysChem*, 8(6):782–803, 2007.
- [114] N. Holonyak, W. D. Laidig, B. A. Vojak, K. Hess, J. J. Coleman, P. D. Dapkus, and J. Bardeen. Alloy clustering in $\text{Al}_x\text{Ga}_{1-x}$ As-GaAs quantum-well heterostructures. *Physical Review Letters*, 45(6):1703–1706, 1980.
- [115] H. Kawai, K. Kaneko, and N. Watanabe. Photoluminescence of AlGaAs/GaAs quantum wells grown by metalorganic chemical vapor deposition. *Journal of Applied Physics*, 56(2):463–467, 1984.
- [116] C. Klingshirn, J. Fallert, H. Zhou, J. Sartor, C. Thiele, F. Maier-Flaig, D. Schneider, and H. Kalt. 65 years of zno research-old and very recent results. *physica status solidi (b)*, 247(6):1424–1447, 2010.
- [117] C. H. Park, S. B. Zhang, and Su-Huai Wei. Origin of p-type doping difficulty in ZnO: The impurity perspective. *Physical Review B*, 66:073202, 2002.
- [118] M. P. Paranthaman, W. Wong-Ng, and R. Bhattacharya. *Semiconductor materials for solar photovoltaic cells*. Cham: Springer., 2015.
- [119] A. Janotti and C. G. Van de Walle. Fundamentals of zinc oxide as a semiconductor. *Reports on Progress in Physics*, 72(12):126501, 2009.
- [120] Ü. Özgür, Ya. I. Alivov, C. Liu, A. Teke, M. A. Reshchikov, S. Doan, V. Avrutin, S.-J. Cho, and H. Morko. A comprehensive review of ZnO materials and devices. *Journal of Applied Physics*, 98(4):041301, 2005.
- [121] L. Yu, Q. Zhu, D. Fan, and Z. Lan. Development in p-type doping of ZnO. *Journal of Wuhan University of Technology-Mater. Sci. Ed.*, 27(6):1184–1187, 2012.
- [122] K. Tang, S.-L. Gu, J.-D. Ye, S.-M. Zhu, R. Zhang, and Y.-D. Zheng. Recent progress of the native defects and p-type doping of zinc oxide. *Chinese Physics B*, 26(4):047702, 2017.
- [123] D. C. Look and B. Claffin. P-type doping and devices based on ZnO. *physica status solidi (b)*, 241(3):624–630, 2004.

- [124] A. Mang, K. Reimann, and St. Rbenacke. Band gaps, crystal-field splitting, spin-orbit coupling, and exciton binding energies in ZnO under hydrostatic pressure. *Solid State Communications*, 94(4):251 – 254, 1995.
- [125] Q. H. Li, Q. Wan, Y. X. Liang, and T. H. Wang. Electronic transport through individual ZnO nanowires. *Applied Physics Letters*, 84(22):4556–4558, 2004.
- [126] R. Ghosh and D. Basak. Electrical and ultraviolet photoresponse properties of quasialigned ZnO nanowires/p-si heterojunction. *Applied Physics Letters*, 90(24):243106, 2007.
- [127] T. J. Hsueh, C. L. Hsu, S. J. Chang, Y. R. Lin, S. P. Chang, Y. Z. Chiou, T. S. Lin, and I. C. Chen. Crabwise ZnO nanowire UV photodetector prepared on zno : Ga/glass template. *IEEE Transactions on Nanotechnology*, 6(6):595–600, 2007.
- [128] A. B. Djurisic, X. Chen, Y. H. Leung, and A. Man Ching Ng. ZnO nanostructures: growth, properties and applications. *J. Mater. Chem.*, 22:6526–6535, 2012.
- [129] A. H. Kitai. Oxide phosphor and dielectric thin films for electroluminescent devices. *Thin Solid Films*, 445(2):367 – 376, 2003. Proceedings of the 3rd International Symposium on Transparent Oxide Thin films for Electronics and Optics.
- [130] S.J. Pearton, D.P. Norton, K. Ip, Y.W. Heo, and T. Steiner. Recent progress in processing and properties of ZnO. *Progress in Materials Science*, 50(3):293 – 340, 2005.
- [131] R. Kumar, O. Al-Dossary, G. Kumar, and A. Umar. Zinc oxide nanostructures for NO₂ gas–sensor applications: A review. *Nano-Micro Letters*, 7(2):97–120, 2015.
- [132] R. Pietruszka, B.S. Witkowski, S. Gieraltowska, P. Caban, L. Wachnicki, E. Zielony, K. Gwozdz, P. Bieganski, E. Placzek-Popko, and M. Godlewski. New efficient solar cell structures based on zinc oxide nanorods. *Solar Energy Materials and Solar Cells*, 143:99 – 104, 2015.
- [133] F. Fleischhaker, V.a Wloka, and I. Hennig. ZnO based field-effect transistors (fets): solution-processable at low temperatures on flexible substrates. *J. Mater. Chem.*, 20:6622–6625, 2010.
- [134] E. Guziewicz, M. Godlewski, T. Krajewski, . Wachnicki, A. Szczepanik, K. Kopalko, A. Wjcik-Godowska, E. Przedziecka, W. Paszkowicz, E. usakowska, P. Kruszewski, N. Huby, G. Tallarida, and S. Ferrari. ZnO grown by atomic layer deposition: A material for transparent electronics and organic heterojunctions. *J. Appl. Phys.*, 105:122413, 2009.

- [135] K. M. Lee, C. W. Lai, K. S. Ngai, and J. C. Juan. Recent developments of zinc oxide based photocatalyst in water treatment technology: A review. *Water Research*, 88:428 – 448, 2016.
- [136] L. J. Brillson and Y. Lu. ZnO schottky barriers and ohmic contacts. *Journal of Applied Physics*, 109(12):121301, 2011.
- [137] Z. L. Wang. ZnO nanowire and nanobelt platform for nanotechnology. *Materials Science and Engineering: R: Reports*, 64(34):33 – 71, 2009.
- [138] A. Ashrafi and C. Jagadish. Review of zincblende ZnO: Stability of metastable ZnO phases. *Journal of Applied Physics*, 102(7):071101, 2007.
- [139] A. B. M. A. Ashrafi, A. Ueta, A. Avramescu, H. Kumano, I. Suemune, Y.-W. Ok, and T.-Y. Seong. Growth and characterization of hypothetical zinc-blende ZnO films on GaAs(001) substrates with ZnS buffer layers. *Applied Physics Letters*, 76(5):550–552, 2000.
- [140] S. Desgreniers. High-density phases of ZnO: Structural and compressive parameters. *Physical Review B*, 58:14102–14105, 1998.
- [141] Z. L. Wang. Zinc oxide nanostructures: growth, properties and applications. *Journal of Physics: Condensed Matter*, 16(25):R829, 2004.
- [142] Y.W. Heo, B.S. Kang, L.C. Tien, D.P. Norton, F. Ren, J.R. La Roche, and S.J. Pearton. UV photoresponse of single ZnO nanowires. *Applied Physics A*, 80(3):497–499, 2005.
- [143] L.-C. Chao, S.-Y. Tsai, C.-N. Lin, C.-C. Liao, and C.-C. Ye. Vertically aligned ZnO nanowires prepared by thermal oxidation of rf magnetron sputtered metallic zinc films. *Materials Science in Semiconductor Processing*, 16(5):1316 – 1320, 2013. *Advanced Oxides for Electronics*.
- [144] W. Lee, M.-C. Jeong, and J.-M. Myoung. Catalyst-free growth of ZnO nanowires by metal-organic chemical vapour deposition (mocvd) and thermal evaporation. *Acta Materialia*, 52(13):3949 – 3957, 2004.
- [145] R. Q. Guo, J. Nishimura, M. Matsumoto, D. Nakamura, and T. Okada. Catalyst-free synthesis of vertically-aligned ZnO nanowires by nanoparticle-assisted pulsed laser deposition. *Applied Physics A*, 93(4):843, 2008.
- [146] W. Wang, G. Zhang, L. Yu, X. Bai, Z. Zhang, and X. Zhao. Field emission properties of zinc oxide nanowires fabricated by thermal evaporation. *Physica E: Low-dimensional Systems and Nanostructures*, 36(1):86 – 91, 2007.
- [147] G. Zhu, Y. Zhou, S. Wang, R. Yang, Y. Ding, X. Wang, Y. Bando, and Z. Lin Wang. Synthesis of vertically aligned ultra-long ZnO nanowires on heterogeneous substrates with catalyst at the root. *Nanotechnology*, 23(5):055604, 2012.

- [148] B. Q. Cao, K. Sakai, D. Nakamura, I. A. Palani, H. B. Gong, H. Y. Xu, M. Higashihata, and T. Okada. Stimulated optical emission from ZnO nanobelts grown with a simple carbothermal evaporation method. *The Journal of Physical Chemistry C*, 115(5):1702–1707, 2010.
- [149] Z. W. Pan, Z. R. Dai, and Z. L. Wang. Nanobelts of semiconducting oxides. *Science*, 291(5510):1947–1949, 2001.
- [150] Z. Li, J. Nieto-Pescador, A. J. Carson, J. C. Blake, and L. Gundlach. Efficient Z-scheme charge separation in novel vertically aligned ZnO/CdSSe nanotrees. *Nanotechnology*, 27(13):135401, 2016.
- [151] Z. Li, J. Nieto-Pescador, A. J. Carson, J. C. Blake, and L. Gundlach. Synthesis of hierarchical ZnO/CdSSe heterostructure nanotrees. *Journal of Visualized Experiments*, 2016.
- [152] F. Jamali-Sheini, R. Yousefi, and K.R. Patil. Surface characterization of AuZnO nanowire films. *Ceramics International*, 38(8):6665 – 6670, 2012.
- [153] Z. Zhang, S. J. Wang, T. Yu, and T. Wu. Controlling the growth mechanism of ZnO nanowires by selecting catalysts. *The Journal of Physical Chemistry C*, 111(47):843, 2007.
- [154] J.-J. Wu and S.-C. Liu. Catalyst-free growth and characterization of ZnO nanorods. *The Journal of Physical Chemistry B*, 106(37):9546–9551, 2002.
- [155] X Wang, J. Song, P. Li, J. H. Ryou, R. D. Dupuis, C. J. Summers, and Z. L. Wang. Growth of uniformly aligned ZnO nanowire heterojunction arrays on gan, aln, and al0.5ga0.5n substrates. *Journal of the American Chemical Society*, 127(21):7920–7923, 2005.
- [156] Zhong Lin Wang. ZnO nanowire and nanobelt platform for nanotechnology. *Materials Science and Engineering: R: Reports*, 64(3):33 – 71, 2009.
- [157] F.-. Chu, C.-W. Huang, C.-L. Hsin, C.-W. Wang, S.-Y. Yu, P.-H. Yeh, and W.-W. Wu. Well-aligned ZnO nanowires with excellent field emission and photocatalytic properties. *Nanoscale*, 4:1471–1475, 2012.
- [158] R. Yousefi and A.K. Zak. Growth and characterization of ZnO nanowires grown on the Si(111) and Si(100) substrates: Optical properties and biaxial stress of nanowires. *Materials Science in Semiconductor Processing*, 14(2):170 – 174, 2011.
- [159] A.B. Djurii, A.M.C. Ng, and X.Y. Chen. ZnO nanostructures for optoelectronics: Material properties and device applications. *Progress in Quantum Electronics*, 34(4):191 – 259, 2010.

- [160] M. Schwartzman, D. Tsivion, D. Mahalu, O. Raslin, and E. Joselevich. Self-integration of nanowires into circuits via guided growth. *Proceedings of the National Academy of Sciences*, 110(38):15195–15200, 2013.
- [161] D. Tsivion, M. Schwartzman, R. Popovitz-Biro, and E. Joselevich. Guided growth of horizontal ZnO nanowires with controlled orientations on flat and faceted sapphire surfaces. *ACS Nano*, 6(7):6433–6445, 2012.
- [162] B. Nikoobakht, C. A. Michaels, S. J. Stranick, and M. D. Vaudin. Horizontal growth and in situ assembly of oriented zinc oxide nanowires. *Applied Physics Letters*, 85(15):3244–3246, 2004.
- [163] I. Levin, A. Davydov, B. Nikoobakht, N. Sanford, and P. Mogilevsky. Growth habits and defects in ZnO nanowires grown on gan/sapphire substrates. *Applied Physics Letters*, 87(10):103110, 2005.
- [164] N. Ferralis, R. Maboudian, and C. Carraro. Structure and morphology of annealed gold films galvanically displaced on the Si (111) surface. *The Journal of Physical Chemistry C*, 11(20):7508–7513, 2007.
- [165] K. W. Schwarz and J. Tersoff. Elementary processes in nanowire growth. *Nano Letters*, 11(2):316–320, 2011.
- [166] W. Zhang and K. Yanagisawa. Hydrothermal synthesis of ZnO long fibers. *Chemistry Letters*, 34(8):1170–1171, 2005.
- [167] F. Libo, S. Hongwei, Y. Lixin, L. Zhongxin, Y. Linmei, P. Guohui, B. Xue, L. Yanqiang, W. Tie, Z. Zhuhong, and K. Xianggui. Hydrothermal synthesis and photoluminescent properties of ZnO sub-micrometer and micrometer rods. *Optical Materials*, 29(5):532 – 538, 2007.
- [168] H. Hu, X. Huang, C. Deng, X. Chen, and Y. Qian. Hydrothermal synthesis of ZnO nanowires and nanobelts on a large scale. *Materials Chemistry and Physics*, 106(1):58 – 62, 2007.
- [169] E. Ohshima, H. Ogino, I. Niikura, K. Maeda, M. Sato, M. Ito, and T. Fukuda. Growth of the 2-in-size bulk ZnO single crystals by the hydrothermal method. *Journal of Crystal Growth*, 260(1):166 – 170, 2004.
- [170] H. Zhang, D. Yang, X. Ma, Y. Ji, J. Xu, and D. Que. Synthesis of flower-like ZnO nanostructures by an organic-free hydrothermal process. *Nanotechnology*, 15(5):622, 2004.
- [171] W.-J. Li, E.-W. Shi, W.-Z. Zhong, and Z.-W. Yin. Growth mechanism and growth habit of oxide crystals. *Journal of Crystal Growth*, 203(1):186 – 196, 1999.

- [172] Z. Hou, L. Guo, H. Wang, Y. Shen, G. Wang, Y. Li, and Q. Jiang. Synthesis of dumbbell-like ZnO microcrystals via a simple solution route. *Nanoscale Research Letters*, 7(1):507, 2012.
- [173] Y. Liu, H. Lv, S. Li, G. Xi, and X. Xing. Synthesis and characterization of ZnO with hexagonal dumbbell-like bipods microstructures. *Advanced Powder Technology*, 22(6):784 – 788, 2011.
- [174] X. Gao, X. Li, and W. Yu. Flowerlike ZnO nanostructures via hexamethylenetetramine-assisted thermolysis of zincethylenediamine complex. *The Journal of Physical Chemistry B*, 109(3):1155–1161, 2005.
- [175] B. G. Wang, E. W. Shi, and W. Z. Zhong. Twinning morphologies and mechanisms of ZnO crystallites under hydrothermal conditions. *Crystal Research and Technology*, 33(6):937–941, 1998.
- [176] W. Neumann. Crystallography of boundaries and interfaces. *Acta Physica Polonica-Series A General Physics*, 89(2):195–208, 1996.
- [177] M. Bitenc, G. Dražić, and Z. C. Orel. Characterization of crystalline zinc oxide in the form of hexagonal bipods. *Crystal Growth & Design*, 10(2):830–837, 2010.
- [178] B. Mayers and Y. Xia. Formation of tellurium nanotubes through concentration depletion at the surfaces of seeds. *Advanced Materials*, 14(4):279–282, 2002.
- [179] Z. Liu, S. Li, Y. Yang, Z. Hu, S. Peng, J. Liang, and Y. Qian. Shape-controlled synthesis and growth mechanism of one-dimensional nanostructures of trigonal tellurium. *New Journal of Chemistry*, 27:1748–1752, 2003.
- [180] Z. Wang, L.g Wang, J. Huang, H. Wang, L. Pan, and X. Wei. Formation of single-crystal tellurium nanowires and nanotubes via hydrothermal recrystallization and their gas sensing properties at room temperature. *Journal of Material Chemistry*, 20:2457–2463, 2010.
- [181] V. Strano, R. G. Urso, M. Scuderi, K. O. Iwu, F. Simone, E. Ciliberto, C. Spinella, and S. Mirabella. Double role of HMTA in ZnO nanorods grown by chemical bath deposition. *The Journal of Physical Chemistry C*, 118(48):28189–28195, 2014.
- [182] L. E. Greene, M. Law, D. H. Tan, M. Montano, J. Goldberger, G. Somorjai, and P. Yang. General route to vertical ZnO nanowire arrays using textured zno seeds. *NANO letters*, 5(7):1231–1236, 2005.
- [183] J. Cui. Defect control and its influence on the exciton emission of electrodeposited ZnO nanorods. *The Journal of Physical Chemistry C*, 112(28):10385–10388, 2008.
- [184] L.-Y. Chen, Y.-T. Yin, C.-H. Chen, and J.-W. Chiou. Influence of polyethyleneimine and ammonium on the growth of ZnO nanowires by hydrothermal method. *The Journal of Physical Chemistry C*, 115(43):20913–20919, 2011.

- [185] Y. Zhou, W. Wu, H. Hu, G. and Wu, and S. Cui. Hydrothermal synthesis of ZnO nanorod arrays with the addition of polyethyleneimine. *Materials Research Bulletin*, 43(8):2113–2118, 2008.
- [186] C. Klingshirn. Review article: ZnO: From basics towards applications. *physica status solidi (b)*, 244(9):3019–3019, 2007.
- [187] *Zinc oxide: from fundamental properties towards novel applications*, volume 120. Springer Science & Business Media.
- [188] D.G. Thomas. Interstitial zinc in zinc oxide. *Journal of Physics and Chemistry of Solids*, 3(3):229 – 237, 1957.
- [189] K. Hoffmann and D. Hahn. Electron spin resonance of lattice defects in zinc oxide. *physica status solidi (a)*, 24(2):637–648, 1974.
- [190] J. Čížek, J. Valenta, P. Hruška, O. Melikhova, I. Procházka, M. Novotný, and J. Bulíř. Origin of green luminescence in hydrothermally grown ZnO single crystals. *Applied Physics Letters*, 106:251902, 2015.
- [191] Y. Yang, X. W. Sun, B. K. Tay, Peter H. T. Cao, J. X. Wang, and X. H. Zhang. Revealing the surface origin of green band emission from ZnO nanostructures by plasma immersion ion implantation induced quenching. *Journal of Applied Physics*, 103:064307, 2008.
- [192] F. Fabbri, M. Villani, A. Catellani, A. Calzolari, G. Cicero, D. Calestani, G. Calestani, A. Zappettini, B. Dierre, T. Sekiguchi, and G. Salviati. Zn vacancy induced green luminescence on non-polar surfaces in ZnO nanostructures. *scientific reports*, 4:5158, 2014.
- [193] *Introduction to solid state physics*. Hoboken, NJ: Wiley.
- [194] J.C. Fan, K.M. Sreekanth, Z. Xie, S.L. Chang, and K.V. Rao. p-type ZnO materials: Theory, growth, properties and devices. *Progress in Materials Science*, 58(6):874 – 985, 2013.
- [195] R. Vidya, P. Ravindran, H. Fjellvåg, B. G. Svensson, E. Monakhov, M. Ganchenkova, and R. M. Nieminen. Energetics of intrinsic defects and their complexes in zno investigated by density functional calculations. *Physical Review B*, 83:045206, 2011.
- [196] A. A. Sokol, S. A. French, S. T. Bromley, C. R. A. Catlow, H. J. J. van Dam, and P. Sherwood. Point defects in ZnO. *Faraday Discuss.*, 134:267–282, 2007.
- [197] Fumiyasu Oba, Atsushi Togo, Isao Tanaka, Joachim Paier, and Georg Kresse. Defect energetics in ZnO: A hybrid hartree-fock density functional study. *Physical Review B*, 77:245202, 2008.

- [198] Y.-S. Kim and C. H. Park. Rich variety of defects in ZnO via an attractive interaction between o vacancies and Zn interstitials: Origin of n -type doping. *Physical Review Letters*, 102:086403, 2009.
- [199] P.S. Xu, Y.M. Sun, C.S. Shi, F.Q. Xu, and H.B. Pan. The electronic structure and spectral properties of ZnO and its defects. *Nuclear Instruments and Methods in Physics Research Section B: Beam Interactions with Materials and Atoms*, 199:286 – 290, 2003.
- [200] J. C. Blake, J. Nieto-Pescador, Z. Li, and L. Gundlach. Ultraviolet femtosecond Kerr-gated wide-field fluorescence microscopy. *Optics Letters*, 41(11):2462–2465, Jun 2016.
- [201] M. A. Duguay and J. W. Hansen. An ultrafast light gate. *Applied Physics Letters*, 15(6):192–194, May 1969.
- [202] D. Hulin, J. Etchepare, A. Antonetti, L. L. Chase, G. Grillon, A. Migus, and A. Mysyrowicz. Subpicosecond timeresolved luminescence spectroscopy of highly excited CuCl. *Applied Physics Letters*, 45(9):993–995, 1984.
- [203] Z. Yu, L. Gundlach, and P. Piotrowiak. Efficiency and temporal response of crystalline Kerr media in collinear optical kerr gating. *Optics Letters*, 36(15):2904–2906, Aug 2011.
- [204] I. Dmitruk, Y. Shynkarenko, A. Dmytruk, D. Aleksyuk, V. Kadan, P. Korenyuk, N. Zubrilin, and I. Blonskiy. Efficiency estimates and practical aspects of an optical kerr gate for time-resolved luminescence spectroscopy. *Methods and Applications in Fluorescence*, 4(4):044007, 2016.
- [205] K. Appavoo and M. Y. Sfeir. Enhanced broadband ultrafast detection of ultraviolet emission using optical Kerr gating. *Review of Scientific Instruments*, 85(5):055114, 2014.
- [206] R. Paschotta. *Encyclopedia of Laser Physics and Technology*. Wiley-VCH, 2008.
- [207] *Ultrafast dynamics of single ZnO nanowires using ultraviolet femtosecond Kerr-gated wide-field fluorescence microscopy*, volume 9956, 2016.
- [208] J. Fallert, F. Stelzl, H. Zhou, A. Reiser, K. Thonke, R. Sauer, C. Klingshirn, and H. Kalt. Lasing dynamics in single ZnO nanorods. *Optics Express*, 16:1125–1131, 2008.
- [209] J. Dai, C. Xu, T. Nakamura, Y. Wang, J. Li, and Y. Lin. Electron–hole plasma induced band gap renormalization in ZnO microlaser cavities. *Optics Express*, 22:28831–28837, 2014.

- [210] J. C. Johnson, H. Yan, P. Yang, and R. J. Saykally. Optical cavity effects in ZnO nanowire lasers and waveguides. *Nano Letters*, 107:8816–8828, 2003.
- [211] J. C. Johnson, K. P. Knutsen, H. Yan, M. Law, Y. Zhang, P. Yang, and R. J. Saykally. Ultrafast carrier dynamics in single ZnO nanowire and nanoribbon lasers. *Nano Letters*, 4:197–204, 2004.
- [212] M. R. Junnarkar and R. R. Alfano. Photogenerated high-density electron-hole plasma energy relaxation and experimental evidence for rapid expansion of the electron-hole plasma in CdSe. *Physical Review B*, 34:7045–7062, 1986.
- [213] H. Yoshikawa and S. Adachi. Optical constants of ZnO. *Japanese Journal of Applied Physics*, 36(10R):6237, 1986.
- [214] S. Xu, C. Xu, Y. Liu, Y. Hu, R. Yang, Q. Yang, J.-H. Ryou, H. J. Kim, Z. Lochner, S. Choi, R. Dupuis, and Z. L. Wang. Ordered nanowire array blue/near-UV light emitting diodes. *Advanced Materials*, 22(42):4749–4753, 2010.
- [215] J. K. Song, U. Willer, J. M. Szarko, S. R. Leone, S. Li, and Y. Zhao. Ultrafast upconversion probing of lasing dynamics in single ZnO nanowire lasers. *The Journal of Physical Chemistry C*, 112(5):1679–1684, 2008.
- [216] D. Vanmaekelbergh and L. K. van Vugt. ZnO nanowire lasers. *Nanoscale*, 3:2783–2800, 2011.
- [217] N. Arai, J. Takeda, H.-J.Ko, and T. Yao. Dynamics of high-density excitons and electronhole plasma in ZnO epitaxial thin films. *Journal of Luminescence*, 119:346 – 349, 2006. Dynamical Processes in Excited States of Solids.
- [218] S Mitsubori, I Katayama, S H Lee, T Yao, and J Takeda. Ultrafast lasing due to electronhole plasma in ZnO nano-multipods. *Journal of Physics: Condensed Matter*, 21(6):064211, 2009.
- [219] J. Takeda, H. Jinnouchi, S. Kurita, Y.F. Chen, and T. Yao. Dynamics of photoexcited high density carriers in ZnO epitaxial thin films. *physica status solidi (b)*, 229(2):877–880, 2002.
- [220] R. Röder, T. P. H. Sidiropoulos, C. Tessarek, S. Christiansen, R. F. Oulton, and C. Ronning. Ultrafast dynamics of lasing semiconductor nanowires. *Nano Letters*, 15(2):4637–4643, 2015.
- [221] Sokrates T. Pantelides. *Deep centers in semiconductors: a state of the art approach*. Gordon and Breach, 1992.
- [222] E. G. Seebauer and K. W. Noh. Trends in semiconductor defect engineering at the nanoscale. *Materials Science and Engineering: R: Reports*, 70(3-6):151 – 168, 2010.

- [223] Z. E. Horváth, A. A. Koós, K. Kertész, G. Molnár, G. Vértesy, M. C. Bein, T. Frigyes, Z. Mészáros, J. Gyulai, and L. P. Biró. The role of defects in chemical sensing properties of carbon nanotube films. *Applied Physics A*, 93(2):495–504, 2008.
- [224] C. A. Aggelopoulos, M. Dimitropoulos, A. Govatsi, L. Sygellou, C. D. Tsakiroglou, and S.N. Yannopoulos. Influence of the surface-to-bulk defects ratio of ZnO and TiO₂ on their UV-mediated photocatalytic activity. *Applied Catalysis B: Environmental*, 205:292 – 301, 2017.
- [225] Y.-Y. Lou, S. Yuan, Y. Zhao, Z.-Y. Wang, and L.-Y. Shi. Influence of defect density on the ZnO nanostructures of dye-sensitized solar cells. *Advances in Manufacturing*, 1(4):340–345, 2013.
- [226] J. L. Benton. Characterization of defects in semiconductors by deep level transient spectroscopy. *Journal of Crystal Growth*, 106(1):116 – 126, 1990.
- [227] W. C. Chueh and S. M. Haile. Electrochemical studies of capacitance in cerium oxide thin films and its relationship to anionic and electronic defect densities. *Physical Chemistry Chemical Physics*, 11:8144–8148, 2009.
- [228] M.M. Lucchese, F. Stavale, E.H. Martins Ferreira, C. Vilani, M.V.O. Moutinho, Rodrigo B. Capaz, C.A. Achete, and A. Jorio. Quantifying ion-induced defects and Raman relaxation length in graphene. *Carbon*, 48:1592 – 1597, 2010.
- [229] J. Hong, Zhixin Hu, M. Probert, K. Li, D. Lv, X. Yang, L. Gu, N. Mao, Q. Feng, L. Xie, J. Zhang, D. Wu, Z. Zhang, C. Jin, W. Ji, X. Zhang, J. Yuan, and Z. Zhang. Exploring atomic defects in molybdenum disulphide monolayers. *Nature Communications*, 6:6293, 2010.
- [230] A. Felten, X. Gillon, M. Gulas, J.-J. Pireaux, X. Ke, G. Van Tendeloo, C. Bittencourt, E. Najafi, and A. P. Hitchcock. Measuring point defect density in individual carbon nanotubes using polarization-dependent X-ray microscopy. *ACS Nano*, 4:4431–4436, 2010.
- [231] H. Xue, N. Pan, R. Zeng, M. Li, X. Sun, Z. Ding, X. Wang, and J. G. Hou. Probing the surface effect on deep-level emissions of an individual ZnO nanowire via spatially resolved cathodoluminescence. *The Journal of Physical Chemistry C*, 113:12715–12718, 2009.
- [232] C. X. Xu, X. W. Sun, C. Yuen, B. J. Chen, S. F. Yu, and Z. L. Dong. Ultra-violet amplified spontaneous emission from self-organized network of zinc oxide nanofibers. *Applied Physics Letters*, 86:011118, 2005.
- [233] A. E. Siegman. *Lasers*. University Science Books, 1986.

- [234] J. K. Song, U. Willer, J. M. Szarko, S. R. Leone, S. Li, and Y. Zhao. Ultrafast upconversion probing of lasing dynamics in single ZnO nanowire lasers. *The Journal of Physical Chemistry C*, 112:1679–1684, 2008.
- [235] G.P. Zhu, C.X. Xu, J. Zhu, X. Li, K. Zheng, J.P. Liu, C.G. Lu, and Y.P. Cui. Characteristics of ultraviolet amplified spontaneous emission from zinc oxide nanowires. *Optical Materials*, 31(2):181 – 183, 2008.
- [236] S. Xu, C. Xu, Y. Liu, Y. Hu, R. Yang, Q. Yang, J.-H. Ryou, H. J. Kim, Z. Lochner, S. Choi, R. Dupuis, and Zhong L. Wang. Ordered nanowire array blue/near-UV light emitting diodes. *Advanced Materials*, 22(42):4749–4753, 2010.
- [237] G. P. Agrawal and N. k. Dutta. *Semiconductor Lasers*. Van Nostrand Reinhold, 1993.
- [238] Yongchun Zhong, Aleksandra B. Djurii, Yuk Fan Hsu, Kam Sing Wong, Gerhard Brauer, Chi Chung Ling, and Wai Kin Chan. Exceptionally long exciton photoluminescence lifetime in ZnO tetrapods. *The Journal of Physical Chemistry C*, 112(42):16286–16295, 2008.
- [239] E. Kioupakis, Q. Yan, D. Steiauf, and C. G. Van de Walle. Temperature and carrier-density dependence of Auger and radiative recombination in nitride optoelectronic devices. *New Journal of Physics*, 15(12):125006, 2013.
- [240] A. M. Stoneham. Non-radiative transitions in semiconductors. *Reports on Progress in Physics*, 44(12):1251, 1981.
- [241] R. S. Wagner and W. C. Ellis. Vaporliquid-solid mechanism of single crystal growth. *Applied Physics Letters*, 4(5):89–90, 1964.
- [242] C. C. Weigand, M. R. Bergren, C. Ladam, J. Tveit, R. Holmestad, P. E. Vullum, J. C. Walmsley, . Dahl, T. E. Furtak, R. T. Collins, J. Grepstad, and H. Weman. Formation of ZnO nanosheets grown by catalyst-assisted pulsed laser deposition. *Crystal Growth & Design*, 11(12):5298–5304, 2011.
- [243] Hugh F. Wilson, Chunguang Tang, and Amanda S. Barnard. Morphology of zinc oxide nanoparticles and nanowires: Role of surface and edge energies. *The Journal of Physical Chemistry C*, 120(17):9498–9505, 2016.
- [244] X. Wang, K. Chen, Y. Zhang, J. Wan, O. L. Warren, J. Oh, J. Li, E. Ma, and Z. Shan. Growth conditions control the elastic and electrical properties of ZnO nanowires. *Nano Letters*, 15(12):7886–7892, 2015.
- [245] M. D. Schroer and J. R. Petta. Correlating the nanostructure and electronic properties of InAs nanowires. *Nano Letters*, 10(5):1618–1622, 2010.

- [246] A. S. Ameruddin, H. A. Fonseka, P. Caroff, J. Wong-Leung, R. LM Op het Veld, J. L. Boland, M. B. Johnston, H. H. Tan, and C. Jagadish. $\text{In}_x\text{Ga}_{1-x}\text{As}$ nanowires with uniform composition, pure wurtzite crystal phase and taper-free morphology. *Nanotechnology*, 26(20):205604, 2015.
- [247] M. Villafuerte, J. M. Ferreyra, C. Zapata, J. Barzola-Quiquia, F. Iikawa, P. Esquinazi, S. P. Heluani, M. M. de Lima Jr., and A. Cantarero. Defect spectroscopy of single ZnO microwires. *Journal of Applied Physics*, 115(13):133101, 2014.
- [248] K. Bandopadhyay and J. Mitra. Zn interstitials and O vacancies responsible for n-type zno: what do the emission spectra reveal. *RSC Advances*, 5:23540–23547, 2015.
- [249] A. Janotti and C. G. Van de Walle. New insights into the role of native point defects in ZnO. *Journal of Crystal Growth*, 287(1):58 – 65, 2006.
- [250] K. Suzuki, M. Inoguchi, K. Fujita, S. Murai, K. Tanaka, N. Tanaka, A. Ando, and H. Takagi. High-density excitation effect on photoluminescence in ZnO nanoparticles. *Journal of Applied Physics*, 107(12):124311, 2010.
- [251] A. Othonos, M. Zervos, and D. Tsokkou. Tin oxide nanowires: The influence of trap states on ultrafast carrier relaxation. *Nanoscale Research Letters*, 4(8):828–833, 2009.
- [252] A. W. Cohn, A. M. Schimpf, C. E. Gunthardt, and D. R. Gamelin. Size-dependent trap-assisted auger recombination in semiconductor nanocrystals. *Nano Letters*, 13(4):1810–1815, 2013.
- [253] V. N. Abakumov, V. I. Perel, and I. N. Yassievich. *Nonradiative recombination in semiconductors*. Amsterdam: North-Holland, 1991.
- [254] B. K. Meyer. *New Data and Updates for IV-IV, III-V, II-VI and I-VII Compounds, their Mixed Crystals and Diluted Magnetic Semiconductors*. Springer-Verlag Berlin Heidelberg, 2011.
- [255] Guang Zhu, Yusheng Zhou, Sihong Wang, Rusen Yang, Yong Ding, Xue Wang, Yoshio Bando, and Zhong lin Wang. Synthesis of vertically aligned ultra-long ZnO nanowires on heterogeneous substrates with catalyst at the root. *Nanotechnology*, 23(5):055604, 2012.
- [256] X. Xu, F. S. F. Brossard, D. A. Williams, D. P. Collins, M. J. Holmes, R. A. Taylor, and X. Zhang. Cavity modes of tapered ZnO nanowires. *New Journal of Physics*, 12(8):083052, 2010.
- [257] B. P. Mehl, R. L. House, A. Uppal, A. J. Reams, C. Zhang, J. R. Kirschbrown, and J. M. Papanikolas. Direct imaging of optical cavity modes in ZnO rods using

second harmonic generation microscopy. *The Journal of Physical Chemistry A*, 114(3):1241–1246, 2010.

- [258] J. R. Kirschbrown, R. L. House, B. P. Mehl, J. K. Parker, and J. M. Papanikolas. Hybrid standing wave and whispering gallery modes in needle-shaped ZnO rods: Simulation of emission microscopy images using finite difference frequency domain methods with a focused gaussian source. *The Journal of Physical Chemistry C*, 117(8):10653–10660, 2013.

Appendix A
FIGURE REPRINT PERMISSIONS



RightsLink®

Home

Account Info

Help



ACS Publications
Most Trusted. Most Cited. Most Read.

Title: Ultrafast Spatially Resolved Carrier Dynamics in Single CdSSe Nanobelts
Author: Lars Gundlach, Piotr Piotrowiak
Publication: The Journal of Physical Chemistry C
Publisher: American Chemical Society
Date: Jul 1, 2009

Logged in as:

Jolie Blake

LOGOUT

Copyright © 2009, American Chemical Society

PERMISSION/LICENSE IS GRANTED FOR YOUR ORDER AT NO CHARGE

This type of permission/license, instead of the standard Terms & Conditions, is sent to you because no fee is being charged for your order. Please note the following:

- Permission is granted for your request in both print and electronic formats, and translations.
- If figures and/or tables were requested, they may be adapted or used in part.
- Please print this page for your records and send a copy of it to your publisher/graduate school.
- Appropriate credit for the requested material should be given as follows: "Reprinted (adapted) with permission from (COMPLETE REFERENCE CITATION). Copyright (YEAR) American Chemical Society." Insert appropriate information in place of the capitalized words.
- One-time permission is granted only for the use specified in your request. No additional uses are granted (such as derivative works or other editions). For any other uses, please submit a new request.

If credit is given to another source for the material you requested, permission must be obtained from that source.

BACK

CLOSE WINDOW

Copyright © 2017 [Copyright Clearance Center, Inc.](#) All Rights Reserved. [Privacy statement](#). [Terms and Conditions](#).

Comments? We would like to hear from you. E-mail us at customer@copyright.com

Figure A.1: Reprint permission for Figure 2.1, 3.3 and 3.6.

[Printable details.](#)

License Number	4133661422530
License date	Jun 21, 2017
Licensed Content Publisher	Elsevier
Licensed Content Publication	Chemical Physics
Licensed Content Title	Spatial variation in carrier dynamics along a single CdSSe nanowire
Licensed Content Author	Jolie C. Blake, Peter S. Eldridge, Lars Gundlach
Licensed Content Date	Oct 17, 2014
Licensed Content Volume	442
Licensed Content Issue	n/a
Licensed Content Pages	4
Type of Use	reuse in a thesis/dissertation
Portion	figures/tables/illustrations
Number of figures/tables /illustrations	4
Format	both print and electronic
Are you the author of this Elsevier article?	Yes
Will you be translating?	No
Order reference number	
Original figure numbers	
Title of your thesis/dissertation	Characterization of Nanostructured Semiconductors by Ultrafast Luminescence Dynamics
Expected completion date	Aug 2017
Estimated size (number of pages)	120
Elsevier VAT number	GB 494 6272 12
Requestor Location	Jolie Blake 607 Lehigh rd NEWARK, DE 19711 United States Attn: Jolie Blake
Publisher Tax ID	98-0397604
Total	0.00 USD

ORDER MORE

CLOSE WINDOW

Figure A.2: Reprint permission for Figure 3.2.



RightsLink®

Home

Create Account

Help



ACS Publications
Most Trusted. Most Cited. Most Read.

Title: Color-Tunable
Photoluminescence of Alloyed
CdSxSe1-x Nanobelts

Author: Anlian Pan, Hua Yang, Ruibin
Liu, et al

Publication: Journal of the American
Chemical Society

Publisher: American Chemical Society

Date: Nov 1, 2005

Copyright © 2005, American Chemical Society

LOGIN

If you're a [copyright.com](#) user, you can login to RightsLink using your [copyright.com](#) credentials. Already a RightsLink user or want to [learn more?](#)

PERMISSION/LICENSE IS GRANTED FOR YOUR ORDER AT NO CHARGE

This type of permission/license, instead of the standard Terms & Conditions, is sent to you because no fee is being charged for your order. Please note the following:

- Permission is granted for your request in both print and electronic formats, and translations.
- If figures and/or tables were requested, they may be adapted or used in part.
- Please print this page for your records and send a copy of it to your publisher/graduate school.
- Appropriate credit for the requested material should be given as follows: "Reprinted (adapted) with permission from (COMPLETE REFERENCE CITATION). Copyright (YEAR) American Chemical Society." Insert appropriate information in place of the capitalized words.
- One-time permission is granted only for the use specified in your request. No additional uses are granted (such as derivative works or other editions). For any other uses, please submit a new request.

If credit is given to another source for the material you requested, permission must be obtained from that source.

BACK

CLOSE WINDOW

Copyright © 2017 [Copyright Clearance Center, Inc.](#) All Rights Reserved. [Privacy statement](#). [Terms and Conditions](#).

Comments? We would like to hear from you. E-mail us at customercare@copyright.com

Figure A.3: Reprint permission for Figure 3.7.

pubscopyright

to me ▾

May 15 (1 day ago) ☆ ↶ ▾

Dear Jolie C. Blake,

Thank you for contacting The Optical Society.

As long as the copyrighted material is included within the body, section or chapter, of the thesis, and is not posted separate from the thesis, OSA considers your requested use of its copyrighted materials to be permissible within the author rights granted in the Copyright Transfer Agreement submitted by the requester on acceptance for publication of his/her manuscript. It is requested that a complete citation of the original material be included in any publication. This permission assumes that the material was not reproduced from another source when published in the original publication.

Let me know if you have any questions.

Kind Regards,

Rebecca Robinson

Rebecca Robinson

May 15, 2017

Authorized Agent, The Optical Society

From: Jolie Blake [mailto:jblake@udel.edu]

Sent: Monday, May 15, 2017 3:37 PM

To: pubscopyright

Subject: Copyright permission request

xxx

Figure A.4: Reprint permission for Figure 5.1.

This Agreement between Jolie Blake ("You") and Elsevier ("Elsevier") consists of your license details and the terms and conditions provided by Elsevier and Copyright Clearance Center.

License Number	4114361401451
License date	May 22, 2017
Licensed Content Publisher	Elsevier
Licensed Content Publication	Progress in Materials Science
Licensed Content Title	Recent progress in processing and properties of ZnO
Licensed Content Author	S.J. Pearton,D.P. Norton,K. Ip,Y.W. Heo,T. Steiner
Licensed Content Date	Mar 1, 2005
Licensed Content Volume	50
Licensed Content Issue	3
Licensed Content Pages	48
Start Page	293
End Page	340
Type of Use	reuse in a thesis/dissertation
Portion	figures/tables/illustrations
Number of figures/tables /illustrations	1
Format	both print and electronic
Are you the author of this Elsevier article?	No
Will you be translating?	No
Order reference number	
Original figure numbers	Table 1
Title of your thesis/dissertation	Characterization of Nanostructured Semiconductors by Ultrafast Luminescence Dynamics
Expected completion date	Aug 2017
Estimated size (number of pages)	120
Elsevier VAT number	GB 494 6272 12
Requestor Location	Jolie Blake 607 Lehigh rd NEWARK, DE 19711 United States Attn: Jolie Blake
Publisher Tax ID	98-0397604
Total	0.00 USD
Terms and Conditions	

Figure A.5: Reprint permission for Table 4.1.

This Agreement between Jolie Blake ("You") and Elsevier ("Elsevier") consists of your license details and the terms and conditions provided by Elsevier and Copyright Clearance Center.

License Number	4114370606234
License date	May 22, 2017
Licensed Content Publisher	Elsevier
Licensed Content Publication	Materials Science and Engineering: R: Reports
Licensed Content Title	ZnO nanowire and nanobelt platform for nanotechnology
Licensed Content Author	Zhong Lin Wang
Licensed Content Date	Apr 3, 2009
Licensed Content Volume	64
Licensed Content Issue	3-4
Licensed Content Pages	39
Start Page	33
End Page	71
Type of Use	reuse in a thesis/dissertation
Intended publisher of new work	other
Portion	figures/tables/illustrations
Number of figures/tables /illustrations	2
Format	both print and electronic
Are you the author of this Elsevier article?	No
Will you be translating?	No
Order reference number	
Original figure numbers	Figure 2, Figure 3.
Title of your thesis/dissertation	Characterization of Nanostructured Semiconductors by Ultrafast Luminescence Dynamics
Expected completion date	Aug 2017
Estimated size (number of pages)	120
Elsevier VAT number	GB 494 6272 12
Requestor Location	Jolie Blake 607 Lehigh rd NEWARK, DE 19711 United States Attn: Jolie Blake
Publisher Tax ID	98-0397604

Figure A.6: Reprint permission for Figure 4.1 and Figure 4.2.

Nicole Harris <nicoleh@spie.org>

5:00 PM (8 minutes ago)

to me

Dear Ms. Blake,

Thank you for seeking permission from SPIE to reprint material from our publications. As author, SPIE shares the copyright with you, so you retain the right to reproduce your paper in part or in whole.

Publisher's permission is hereby granted under the following conditions:

- (1) the material to be used has appeared in our publication without credit or acknowledgment to another source; and
- (2) you credit the original SPIE publication. Include the authors' names, title of paper, volume title, SPIE volume number, and year of publication in your credit statement.

Sincerely,

Nicole Harris
Administrative Editor, SPIE Publications
1000 20th St.
Bellingham, WA 98225
[+1 360 685 5586](tel:+13606855586) (office)
nicoleh@spie.org

SPIE is the international society for optics and photonics. <http://SPIE.org>

SPIE.

From: Jolie Blake [mailto:jblake@udel.edu]
Sent: Tuesday, May 23, 2017 11:53 AM
To: reprint_permission <reprint_permission@spie.org>
Subject: Reprint permission request

Figure A.7: Reprint permission for Figure 5.2, Figure 5.3, Figure 5.4 and 6.3.

[Printable details.](#)

License Number	4120450488359
License date	Jun 01, 2017
Licensed Content Publisher	Elsevier
Licensed Content Publication	Journal of Crystal Growth
Licensed Content Title	Growth mechanism and growth habit of oxide crystals
Licensed Content Author	Wen-Jun Li,Er-Wei Shi,Wei-Zhuo Zhong,Zhi-Wen Yin
Licensed Content Date	May 1, 1999
Licensed Content Volume	203
Licensed Content Issue	1-2
Licensed Content Pages	11
Type of Use	reuse in a thesis/dissertation
Portion	figures/tables/illustrations
Number of figures/tables/illustrations	3
Format	both print and electronic
Are you the author of this Elsevier article?	No
Will you be translating?	No
Order reference number	
Original figure numbers	Figure 1 9 and 10
Title of your thesis/dissertation	Characterization of Nanostructured Semiconductors by Ultrafast Luminescence Dynamics
Expected completion date	Aug 2017
Estimated size (number of pages)	120
Elsevier VAT number	GB 494 6272 12
Requestor Location	Jolie Blake 607 Lehigh rd NEWARK, DE 19711 United States Attn: Jolie Blake
Publisher Tax ID	98-0397604
Total	0.00 USD

[ORDER MORE](#)

[CLOSE WINDOW](#)

Figure A.8: Reprint permission for Figure 4.8.

[Printable details.](#)

License Number	4124410324089
License date	Jun 08, 2017
Licensed Content Publisher	John Wiley and Sons
Licensed Content Publication	Crystal Research & Technology
Licensed Content Title	Twinning Morphologies and Mechanisms of ZnO Crystallites under Hydrothermal Conditions
Licensed Content Author	B. G. Wang,E. W. Shi,W. Z. Zhong
Licensed Content Date	Dec 14, 1998
Licensed Content Pages	5
Type of use	Dissertation/Thesis
Requestor type	University/Academic
Format	Print and electronic
Portion	Figure/table
Number of figures/tables	1
Original Wiley figure/table number(s)	Figure 5
Will you be translating?	No
Title of your thesis / dissertation	Characterization of Nanostructured Semiconductors by Ultrafast Luminescence Dynamics
Expected completion date	Aug 2017
Expected size (number of pages)	120
Requestor Location	Jolie Blake 607 Lehigh rd NEWARK, DE 19711 United States Attn: Jolie Blake
Publisher Tax ID	EUS26007151
Billing Type	Invoice
Billing address	Jolie Blake 607 Lehigh rd NEWARK, DE 19711 United States Attn: Jolie Blake
Total	0.00 USD

Figure A.9: Reprint permission for Figure 4.13.

[Printable details.](#)

License Number	4130361072483
License date	Jun 15, 2017
Licensed Content Publisher	American Physical Society
Licensed Content Publication	Physical Review B
Licensed Content Title	Native point defects in ZnO
Licensed Content Author	Anderson Janotti and Chris G. Van de Walle
Licensed Content Date	Oct 4, 2007
Licensed Content Volume	76
Type of use	Thesis/Dissertation
Requestor type	Student
Format	Print, Electronic
Portion	image/photo
Number of images/photos requested	1
Portion description	Figure 3
Rights for	Main product
Duration of use	Life of Current Edition
Creation of copies for the disabled	no
With minor editing privileges	no
For distribution to	United States
In the following language(s)	Original language of publication
With incidental promotional use	no
Lifetime unit quantity of new product	0 to 499
The requesting person/organization	Jolie Blake
Order reference number	
Title of your thesis / dissertation	Characterization of Nanostructured Semiconductors by Ultrafast Luminescence Dynamics
Expected completion date	Aug 2017
Expected size (number of pages)	120
Requestor Location	Jolie Blake 607 Lehigh rd NEWARK, DE 19711 United States Attn: Jolie Blake
Billing Type	Invoice
Billing address	Jolie Blake 607 Lehigh rd NEWARK, DE 19711 United States Attn: Jolie Blake
Total	0.00 USD

Figure A.10: Reprint permission for Figure 4.17.

[Printable details.](#)

License Number	4130380690700
License date	Jun 15, 2017
Licensed Content Publisher	American Physical Society
Licensed Content Publication	Physical Review B
Licensed Content Title	Energetics of intrinsic defects and their complexes in ZnO investigated by density functional calculations
Licensed Content Author	R. Vidy a et al.
Licensed Content Date	Jan 31, 2011
Licensed Content Volume	83
Type of use	Thesis/Dissertation
Requestor type	Student
Format	Print, Electronic
Portion	image/photo
Number of images/photos requested	1
Portion description	figure 2
Rights for	Main product
Duration of use	Life of Current Edition
Creation of copies for the disabled	no
With minor editing privileges	no
For distribution to	Worldwide
In the following language(s)	Original language of publication
With incidental promotional use	no
Lifetime unit quantity of new product	0 to 499
The requesting person/organization	Jolie Blake
Order reference number	
Title of your thesis / dissertation	Characterization of Nanostructured Semiconductors by Ultrafast Luminescence Dynamics
Expected completion date	Aug 2017
Expected size (number of pages)	120
Requestor Location	Jolie Blake 607 Lehigh rd NEWARK, DE 19711 United States Attn: Jolie Blake
Billing Type	Invoice
Billing address	Jolie Blake 607 Lehigh rd NEWARK, DE 19711 United States Attn: Jolie Blake
Total	0.00 USD

Figure A.11: Reprint permission for Figure 4.16.